

ASSESSING THE POTENTIAL FOR MAGMATIC SULFIDES WITHIN
SOUTHWESTERN LAURENTIA LARGE IGNEOUS PROVINCE

By

Thomas J. Boes

Bachelor of Science in Geology
University of Nevada, Las Vegas
2021

A thesis submitted in partial fulfillment
of the requirements for the

Master of Science - Geoscience

Department of Geoscience
College of Sciences
The Graduate College

University of Nevada, Las Vegas
May 2024



Thesis Approval

The Graduate College
The University of Nevada, Las Vegas

April 2, 2024

This thesis prepared by

Thomas J. Boes

entitled

Assessing the Potential for Magmatic Sulfides within Southwestern Laurentia Large Igneous Province

is approved in partial fulfillment of the requirements for the degree of

Master of Science - Geoscience
Department of Geoscience

Simon Jowitt, Ph.D.
Examination Committee Chair

Andrew Martin, Ph.D.
Examination Committee Member

Kevin Konrad, Ph.D.
Examination Committee Member

Carlos Dimas, Ph.D.
Graduate College Faculty Representative

Alyssa Crittenden, Ph.D.
*Vice Provost for Graduate Education &
Dean of the Graduate College*

ABSTRACT

The ~1.1 Ga magmatism of the Southwestern Laurentia Large Igneous Province (SWLLIP) generated a series of mafic-ultramafic sheets, sills, and dikes emplaced within Mesoproterozoic sedimentary units and older crystalline basement rock throughout the southwest United States and northern Mexico. This large igneous province (LIP) event remains enigmatic in identifying the processes that generated this magmatism. In addition, potential links to the contemporaneous magmatism of North America's magmatic Ni-Cu-platinum group element (PGE) mineralized Mid-Continent Rift (MCR) LIP to the northeast of the SWLLIP remain unclear. The contemporaneous 1.1 Ga MCR LIP event hosts economically viable magmatic sulfide deposits in the Duluth Complex in Minnesota and elsewhere, providing further incentive to understand the links between the LIP events as well as independently assessing the mineral exploration potential for magmatic sulfide deposit formation within the SWLLIP. This study aims to further our knowledge of the petrogenesis of the SWLLIP and the potential of this magmatic event to host magmatic sulfide mineralization.

Whole-rock geochemical and Pt, Pd, and Au data have been obtained for 52 SWLLIP samples from California, Arizona, and New Mexico, allowing an initial assessment of the petrogenesis, magmatic sulfide fertility, sulfide saturation status, and crustal contamination of magmas of the SWLLIP to be assessed. All these factors are critical in determining the potential for this LIP to host magmatic Ni-Cu-PGE sulfide mineralization. Two suites have been identified within the SWLLIP

that define two distinct magmatic pulses during the LIP event: a potentially prospective (from a magmatic sulfide viewpoint) tholeiitic suite and a seemingly unprospective alkaline suite. The tholeiitic suite has undepleted chalcophile element samples, demonstrating that the magmas that formed the suite were derived from a fertile mantle source region with sufficient partial melting to generate chalcophile-undepleted magmas. Furthermore, some tholeiitic samples within this suite are depleted in chalcophile elements and are crustally contaminated, suggesting that the magmas assimilated country rocks and became sulfur-saturated before emplacement. This process is crucial in most magmatic Ni-Cu-PGE mineralizing systems elsewhere and within the SWLLIP-generated immiscible sulfide melts deposited elsewhere within the system. This indicates the magmatic sulfide prospectivity of intrusions with this tholeiitic suite within the SWLLIP. In comparison, alkaline SWLLIP suite samples are uniformly depleted in chalcophile elements and display varying degrees of crustal contamination that do not contain sufficient sulfides, inferring they are unfertile. These unfertile melts were generated by low degree partial melting of the mantle and did not become sulfur saturated before emplacement. Overall, this research indicates that exploration for magmatic sulfides within the SWLLIP should focus on intrusions and sections of the LIP with affinities to the tholeiitic suite. The transitional alkaline suite is likely unprospective of chalcophile elements from an exploration viewpoint. This geochemical dataset allows for comparison between the two distinct pulses of magmatism in the SWLLIP and the MCR magmatism, particularly the

mafic magmatism associated with the Duluth Complex, which is suggestive of a single plume under the North American craton.

ACKNOWLEDGMENTS

This research would not have been possible without Dr. Simon Jowitt's exceptional knowledge and guidance throughout my graduate school journey. His door was always open, allowing me to expand my understanding of economic geology and delve deeper into the science and how it connects with our daily lives. I am grateful to my committee members, Dr. Andrew Martin and Dr. Kevin Konrad, for their unwavering support and insightful advice on the intricate details with significant implications. Dr. Carlos Dimas deserves acknowledgment for igniting my passion for education and introducing me to UNLV's Special Collections. Special thanks to Tim Cliffe for continuously inspiring me to make Geoscience accessible to students and shaping my educational path.

Thank you for funding from Richard Ernst, the Rocky Mountain Federation of Mineralogical Societies scholarship, the Society of Economic Geologists student grant, and travel funding from the UNLV Graduate and Professional Student Association.

My heartfelt appreciation goes to my family and friends who accompanied me on this journey. Sierra Ramsey, your open door allowed for spontaneous discussions, and those delightful baked treats were invaluable. I owe a debt of gratitude to Dr. Dalton McCaffrey, my mentor turned friend, who patiently listened and provided invaluable insights into my research.

I am thankful for my mother, Arline Toler; your unwavering support and assistance with the children made my academic pursuits manageable. My brother,

Andrew Toler, and his wife, Shasta Lewis, provided remote support and encouragement, inspiring me to persevere. To my children, Laila, Talia, and Quentin, your presence made every challenging day worthwhile. You are my greatest joy. And to my beloved wife, Nyeisha Boes, your unwavering support and understanding anchored me throughout this journey. Your love and stability provided the foundation for our family to thrive. I am forever grateful.

TABLE OF CONTENTS

ABSTRACT	iii
ACKNOWLEDGMENTS	vi
LIST OF FIGURES	x
I. INTRODUCTION	1
II. GEOLOGICAL SETTING AND BACKGROUND	9
Death Valley.....	14
Colorado River region, California and Arizona.....	14
Hualapai Mountain	15
Garnet Mountain	16
Salt River Canyon.....	16
Southwest of Burro Mountain.....	17
III. SAMPLING AND ANALYTICAL METHODS	18
IV. PETROGRAPHY	20
V. GEOCHEMISTRY	22
VI. DISCUSSION	48
Genesis of the SWLLIP magmas	48
Crustal contamination of the SWLLIP magmas.....	53
Magmatic sulfur saturation history of SWLLIP magmatism	56

Evidence for the tectonic setting of the SWLLIP	62
Spatial variation within the SWLLIP	67
VII. CONCLUSIONS AND FUTURE WORK	70
APPENDICES	74
Appendix A: Figure 3 and others	74
Appendix B : Figure 8 and others	76
Appendix C: Sample locations and geochemistry	78
Appendix D: Standard geochemistry and certificate values.	96
REFERENCES	102
CURRICULUM VITAE.....	114

LIST OF FIGURES

Figure 1. Base maps for SWLLIP..	13
Figure 2. Hand samples from SWLLIP.	21
Figure 3. Photomicrographs showing representative examples of SWLLIP units.....	74
Figure 4. Nb/Y vs. Zr/Ti basalt classification diagram.	24
Figure 5. Nb/Y vs. Zr/P ₂ O ₅ tholeiitic and alkaline discrimination diagram..	26
Figure 6. Ti vs. V diagram.....	28
Figure 7. Diagram (Tb/Yb) PM and (La/Sm) PM	31
Figure 8. Plots of MgO (wt.%) vs. major element oxides (wt.%) for SWLLIP samples.....	76
Figure 9. Multi-element variation diagrams normalized to primitive mantle values.....	34
Figure 10. Diagrams showing the chalcophile element variations within the SWLLIP showing Ni (A) Cu (B), Pd (C), and Pd (D) variations compared to MgO concentrations	37
Figure 11. Diagrams showing variation in (Cu/Zr)PM (A) and (Pd/Yb)PM (B) ratios with MgO concentrations..	39
Figure 12. Diagram (Nb/Th)PM and (Th/Yb)PM	41
Figure 13. Diagram (Cu/Zr)PM (A) and (Pd/Yb)PM (B)	44
Figure 14. Diagram (Nb/Yb)PM and (Th/Yb)PM..	45
Figure 15. Diagram showing variation in Cu/Pd ratios compared to Pd concentration.....	47
Figure 16. Magmatic sulfide model for SWLLIP	72

I. INTRODUCTION

Large Igneous Provinces (LIPs) were first defined by Coffin and Eldholm (1994) as large-volume but short-duration igneous events that can have global effects, including on climate associated with mass extinctions (Ganino and Arndt, 2009; Ernst and Youbi, 2017), topographic uplift, rifting, and other plate tectonic effects. Importantly, these provinces host world-class mineral deposits (Ernst and Jowitt, 2013; Ernst, 2021; Srivastava et al., 2022). These magmatic provinces are generally defined as large volumes of magma ($>100,000 \text{ km}^3$) that were emplaced or erupted over a large area ($>100,000 \text{ km}^2$) but over a relatively short period ($<1\text{-}5$ Myrs) or as a series of pulses (often <1 Myr) typically with an overall duration of ~ 50 Myrs (Bryan and Ernst, 2008; Ernst R., 2021). Large Igneous Provinces are not restricted to any geologic period or geographic location (Bryan and Ernst, 2008) but occur throughout the geological record and have been identified globally. Lastly, LIPs are useful for paleocontinent reconstruction because LIPs can link rifted continents (Ernst et al., 2013) and are valuable analogs for abundant intraplate magmatism on planet bodies (Hansen, 2007; Ernst, 2021).

In general, LIPs can contain both felsic and mafic components (Sheth, 2007). However, mafic-ultramafic LIPs are more common throughout geological history and are directly associated with a wide range of mineralizing systems, especially the magmatic Ni-Cu-platinum group element (PGE) sulfide mineralization that forms the focus of this study (e.g., Ernst and Jowitt, 2013). The complex nature of

LIP plumbing systems (e.g., Srivastava et al., 2022) means that the signatures of mineralization can be recorded in various ways within a given LIP system or event, even in samples that may at first appear to be unrelated to mineralization (i.e., do not contain any sulfide mineralization). For example, chalcophile element depletions within the crustally contaminated portions of the volcanic pile of the Siberian Trap LIP provide a distal record of the formation of the associated Noril'sk-Talnakh magmatic sulfide deposit (Keays and Lightfoot, 2010; Yao and Mungall, 2022). Magmatic Ni-Cu-PGE mineralization associated with LIPs includes the world-class Noril'sk-Talnakh deposit within the Siberian Trap flood basalts (Naldrett, 2004), the Duluth Complex associated with the Keweenaw or Mid-Continent Rift LIP (Severson et al., 2002), mineralization within the Musgrave Province related to the Giles Event in Australia (Maier et al., 2015), and numerous others. Magmatic sulfide mineralization in LIPs is also not constrained to one specific LIP or plumbing system (Munteanu et al., 2010; Barnes et al., 2015; Ernst et al., 2019). Thus, understanding the processes involved in LIP petrogenesis and evolution is important in understanding the mineral exploration and magmatic sulfide prospectivity within each part of a given LIP.

The other reason for investigating the magmatic sulfide potential of LIP events is that demand for Ni, Cu, Co, and the PGE is expected to increase over the next few decades as a result of the energy transition, especially in the electric vehicle (EV) and "green-energy" sectors (Northey et al., 2014; Mudd et al., 2018; Hughes et al., 2021). The production of PGE worldwide has been dominated by

Russia and South Africa, with this geographical concentration leading to supply chain insecurity and price volatility (e.g., mine closures due to COVID-19)(Mudd et al., 2018; Jowitt et al., 2020). The discovery of additional magmatic sulfide deposits can help alleviate supply chain risks for PGE, Ni, and Cu through the geographic and geopolitical diversification of resource supply.

Magmatic sulfide deposits can be divided into S-rich deposits that are enriched in Ni-Cu (and often Co) with minor amounts of PGE and S-poor deposits (<5% sulfide) that are enriched in the PGE relative to Ni and Cu (Naldrett, 1999; Barnes et al., 2017). This study focuses on the potential for S-rich deposits within the 1.1 Ga SWLLIP. The magmatic sulfide mineralization within these systems accounts for a small percentage of the overall volume of a given LIP (typically <0.1%, often far less). For example, the magmatism associated with the Siberian Traps occurred over an area of $\sim 7 \times 10^6$ km² (Ivanov et al., 2013). In contrast, the main mineralized portion of this LIP, the Noril'sk-Talnakh deposits, represent one of the largest globally known volumes of magmatic sulfide mineralization but crops out over an area of only ~ 50 km² (Yakubchuk and Nikishin, 2004), only $\sim 0.000007\%$ of the total area of the LIP. Identifying the various geochemical signatures of individual suites within an LIP is crucial in defining the total and regional prospectivity of a given LIP, the timing of the mineralization within a LIP system, and geochemical identifiers that enable the determination of the prospectivity of a given unit within a LIP, especially as some suites within a LIP will be prospective for magmatic sulfides and others will not (e.g., Jowitt et al., 2014). A combination of

chalcophile and lithophile elemental geochemistry is therefore key for determining the processes involved in LIP formation, including partial melting of the mantle, sulfur saturation, and crustal contamination, all of which directly influence magmatic sulfide prospectivity and genesis (Naldrett, 2010a; Ernst and Jowitt, 2013; Jowitt and Ernst, 2013; Barnes et al., 2017).

Magmatic sulfide Ni-Cu-PGE deposits are thought to form from S-undersaturated mafic to ultramafic mantle-derived melts that are eventually emplaced in the crust, with S-saturation occurring typically as a result of crustal contamination or the fractional crystallization of a silicate melt although the latter often results in subeconomic sulfide generation (grade and volume); crustal contamination is thought to be required to form economic magmatic sulfide mineralization (Naldrett, 1999, 2010b, 2010a; Barnes and Lightfoot, 2005; Keays and Lightfoot, 2010; Barnes et al., 2017; Yao et al., 2018; Yao and Mungall, 2021). The chalcophile elements within these systems are sourced from the mantle, and their abundances (and whether a given magma is chalcophile element enriched or depleted) are generally controlled by the degree of mantle melting with higher degree (>20%) partial melting generating melts that sequester more of the chalcophile elements within the mantle source region than low degree (<10%) partial melts (Barnes and Lightfoot, 2005; Barnes et al., 2015; Smythe et al., 2017) although other influences such as the oxidation state of the mantle may also play a role (Mungall et al., 2006). High-degree partial melting of the mantle thus enables the formation of chalcophile undepleted melts that are fertile from a magmatic

sulfide prospectivity perspective (Naldrett, 2010a; Barnes et al., 2017). These melts transport most of the chalcophile elements from the mantle source region to the crust, where timely sulfur saturation can generate immiscible sulfide melts that form magmatic sulfide mineralization. Sulfur saturation within the silicate melt typically needs to occur before significant fractionation because of cooling and crystallization, which would remove Ni and other chalcophile elements like Pt from the system by the crystallization of olivine and pyroxene and, therefore, would limit the amount of Ni and other chalcophile elements that would be available for any immiscible sulfide melts within the system (Naldrett, 2010a). Magmatic systems also tend to decrease in energy with increasing differentiation and fractionation, inhibiting critical aspects like the interaction between silicate and sulfide melts, as discussed below. The degree and timing of S-saturation thus determines the magnitude of immiscible sulfide chalcophile element enrichment achievable within a system and whether a given magmatic system (or part or suite within a magmatic system) is prospective for magmatic sulfide mineralization.

If a magma becomes S-saturated, the resulting immiscible sulfide droplets within the system interact with silicate melts, scavenging chalcophile elements from the latter. The ratio at which this interaction occurs is known as the R-factor (Campbell and Naldrett, 1979), with higher R-factors leading to higher tenor sulfide melts, where the tenor is the abundance of chalcophile elements within the sulfide portion of a magmatic system (Holwell and McDonald, 2010). Increasing turbulence within a system can lead to the enrichment of the immiscible sulfide melts in

chalcophile elements as well as the amalgamation of these sulfides into larger droplet sizes (Robertson et al., 2015; Yao and Mungall, 2022). These denser sulfides then begin to accumulate, enabling the settling out of the sulfide melt in structural traps within the magmatic plumbing system (Barnes and Lightfoot, 2005; Holwell and McDonald, 2010; Robertson et al., 2015; Yao and Mungall, 2022). Magma conduits and pathways are also vital in controlling magmatic sulfide accumulation since they provide structural traps for the sulfide melt and pathways into potentially S-rich sediments. Although magmatic plumbing systems are complex and the extent of their subsurface features may be unknown, geochemical data can assist in determining the individual components of the LIP as well as insight into the composition, origin, and dynamics of the magma (Cundari et al., 2021; Rollinson and Pease, 2021; Black et al., 2021; Klausen, 2022). The role of magma conduits is thus not limited to facilitating magmatic sulfide deposition but also upgrading the sulfide melt by allowing for continual magmatic recharge events involving chalcophile element-undepleted (e.g., high-degree partial melts) melts that enable the upgrading of sulfides in the system, demonstrated by a high R-factor (Maier et al., 2001, 2015; Keays and Lightfoot, 2007, 2010; Munteanu et al., 2010).

As outlined above, immiscible magmatic sulfides concentrate chalcophile elements (i.e., Cu, Ni, Pd, Pt) that preferentially partition into sulfide melt rather than silicate melts (Smythe et al., 2017). The analysis of these chalcophile elements and their relationship to other magmatic processes and evolution (e.g., mineralogy and geochemical variations) can determine the magmatic sulfide behavior in the

LIP and, more importantly, identify portions of the LIP that are enriched and depleted in chalcophile elements. One example of this is determining whether primitive melts within a LIP system are PGE depleted or undepleted compared to mantle values (e.g., the primitive mantle; McDonough and Sun, 1995), with the latter indicative of a high degree of partial melting of the mantle and the formation of fertile melts that have a higher potential for magmatic sulfide genesis (Ripley and Li, 2003; Naldrett, 2010a). Equally important is examining the chalcophile element enrichment and depletion in different parts of LIP systems, especially in those exposed portions of a LIP system that are readily accessible at the surface (e.g., Jowitt et al., 2014). Identifying chalcophile element enrichment within individual units of a LIP indicates magmatic sulfide mineralization within that portion of the magmatic system. Chalcophile element depletions can be indicative of either infertile melts that formed during low-degree partial melting or may be indicative of fertile, immiscible silicate melts that have undergone sulfide saturation, with sulfide melt portions being deposited elsewhere in the system after segregating from the silicate melt portion. This immiscible sulfide generation process can be identified by the presence of a mix of cogenetic chalcophile element depleted and undepleted units within the same LIP or subset (i.e., magmatic suite) of a LIP, with the undepleted units representing the compositions of mantle-derived melts and the depleted units representing the melts after S-saturation and the generation and removal of sulfide melts and chalcophile elements from the magma; somewhat analogous to the exhaust system of an internal combustion engine providing

evidence of the combustion process (Keays and Lightfoot, 2010; Yuan et al., 2012; Jowitt et al., 2014; Yao and Mungall, 2021).

All the above indicates that geochemical data for the magmas and resulting rocks within a LIP are key in constraining the petrogenesis of LIP magmas as well as the presence or absence of a range of processes that control the magmatic sulfide prospectivity of a given magmatic event (Barnes, 2023). Suitable approaches include using whole-rock geochemical analysis to identify the geochemical characteristics of the melt source region (e.g., source enrichment; Jowitt and Ernst, 2013; Jowitt et al., 2014; Wallace et al., 2015) and the degree of melting associated with subsequent mineralization (low or high degree partial melting). Other important information for magmatic sulfide system petrogenesis that can be gleaned from lithochemical analysis include the potential geologic setting of LIP emplacement, the degrees of crustal contamination, and magma fractionation extent, all of which play a vital role in allowing S-saturation to occur within the melt (Holwell and McDonald, 2010; Naldrett, 2010a; Barnes, 2023).

This study is the first evaluation of the magmatic sulfide potential of the Southwest Laurentia Large Igneous Province (SWLLIP), a 1.1 Ga mafic-ultramafic LIP within the southwestern U.S. and Mexico. The geological setting and background of this LIP event are discussed below.

II. GEOLOGICAL SETTING AND BACKGROUND

The SWLLIP was emplaced into Mesoproterozoic shallow marine to terrestrial sedimentary environments and crystalline basement rock in southwest Laurentia (Wright et al., 1976; Hammond, 1986, 1990; Howard, 1991; Wrucke et al., 2007; Bright et al., 2014). Some sedimentary units were unconsolidated wet sediments during the diabase emplacement (Hammond, 1986).

The predominantly intrusive magmatism that formed the SWLLIP is recorded within the southwestern U.S. and Mexico between eastern California and western New Mexico (Wright et al., 1976; Hammond, 1990; Howard, 1991; Bright et al., 2014; Mohr et al., 2024)(Fig. 1). The mafic Mesoproterozoic magmatism can also possibly extend to subsurface environments in western Texas (Mosher, 1998; Bright et al., 2014; Adams et al., 2022) and contemporaneous felsic magmatism has been identified in northern Mexico and western Texas (Bright et al., 2014). The formation of the SWLLIP was initially constrained to 1094-1080 Ma by Bright et al. (2014), who dated the mafic portions of the LIP using zircon and baddeleyite U-Pb geochronology. Further dating by Mohr et al. (2024) focused on cogenetic felsic segregations within mafic units that revealed two distinct magmatic pulses, the first at 1098 Ma and a later pulse at 1083 Ma. The initial pulse was constrained by ages 1098.27 ± 0.27 Ma and 1097.91 ± 0.29 Ma while the later pulse was constrained by 1082.60 ± 0.30 Ma and 1082.18 ± 1.25 Ma (Mohr et al. 2024.)

The majority of exposed SWLLIP intrusions are hosted within a 1.4 Ga granitic batholith, but intrusions in younger sedimentary and older gneisses are

common and are exposed in tilted crustal blocks as a result of Basin and Range faulting throughout the southwestern U.S. (Hammond, 1986; Howard, 1991; Bright et al., 2014). Figure 1A shows the evolution of southwestern Laurentia and the magmatism that intrudes the accreted terranes within this region. The 1.4 Ga granite intrusions are believed to have been emplaced close to lithostatic pressure, perpendicular to foliations and shear zones of older 1.8 Ga rocks of the Mojave and ~1.8-1.6 Ga rocks of the Yavapai and Mazatzal provinces (Nyman and Karlstrom, 1997; Amato et al., 2008, 2011; Bright et al., 2014)(Fig. 1A). The Mojave and Yavapai provinces represent exotic terranes accreted at or before 1.74 Ga based upon metamorphic and isotopic data as well as the presence of detrital zircons in metasedimentary units of the Mojave province that have ages to the units within the Wyoming province (Duebendorfer et al., 2001; Strickland et al., 2013)(Fig. 1A). The Mazatzal province is also thought to be considered an exotic terrane accreted to the craton(e.g., Condie, 1982; Whitmeyer and Karlstrom, 2007), but Holland et al., (2020) suggest that this province formed in an extensional setting generated by slab rollback that generated magmatism at levels stratigraphically higher than the Yavapai Province basement rather than terrane accretion (Fig. 1A). The slab rollback model is supported by detrital zircons found within metasedimentary rocks of the Mazatzal province derived from the older Mojave and Yavapai provinces inferring a local rather than an exotic source (Holland et al., 2020). These provinces represent the growth of the lithosphere of the southwestern part of Laurentia and correlate with sedimentary units hosting SWLLIP diabase in similar deposit

environments across the region (Hammond, 1990; Wrucke, 1993; Bright et al., 2014; Grambling et al., 2022)(Fig. 1A).

The SWLLIP magmatism at ~1.1 Ga is contemporaneous with a limited extensional event within the southwestern U.S. (Hammond, 1990; Howard, 1991; Wrucke, 1993; Bright et al., 2014; Grambling et al., 2022). Diabase dikes and sills thus may have been emplaced passively parallel to the bedding or fabrics of the host rock with this emplacement enabled by the contemporaneous extension (Wrucke, 1993). Howard (1991) initially suggested a plume origin for the SWLLIP that was possibly related to the contemporaneous magmatism of the MCR, which is thought to be plume-related and associated with a period of continental rifting (Swanson-Hysell et al., 2019). However, Hammond (1990) interpreted the diabase units within the SWLLIP to have formed because of limited inter-plate rifting rather than within a continental margin setting, with a model involving the partial melting of a light rare earth element (LREE) enriched homogenous mantle source rather than any association with a mantle plume. Mafic magmatism associated with rifting is quite common, and the resulting magmas ascend and are transported through the crust via vertical and lateral migration along dikes and sills (Srivastava et al., 2022). However, exposed vertical intrusions (i.e., dikes) within the SWLLIP are relatively rare, with the main mode of emplacement seemingly horizontally in the upper crust (e.g., sheets and sills). Howard (1991) defined the diabase sheets with discordant features, placed originally horizontally before being rotated during later extension. The magmatism of the SWLLIP had likely been emplaced at a rate that was less

than the crustal extension rate due to sheet formations rather than vertical dikes within the SWLLIP (Howard, 1991).

The tertiary extension of the southwest U.S. caused the tilting of fault blocks that exposed the diabase intrusions sampled during this study, originally placed at paleodepths between 2 and 13 km (Howard, 1991). These sample localities were chosen (1) to adequately reflect variability in the differing country rock hosting the diabase intrusion and (2) to provide a representative sample population distributed across the SWLLIP area (Fig. 1B). The following sections provide brief sample location descriptions that are the focus of this study.

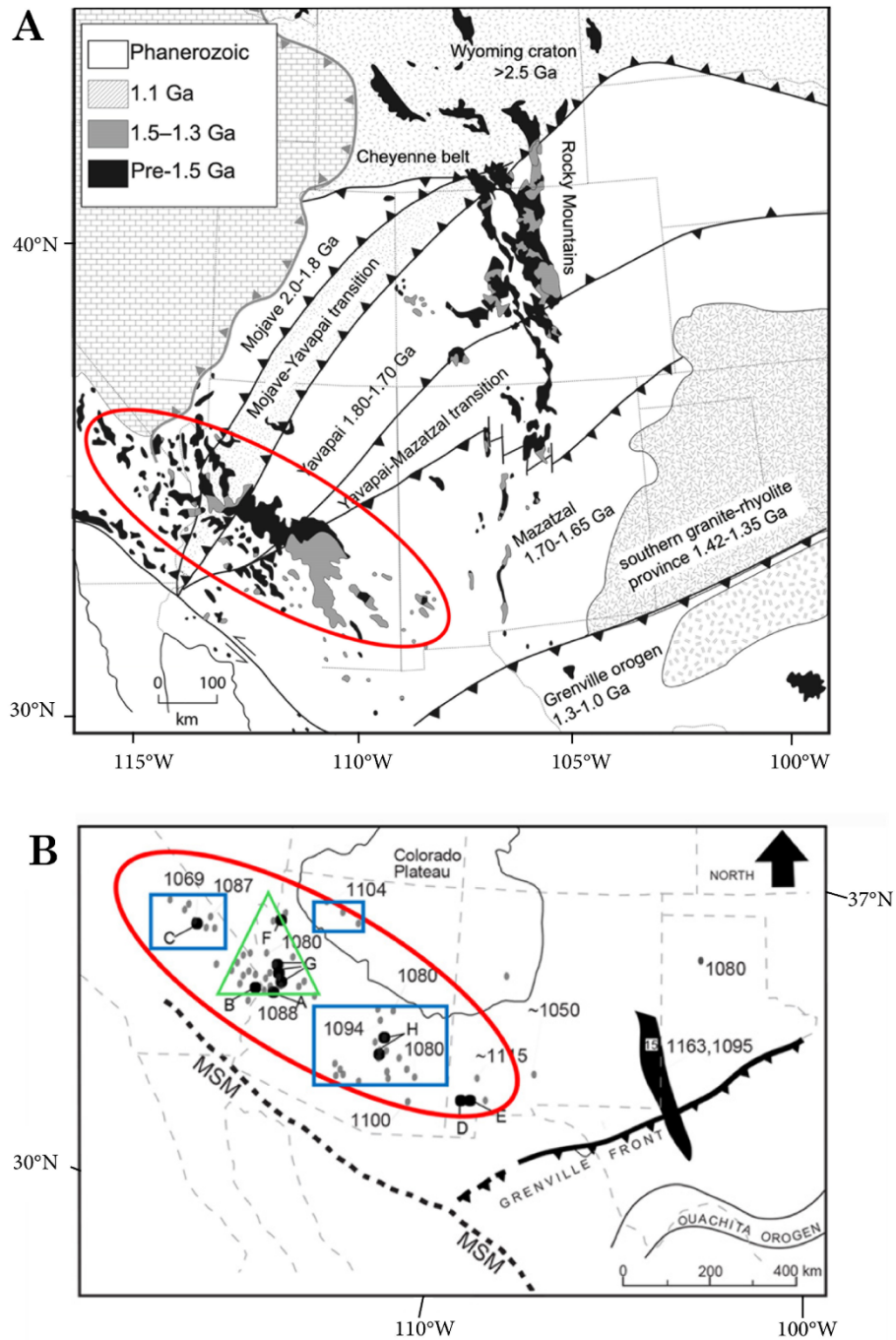


Figure 1. Base maps for SWLLIP. (A) Precambrian provinces of Southwest Laurentia and exposed Proterozoic rocks. Adapted from Amato et al. (2018) and modified from Karlstrom et al. (2004). The red oval on A and B is the general area of the SWLLIP locations. (B) Southwest USA with known diabase location (Gray ovals) and ages modified from Bright et al. (2014), Timmons et al. (2005), and Howard (1991). Blue squares denote the general area for 1093 Ma magmatism, and the green triangle specifies 1083 Ma magmatism for the SWLLIP (Mohr et al. 2024). Black circles are sampled locations from this study, including (A & B) Colorado River Basin; (C) Death Valley; (D & E) Burro Mountains; (F) Garnet Mountains; (G) Hualapai Mountains; and (H) Salt River Canyon.

California

Death Valley

SWLLIP sills within the Death Valley area were emplaced into the Stromatolite Member of the Middle Proterozoic Crystal Spring Formation, which consists of a basal arkosic conglomerate overlain by alternating sandstone, shale, and carbonate units that overlie 1.7 Ga crystalline basement rocks. (Roberts, 1976; Wright et al., 1976; Hammond, 1990). The Crystal Spring Formation makes up the lower portion of the Pahrump Group, with the latter strata suggestive of representing a failed rift (Wright et al., 1976). Hammond (1986) suggested upper members of the Crystal Spring Formation were still wet and unconsolidated when the diabase sills intruded. The Crystal Spring Formation records evidence of contemporaneous late Proterozoic deformation events initiated by diabase intrusions, which are demonstrated within low-angle faults in Galena Canyon. It is also associated with faults and thickening of units in which it was placed (Wrucke, 1967). The paleoenvironment during emplacement consisted of fan delta and carbonate tidal-flat sedimentary settings (Roberts, 1976). Sampling was taken from various heights within diabase sills that alternate with the Stromatolite Member of the Crystal Spring Formation.

Colorado River region, California and Arizona

The SWLLIP in the Colorado River region of both Arizona and California is present as diabase sheets (Howard, 1991). The eastern Arizona SWLLIP portion

consists of diabase sheets emplaced into granite gneiss units of the Bucks Mountain block of the Mojave Mountains (Howard et al., 1990; Howard, 1991). On the west side of the Colorado River in California, diabase sheets intrude red granodiorite to monzogranite of a metamorphic core complex within the Chemehuevi Mountains (John, 1982). Diabase contacts are sharp against the host rocks where exposed, and the diabase sheets' width ranges from a few meters to ~20 m, with some trending >100 m. Diabase sheets also dominate the SWLLIP within the Mojave Mountains of California and Arizona and are not always parallel to the fabric of the host rock (Howard, 1991). The exposure of the SWLLIP in this area was associated with mid-Tertiary Basin and Range faulting that tilted and uplifted a roughly 15 km thick crustal block, exposing the diabase plumbing system of the LIP (Howard, 1991). Samples were taken from various sills throughout the region, with samples TB002 and TB010 taken from a single ~6m thick sill but from ~300m apart.

Arizona

Hualapai Mountain

Diabase dikes and sills of the SWLLIP outcrop within the Hualapai Mountains to the southeast of the Buck Mountains in AZ but were originally emplaced at paleodepths of 2-13 km (Howard, 1991). The Hualapai Mountains are dominated by Paleoproterozoic metasedimentary units that were later intruded by a granite pluton (Ferguson et al., 2004). The metamorphic rocks within the mountains consist

of amphibolite, schist, and gneiss units (Stensrud and More, 1980). Samples were taken from a single 6 m thick sill and two equigranular dikes (Bright, 2012).

Garnet Mountain

The Garnet Mountains are located ~100 km to the NNE of the Hualapai Mountains in Arizona and consist of early Proterozoic porphyritic monzogranite and medium-grained leucocratic monzogranites that were emplaced as a plutonic complex into various Paleoproterozoic gneiss units (Blacet, 1975; Theodore et al., 1987; Bright, 2012). Diabase units of the SWLLIP were emplaced as dikes and sill throughout these Paleoproterozoic units (Blacet, 1975). One aphanitic sample was acquired from a single dike with poorly defined contacts (Bright, 2012).

Salt River Canyon

The Salt River Canyon is roughly 140 km to the east of Phoenix, AZ, and is located within the Yavapai Province. This area is dominated by Precambrian granites that are overlaid by the sedimentary units of the Apache Group and the Troy Quartzite, with diabase units of the SWLLIP emplaced into the granites as sills (Wrucke, 1989; Bright et al., 2014). Samples were collected from two different sills exposed in road cuts (Bright, 2012).

New Mexico

Southwest of Burro Mountain

The Burro Mountains are in southwest New Mexico and are dominated by Paleoproterozoic deformed granites and metasedimentary rocks that were intruded by ~1.45 Ga plutonic rocks and diabase units of the SWLLIP (Amato et al., 2008), with the latter poorly exposed but present throughout the leucogranite country rock. Five samples were taken from a ~5 m sill exposed in a roadcut and contained xenoliths of the granitic country rock. An additional two samples were taken ~13 km further east from two small outcrops and represent the eastern boundary of the study area.

III. SAMPLING AND ANALYTICAL METHODS

Samples were collected from the locations labeled in Figure 1B with additional thin sections and eight hand samples provided by Jeffrey Amato that were previously dated (Bright, 2012; Bright et al., 2014). A total of 44 diabase samples were collected during this study, with care taken to collect the least weathered samples from outcrops, with all 52 hand samples (including the eight samples provided by Amato) cut and trimmed with a wet saw before being sent off for whole-rock geochemical analysis. Of the 52 hand samples, 23 thin sections were produced at the National Petrographic Service, INC, in Rosenberg, TX. Trimmed hand samples were sent to Reno, NV's Australian Laboratory Services (ALS) lab for analysis of major and trace elements and precious metals (Pd, Pt, and Au) compositions. Prior to analysis, whole rock samples were crushed in a jaw crusher and pulverized in a ball mill to sizes of <2 mm and <75 μm , respectively, to yield a powder suitable for whole-rock geochemical analysis. This sample preparation used low Cr-steel equipment to avoid contamination from PGE samples and the addition of elements such as W and Co that could be added if W carbide crushing and milling were used; sample preparation duplicates provide little evidence of contamination during sample preparation. Loss on ignition (LOI) values were determined by igniting sample powders in a furnace at 1000°C. Total sulfur and carbon concentrations were determined using unignited powders by induction furnace (IR) heating. Whole rock geochemical data were generated using a variety of different approaches according to the elements of interest. Major element concentrations

reported in oxide wt.% values were determined by lithium borate fusion to generate a fused bead that was then digested using an acid dissolution approach to yield a solution that was used for inductively coupled plasma-atomic emission spectroscopy (ICP-AES). Some trace elements (As, Bi, Hg, In, Re, Sb, Se, Te, and Tl) typically present in refractory minerals were determined using a similar lithium borate fusion approach, again generating a fused bead that was then digested using a 4-acid approach to yield a solution that was used for ICP-mass spectroscopy (ICP-MS). Other trace elements (Ag, Cd, Co, Cu, Li, Mo, Ni, Pb, Sc, and Zn) were determined using 4-acid digestion and ICP-MS. Precious metal concentrations (Pt, Pd, and Au) were determined by standard lead oxide collection fire-assay followed by ICP-MS analysis. The resulting geochemical data and detection limits are reported in Table 1. Analytical accuracy was determined by repeat analysis of OREAS-certified standards 24d, 682, and 684 and USGS GSP-2, with these data also used for the determination of precision along with duplicate analyses of unknowns. The resulting data are all provided in Appendix A. Sample preparation duplicates results are compiled in Appendix B.

IV. PETROGRAPHY

Hand samples range from fine to coarse-grained <10 mm, with phaneritic plagioclase and pyroxene (Figs. 2A and 2B). Microscopic observations indicate that these samples are typically fine to coarse-grained with ophitic to subophitic textures defined by plagioclase (~50 μ m - ~300 μ m wide) enclosed by clinopyroxene. The SWLLIP diabase mineralogy typically consists of plagioclase, clinopyroxene, +/- olivine, +/- orthopyroxene, and Fe-Ti oxides, with minor amounts of apatite (Fig. 3 in Appendix A). Clinopyroxene is the coarsest minerals and partially or fully enclose plagioclase (Fig. 3A). Plagioclase laths average ~300 μ m across and olivine, where present, is similar in size and is semi-rounded, with some olivine having reaction rims adjacent to plagioclase and pyroxenes (Fig. 3A and 3B). Some SWLLIP samples from Death Valley, CA, have a partial replacement of primary mineralization like augite and olivine (Fig. 3C). Alteration products include chlorite, serpentine, hornblende, magnetite, epidote, and biotite, which tend to replace the mafic mineralization. The main alteration of plagioclase is sericitization, which is most evident in the thin sections from Death Valley (Fig. 3D). A few samples near the Burro Mountains contain locally derived xenoliths from the surrounding country with secondary sulfide minerals within the brecciated contact (Fig. 3E). Minor amounts of sulfide phases, typically pyrite or pyrrhotite and chalcopyrite, are also present (Fig. 3F).

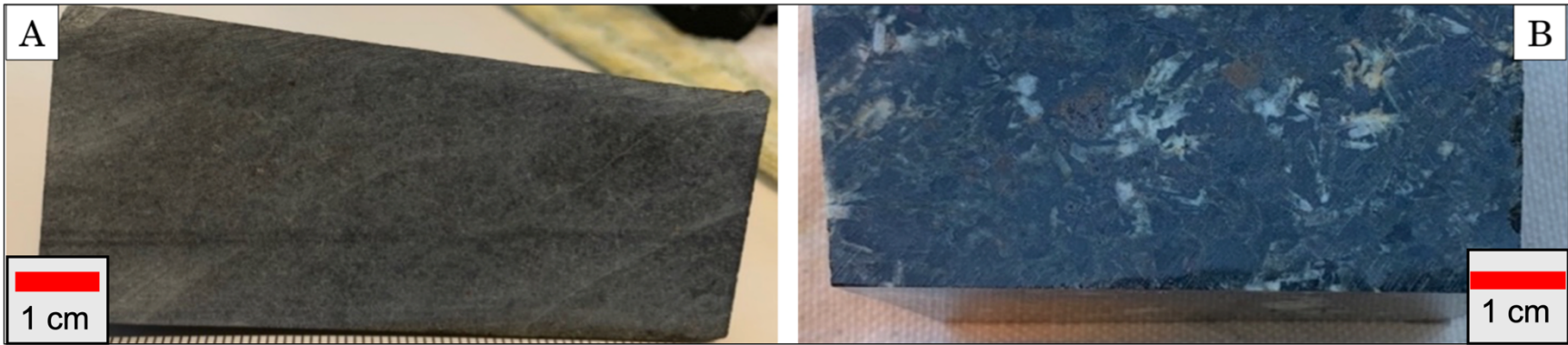


Figure 2. Hand samples from SWLLIP. Samples from Death Valley showing representative examples of aphanitic (sample TB028 in A) and phaneritic (sample TB026 in B) textures seen throughout the SWLLIP.

V. GEOCHEMISTRY

Post-crystallization weathering and interactions with hydrothermal fluids or meteoric water can cause alteration and geochemical mobility (e.g., Zhong et al., 2023), meaning that prior to investigating the petrogenesis and igneous processes involved in SWLLIP formation, it is important and the mobility of major and trace elements during post-magmatic alteration. High-field strength elements (HFSE) (Hf, Zr, Ti, Nb, Th, La, Ta, and Y) are unlikely to be mobile (Linnen and Keppler, 1997, 2002; Jiang et al., 2005; Condie and Shearer, 2019)(Fig. 4), and are often used in determining aspects like the tectonic setting of metamorphosed or significantly altered mafic and felsic units (Pearce et al., 1984; Pearce, 1996; Salters, 2011). When using trace elements discrimination diagrams, it is important to use the trace elements and the rare earth elements (REE) that can be normalized to mantle values. Trace element (e.g., Zr and Nb) data alone is not enough for assessing basaltic rocks, mainly their tectonic environments (e.g., mid-ocean ridge basalt vs. back-arc basin basalt), but when coupled with REE (La-Lu) that are plotted on mantle-normalized trace element diagrams, it can further discriminate between various tectonic settings (Li et al., 2015).

The presence of variable amounts of alteration within the SWLLIP samples analyzed during this study means that the classification and petrogenetic diagrams used during this study focus on immobile elements, negating any potential misclassification associated with any major element mobility and the use of diagrams such as total alkali-silica (TAS) plots. Specifically, Fig. 4 uses ratios of

immobile elements (e.g., Nb/Y vs. Zr/Ti), thus removing the effect of any cumulus accumulation of minerals such as olivine and plagioclase (Jowitt et al., 2014).

Plotting the SWLLIP samples on a Nb/Y vs. Zr/Ti classification diagram indicates the majority are basalts, with 9% of the samples classified as basaltic andesites (after (Winchester and Floyd, 1977; Pearce, 1996) diagram (Fig. 4).

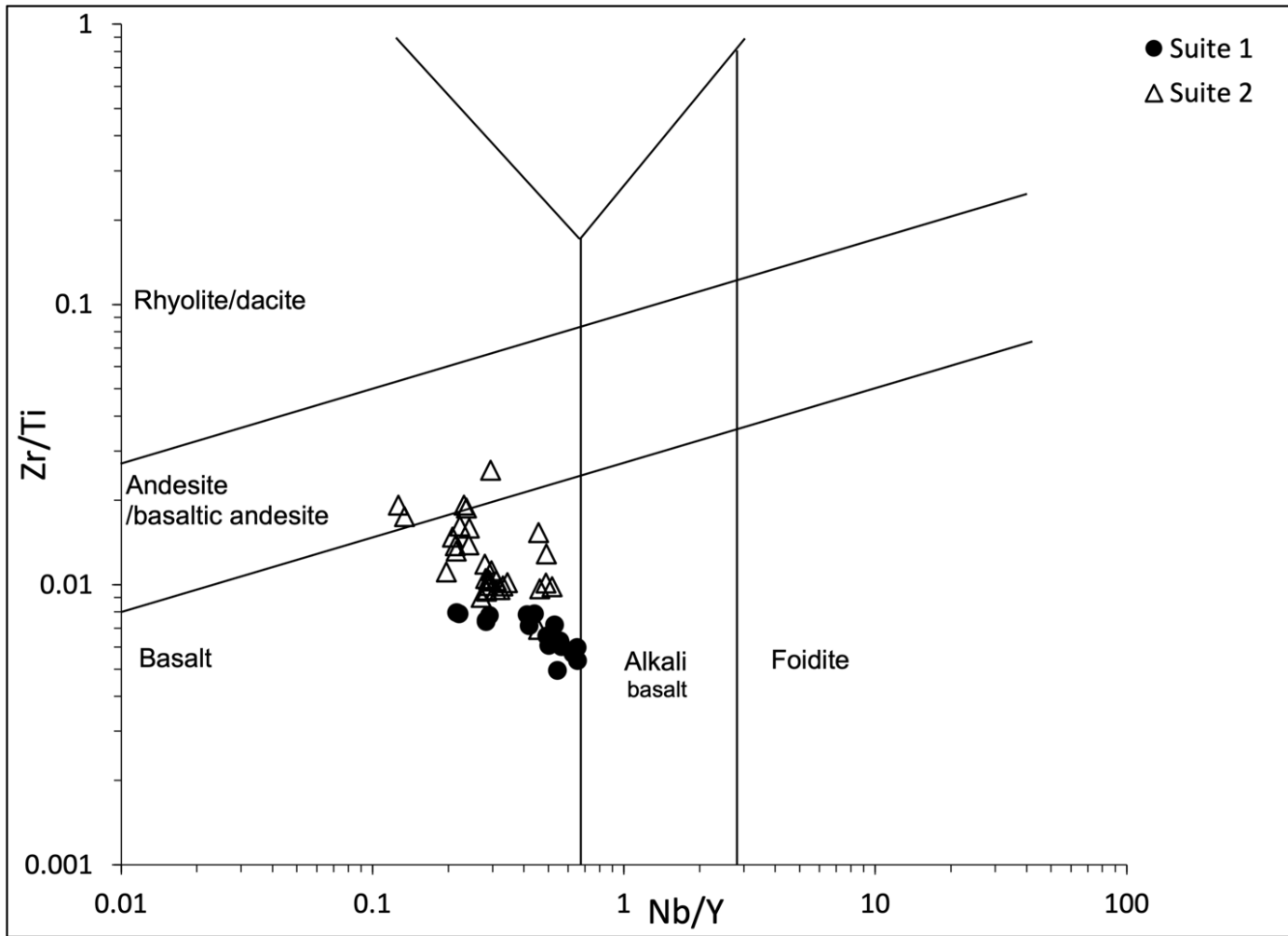


Figure 4. Nb/Y vs. Zr/Ti basalt classification diagram. The Nb/Y vs. Zr/Ti diagram (Pearce,1996) shows the SWLLIP sample distribution and basaltic affinities; the suite classification used here is described later in the text.

The two groupings evident in Fig. 4 are consistent with the presence of two suites within the SWLLIP samples analyzed during this study. Various authors have widely noted the varying composition of the SWLLIP diabase (Hammond, 1986; Bright, 2012; Hammond-Gordon et al., 2022). This classification is further examined using a tholeiitic vs alkaline affinity discrimination diagram employing variations in Nb/Y and Zr/P₂O₅ (Fig. 5)((Floyd and Winchester, 1975; Winchester and Floyd, 1977; Rollinson, 1993). The results of this study highlight two geochemically distinct diabase suites (Fig. 5): a mildly alkaline diabase suite (hereafter referred to as Suite 1) and tholeiitic diabase (hereafter referred to as Suite 2).

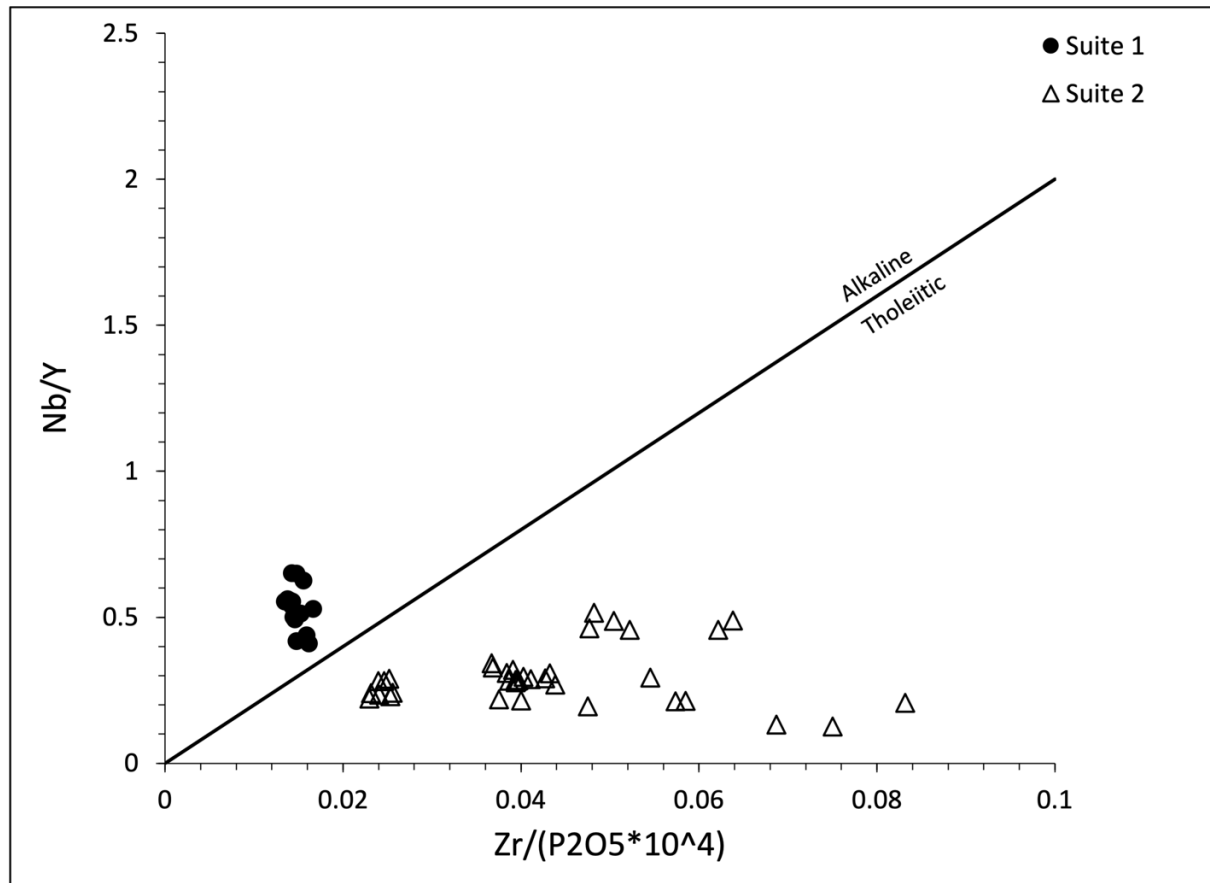


Figure 5. Nb/Y vs. Zr/P₂O₅ tholeiitic and alkaline discrimination diagram. From Rollinson, 1993, adapted from Floyd and Winchester, 1975, and Winchester and Floyd, 1976. This diagram shows the division of SWLLIP samples into mildly alkaline and tholeiitic suites.

Notably, Fig. 8 in Hammond (1990) plots Ba/Zr against P/Zr to distinguish the diabase samples, which also fall into two groupings that are similar to this study's grouping. It is important to note that Suite 1 identified in Fig. 5 is not silica-undersaturated alkaline basalt but rather a transitional alkali basalt composition, such as those within the Western Snake River Plain (Servais and Vetter, 2009). This classification is also consistent with spatial variations within the SWLLIP and the two distinct pulses from Mohr et al. (2024), with Suite 1 isolated in the Colorado River region with Suite 2 samples located in Arizona, New Mexico, and California, including five samples from sheets within the Suite 1 region.

Further subdivision of the diabase samples was attempted using Ti/ V values since basaltic rocks have measurable quantities of Ti and V (HFSE). Moreover, these elements are considered immobile, therefore making them ideal for assessing the tectonic setting of the magmatic suite (Shervais, 1982). Suite 1 has Ti/V values between 20 and 50, and plots in the central field of Shervais (1982) are indicative of plotting as back-arc-basin basalts (BABBs) and continental flood basalts (CFBs) fields (Shervais, 1982; Fig. 6). Suite 2 has varying Ti/V concentrations, with 12 samples having Ti/V values between 20 and 50 and plotting in the CFB type. One sample (TBJA03) has a low Ti/V ratio (<20), plotting just within the island-arc basalt (IAB) field, while three samples (TB038B, TB038M, TB038T) contain > 100 Ti/V (Fig. 6). The remaining 21 Suite 2 samples plots in the ocean-island basalt (OIB)/ alkali basalt field with Ti/ V values between 50 and 100 (Fig.6).

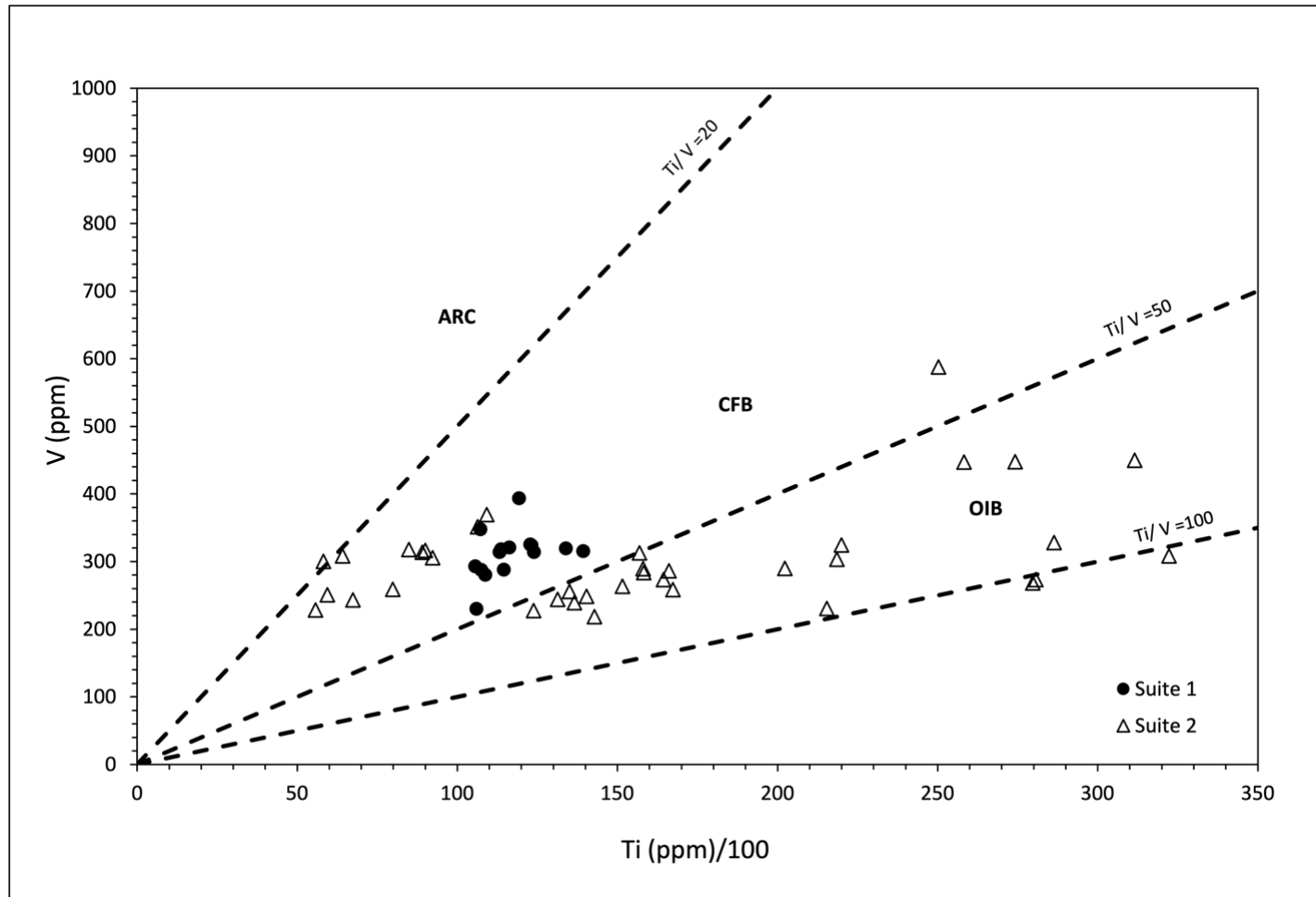


Figure 6. Ti vs. V diagram. SWLLIP samples from this study vary on a Ti vs. V diagram (after Shervais, 1982). Suite 1 plots uniformly within the (CFB) field, while Suite 2 Ti/V concentrations range from CFB to OIB. Note the higher Ti contents of Suite 2 samples are also some of the most crustal contaminated samples seen in crustal contamination diagrams.

The SWLLIP suite division can be further evaluated on a $(\text{Tb}/\text{Yb})_{\text{PM}}$ vs. $(\text{La}/\text{Sm})_{\text{PM}}$ (modified from Wang et al., 2002) diagram, which can assess the depth of the source region along with crustal contamination and source enrichment of the melt (Fig 7)(where PM denotes normalization to primitive mantle values of McDonough and Sun, 1995). Analyzing LREEs (e.g., La and Sm) can help determine source enrichment and the degree of crustal contamination due to La being less compatible within the mantle than Sm; thus, the La/Sm concentration of a melt decreases as a melt fraction increases (Lightfoot et al., 1993; Ball et al., 2021). The La/Sm ratios are also a proxy for crustal contamination (Hollings et al., 2010; Wallace et al., 2015), the degree of melting because of the relative incompatibility of LREE in mantle rocks (Pinti, 2011), and relative enrichment in most crustal rocks (Rudnick and Gao, 2013). Heavy REE (HREE) (e.g., Tb and Yb) are preferentially incorporated into garnet relative to spinel so that melts generated within the garnet stability field (i.e., from garnet lherzolites) will have higher Tb/Yb ratios as long as the melting that occurs in the source region for these magmas occurred at low degrees of partial melting, leaving garnet in the source region (Wang et al., 2002; Jicha et al., 2009). Suite 1 samples generally plot within the spinel lherzolite field, with one sample (TB001) plotting just inside the garnet lherzolite field (Fig. 7). Suite 1 samples have <2 $(\text{La}/\text{Sm})_{\text{PM}}$ values with one sample (TB005) plotting with ~ 2.4 $(\text{La}/\text{Sm})_{\text{PM}}$ (Fig. 7). Suite 2 has a broad range of $(\text{Tb}/\text{Yb})_{\text{PM}}$ and $(\text{La}/\text{Sm})_{\text{PM}}$ ratios compared to Suite 1 samples. Five samples from Suite 2 plot within the garnet lherzolite field, while the remainder plot in the spinel

lherzolite field. (Fig. 7). Suite 2 samples have similar (La/Sm) PM ratios to Suite 1, with only four samples plotting below Suite 1 (La/Sm)PM ratios. Two samples from Suite 2 have (La/Sm)PM values >2 (samples TBJA04 and TB021a), the latter having the study's highest (La/Sm) PM value of 3.194 (Fig. 7).

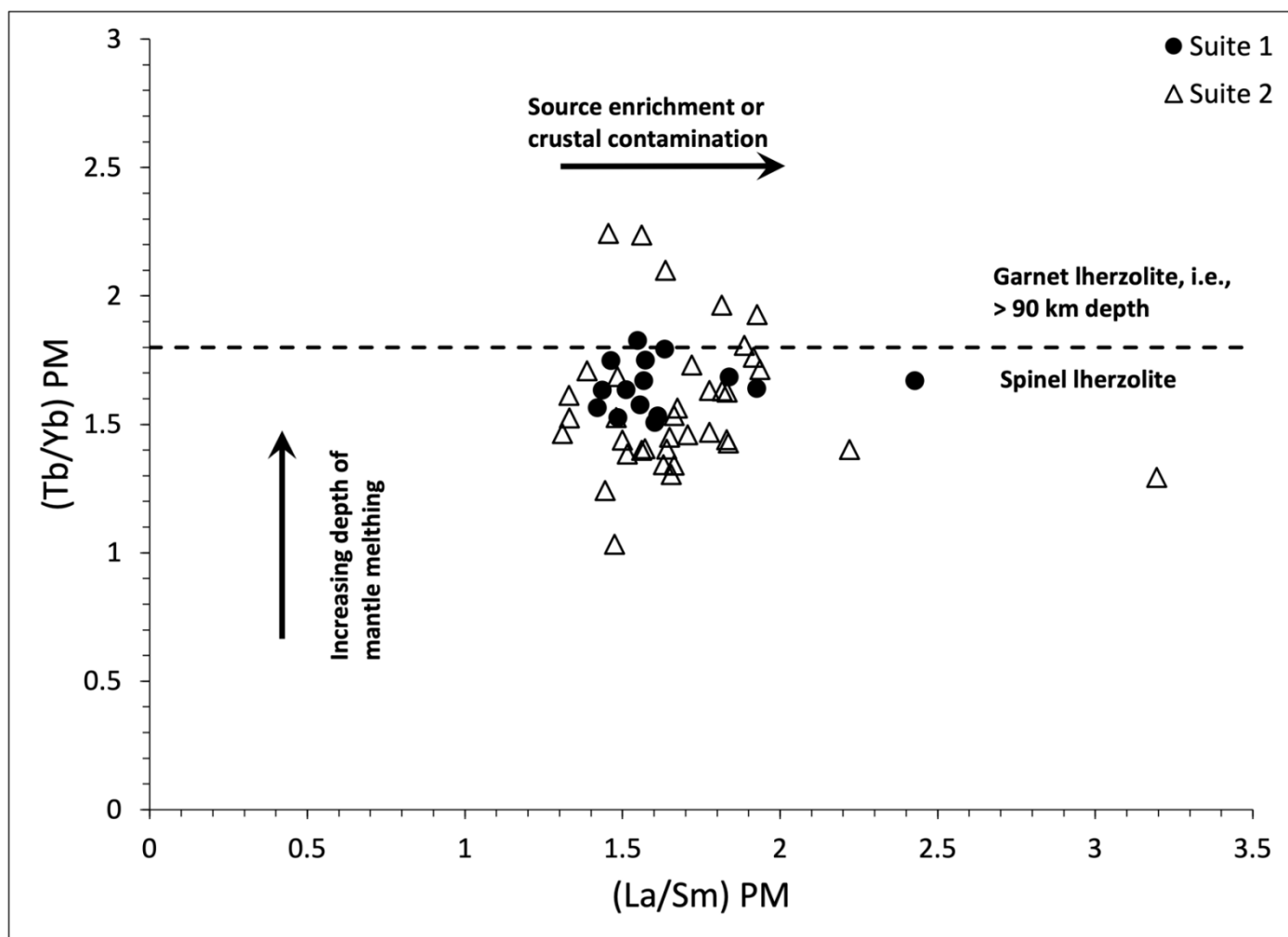


Figure 7. Diagram (Tb/Yb) PM and (La/Sm) PM. This diagram shows variations within the SWLLIP samples, where PM denotes normalization to primitive mantle values of McDonough and Sun (1995); the discrimination line between magmas sourced from the melting of spinel peridotite mantle and garnet peridotite mantle is after Wang et al. (2002). Note that the cluster of Suite 1 samples indicates a smaller degree of partial melting, while Suite 2 samples show both shallow and deep mantle sources. The outliers in (La/Sm)PM are suggestive of higher degrees of crustal contamination within individual intrusion within the SWLLIP rather than a change source enrichment.

Similar trends in major element variation diagrams (Fig. 8 in Appendix B) are seen in both suites, indicating their use was limited in further classifying them. Samples' MgO values range from 3.06-10.46 wt.%. The majority of Suite 1 samples cluster in most major element variation diagrams in Fig. 8, but CaO positively correlates with MgO, while Fe₂O₃, Na₂O, P₂O₅, and TiO₂ negatively correlate to MgO. Suite 2 samples show more variation in major element concentrations compared to Suite 1 but show similar correlations between major elements and MgO with the exception of P₂O₅ (Fig. 8). Suite 2 samples show a negative correlation between P₂O₅ and MgO but at a lower trend line than Suite 1 (Fig. 8F.) Five Suite 2 samples show elevated P₂O₅ values compared to the rest of the SWLLIP samples, these five samples are different than the five elevated samples of (Tb/Yb)_{PM} from Fig. 7.

Mantle-normalized trace element diagrams paired with trace element discrimination diagrams allow for more efficient discrimination in basalts (Li et al., 2015). Figure 9 demonstrates the difference between the two identified suites and identifying outliers within individual intrusions within the suites with known magma compositional endmembers from Sun and McDonough, 1989. Suite 1 trace elements are uniform, with only a few samples demonstrating large ion lithophile elements (LILEs) anomalies (Pb and Rb) and one sample (TB012) plotting with a negative Sr anomaly. Suite 1 is characterized by an enrichment in LILE and no Nb and Ta anomalies, unlike Suite 2, which has Nb and Ta anomalies and depletion in LILE relative to HFSE.

Samples that are classified as Suite 2 have both LILE positive and negative anomalies (Fig. 9B). Geochemical discrimination of the SWLLIP samples was not based on LILE. Still, it was used to assess various outliers in geochemical data. Suite 2 samples have higher concentrations of trace elements compared to Suite 1, except for four samples that are characterized by low trace elemental values and negative Nb, Ta, P, and Ti anomalies. The five Suite 2 samples from the Colorado River area show a similar enrichment of LILEs and Nb-Ta trends as Suite 1 but have positive K and Sr anomalies, like Suite 2.

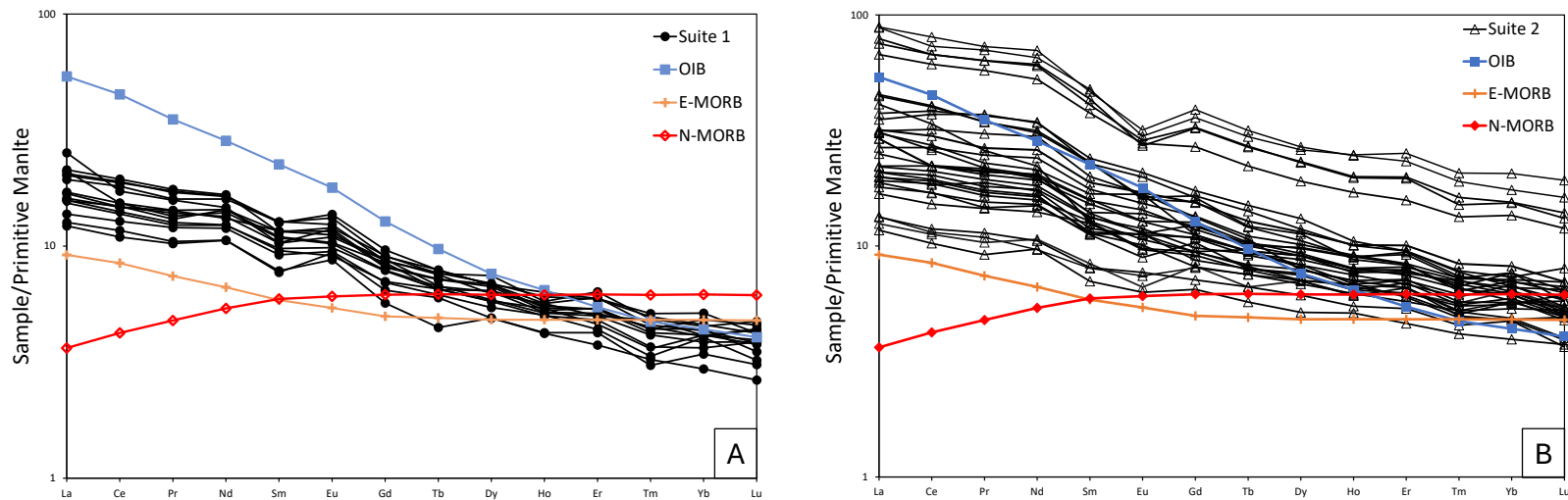


Figure 9. Multi-element variation diagrams normalized to primitive mantle values. Samples are divided by suite: (A) Suite 1 samples and (B) Suite 2 samples. Mantle values from McDonough and Sun (1995). Ocean island basalts (OIB), normal mid-ocean ridge basalts (N-MORB), and enriched mid-ocean basalts (E-MORB) compositions are from Sun and McDonough, 1989.

Magnesium is a valuable proxy for comparing MgO concentrations with chalcophile element concentrations to examine the relative importance of differentiation and fractionation processes versus those associated with immiscible sulfide formation (Figs. 10A-D). Suite 1 samples plot uniformly along the within-plate basalt array of Keays and Lightfoot (2007) on a Ni vs. MgO diagram (Fig. 10A). Suite 1 samples have similar Cu and MgO concentrations, except for one sample (TB005) with ~182 Cu ppm, the second highest of all samples from this study (Fig. 10B). Suite 2 varies in Ni and MgO concentration much more than Suite 1, nevertheless, Suite 2 mostly plots along the array (Fig 10A). Two samples (TB031 and TB035) from Death Valley plot among the highest MgO concentrations of all the samples but only have average Suite 2 Ni values (Fig. 10A). The significant variation of Cu values in Suite 2 is demonstrated in Fig 10B. There is a weak positive correlation between Cu and MgO concentrations in Suite 2 (Fig. 10B). Six samples from Suite 2 have above-average Cu values compared to Suite 1, while the remainder of Suite 2 samples plot at or below-average Cu values of Suite 1 samples. Suite 2 sample (TB031) is from a >100m sill in Death Valley and has the highest Cu concentration of the study at ~ 217 ppm (Fig. 10B).

Regarding chalcophile distribution, Pt and Pd (ppb) values exhibit more variability than Ni and Cu (ppm) values within Suite 2 (Fig. 10A-D). Four samples from Suite 2 have Pd and Pt concentrations >10 and >9 ppb and reach concentrations of ~14.35 and 15.16 ppb, respectively (Fig. 10C, D). These samples will be referred to as the undepleted samples for the remainder of the paper. It is

worth noting that these four samples also have some of the highest Ni and Cu concentrations in this study (Fig. 10A, B). Around half the remaining Suite 2 samples have Pt and Pd values higher than Suite 1 (Fig. 10C, D). The remaining Suite 2 samples demonstrate a depletion in Pt and Pd concentrations, plotting either in the Suite 1 range or below and a weak positive correlation to MgO (Fig 10C, D). Suite 1 samples exhibit tight clustering of Pt and Pd, no correlation to MgO concentrations, and no significant change in chalcophile element distribution (Figs. 10 A- D).

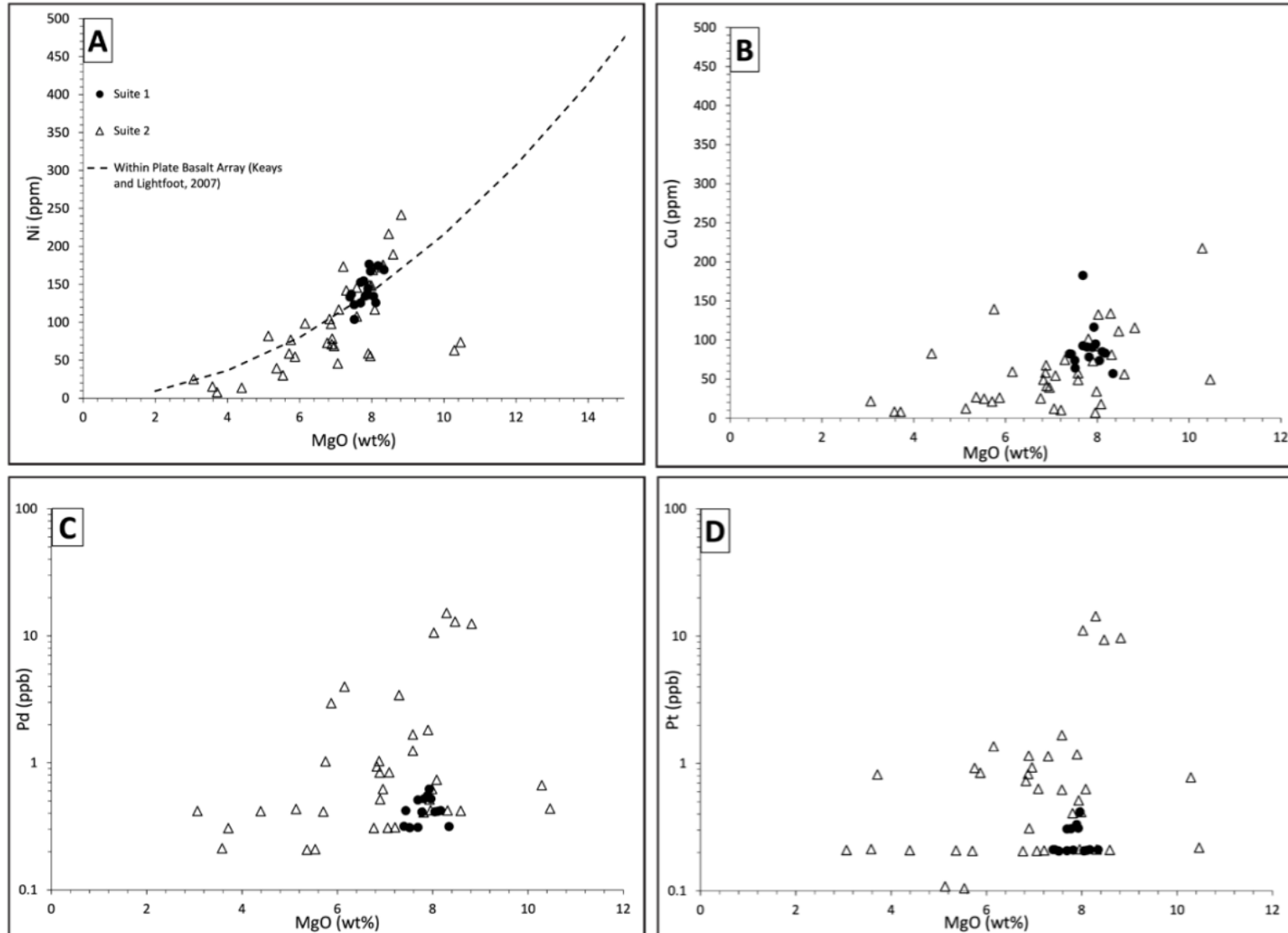


Figure 10. Diagrams showing the chalcophile element variations within the SWLLIP showing Ni (A) Cu (B), Pd (C), and Pd (D) variations compared to MgO concentrations. Dashed line (A) is the within-plate basalt array of Keays and Lightfoot (2007).

Chalcophile elements like Cu and Pd, which normally behave incompatibly in S-undersaturated mafic systems (Keays, 1995), can be normalized with incompatible elements such as Zr and Yb (Jowitt, 2014). Normalizing incompatible elements against chalcophile elements separates the sulfur saturation and differentiation influences that occur during magmatic differentiation, for in sulfur-undersaturated melts, Cu, Pd, Zr, and Yb are increased at a constant rate, but during S-saturate events, Cu and Pd values decrease due to their affinity to sulfides over silicates (Naldrett, 2010a; Jowitt et al., 2014). Partition coefficients for Cu and Pd between sulfide liquid and silicate melt are 1,383 and >23,400, respectively (Peach et al., 1990). The ratios Cu/Zr and Pd/Yb thus can be used to assess the sulfur saturation history of the suites. Suite 1 demonstrates a tight clustering in (Cu/Zr) PM and (Pd/Yb) PM ratios and shows no correlation to MgO concentrations (Figs. 11A, B). However, Suite 2 samples exhibit a wide range of (Cu/Zr)PM and (Pd/Yb)PM ratios and a weak positive correlation between MgO concentrations (Fig. 11A, B). Nine Suite 2 plot within Suite 1 cluster, while the rest plot below Suite 1 values (Cu/Zr) PM (Fig. 11A). Those nine Suite 2 samples, including the four undepleted samples, plot above Suite 1 (Pd/Yb)PM ratios (Fig. 11B). The remaining Suite 2 samples plot at or below Suite 1 (Pd/Yb)PM ratios (Fig. 11B).

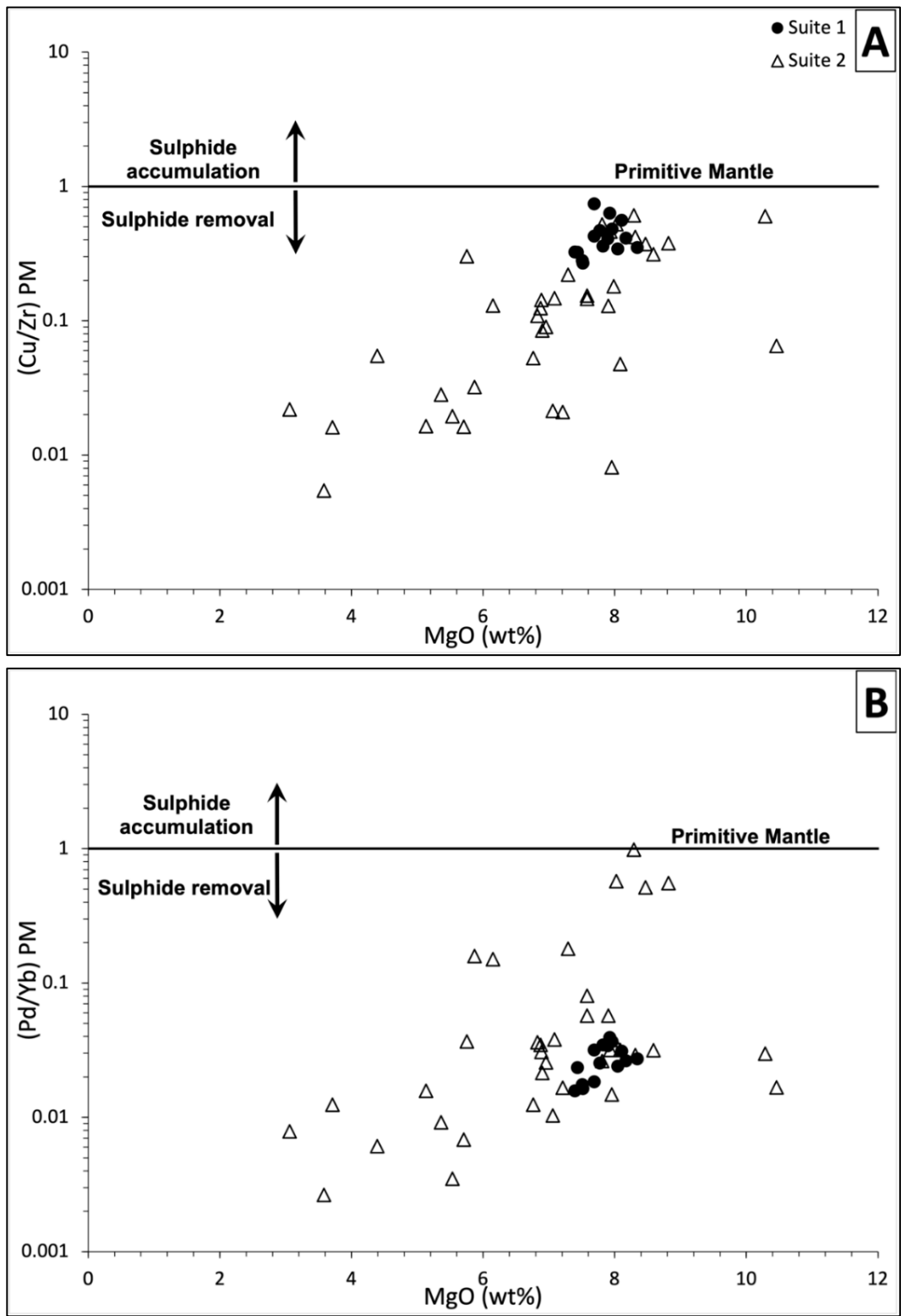


Figure 11. Diagrams showing variation in $(\text{Cu}/\text{Zr})\text{PM}$ (A) and $(\text{Pd}/\text{Yb})\text{PM}$ (B) ratios with MgO concentrations. Ratios are normalized to primitive mantle values of McDonough and Sun (1995).

Crustal contamination is the primary process in allowing for sulfur saturation to occur within a magmatic system and can be assessed by using an (Nb/Th)_{PM} vs (Th/Yb)_{PM} diagram allowing for the diabase to be evaluated alongside established mantle values (e.g., normal mid-ocean ridge basalt [N-MORB]) (Hofmann, 1988) and crustal components, represented by the average lower continental crust (LCC) composition and the average upper continental crust (UCC) components (Taylor and McLennan, 1985) (Fig. 12). Assessing the Nb concentrations with a similar compatibility element like Th allows for assessing the Nb anomaly, while evaluating a highly incompatible element (e.g., Th) to a moderately incompatible element (e.g., Yb) can discriminate between mantle-derived melts and crustal rocks (Wang et al., 2006). Mantle-derived melts will have lower (Th/Yb)_{PM} ratios and higher (Nb/Th)_{PM} than crustal rocks. Suite 1 has constant (Th/Yb)_{PM} ratios while their (Nb/Th)_{PM} values vary (Fig. 12). Suite 2 shows a wide variation with a majority of samples clustering around LCC composition, while six samples trend toward UCC composition (Fig. 12). Two samples (TB040 and TB041) from Suite 2 are from western New Mexico, the furthest samples east in this study, plot within Suite 1 field (Fig. 12). The four undepleted samples of Suite 2 have some of the lowest (Nb/Th)_{PM} and (Th/Yb)_{PM} ratios from this study (Fig. 12).

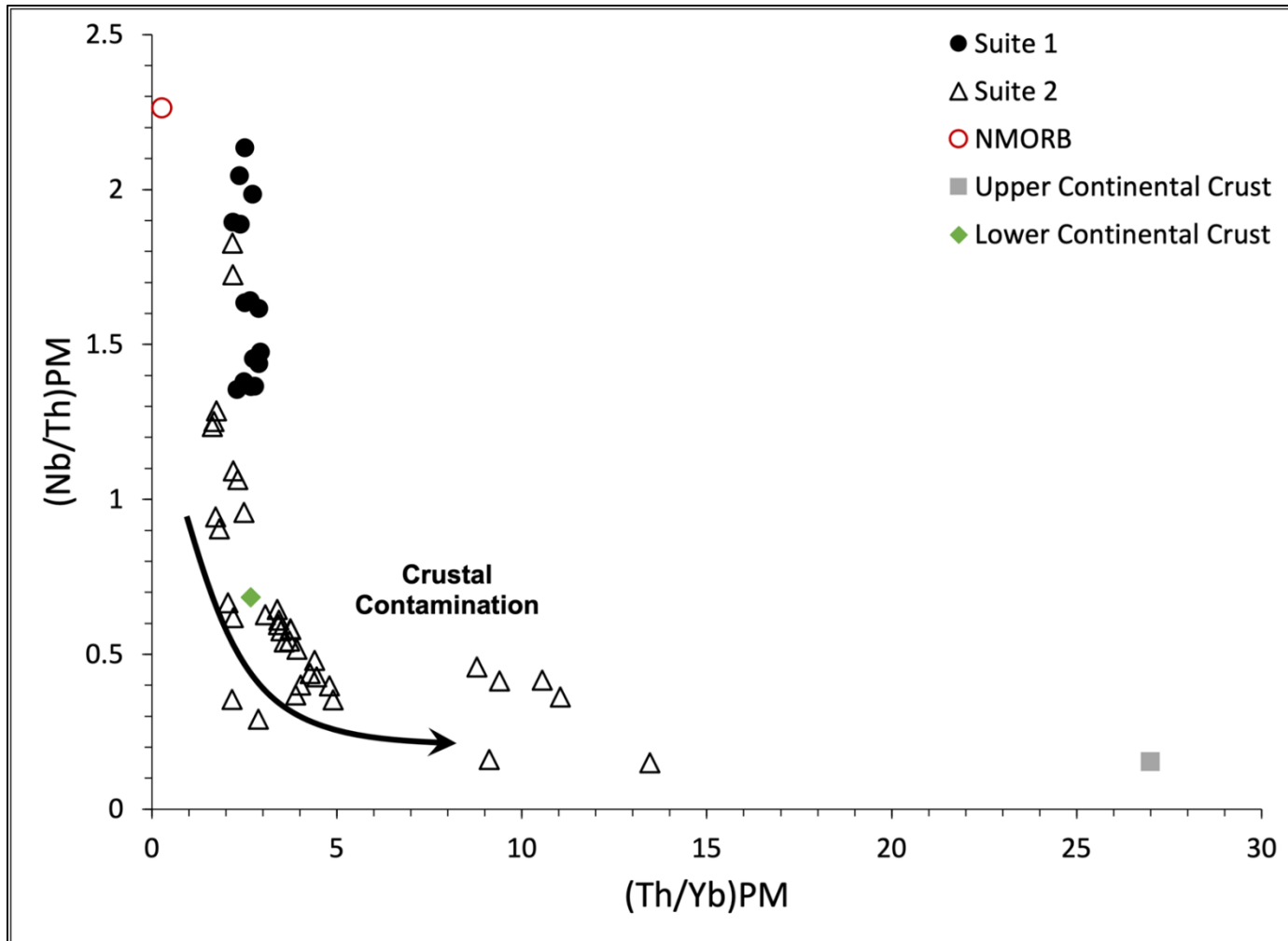


Figure 12. Diagram $(\text{Nb}/\text{Th})_{\text{PM}}$ and $(\text{Th}/\text{Yb})_{\text{PM}}$. Ratios are normalized to primitive mantle values of McDonough and Sun (1995), N-MORB composition is from Hofmann (1988), and average lower continental crust (LCC) and upper continental crust (UCC) composition is from Taylor and McLennan (1985). Note Suite 1 shows no change in $(\text{Th}/\text{Yb})_{\text{PM}}$, which indicates limited crustal assimilation, while Suite 2 clusters around LCC values.

Further analyses of chalcophile element distribution and crustal contaminant can be assessed using (Cu/Zr) PM and (Pd/Yb) PM vs. (Th/Yb)PM (Fig 13A, B), where (Cu/Zr) PM and (Pd/Yb) PM are indicative of chalcophile element depletion or enrichment while (Th/Yb)PM values are representative of crustal contamination (Jowitt et al., 2014). Samples classified as Suite 1 exhibit similar (Cu/Zr) PM and (Pd/Yb) PM vs. (Th/Yb)PM concentrations with no outliers (Fig. 13A and B).

The chalcophile element distribution and crustal contamination vary in Suite 2, with some units showing a substantial depletion while others show none to slight depletion within chalcophile elements (Fig 13A and B). The undepleted samples of Suite 2 plot within Suite 1 (Cu/Zr)PM ratios and show little crustal contamination, unlike the rest of Suite 2 (Fig 13A). Six samples from Suite 2 have >8 (Th/Yb)PM (Fig. 13A and B). Suite 2 shows a weak negative correlation between (Cu/Zr) PM ratios and (Th/Yb)PM values (Fig. 13A). Suite 2 samples have a wide range of (Pd/Yb)PM, still around half cluster around Suite 1 (Fig. 13B). Ten samples from Suite 2 have elevated (Pd/Yb)PM compared to the rest of the samples of this study with four plotting close to primitive mantle values (McDonough and Sun, 1995)(Fig. 13B). Interestingly, five additional Suite 2 samples have the lowest (Pd/Yb) PM values of the study with only slightly elevated (Th/Yb) PM compared to the rest of the samples (Fig. 13B). Further evidence of the depletion of chalcophile elements in Suite 2 is shown by a weak negative correlation between (Pd/Yb)PM and (Th/Yb)PM values (Fig. 13B). Suite 2 samples with the highest (Cu/Zr)PM and (Pd/Yb)PM have some of the lowest (Th/Yb)PM ratios, indicating a correlation

between sulfur saturation and crustal contamination and the depletion of chalcophile elements from the silica melt (Fig. 13A and B). Furthermore, Suite 2 samples that have the highest (Th/Yb)_{PM} values do not have the lowest (Cu/Zr)_{PM} and (Pd/Yb)_{PM} values.

It is crucial to scrutinize the crustal contamination within the diabase along with the melt's source region, which affects the initial chalcophile element budget that determines whether a melt is fertile or unfertile in chalcophile elements. The melt's source region and crustal contamination can be assessed using a (Th/Yb)_{PM} vs. (Nb/Yb)_{PM} diagram. Suite 1 plots within mantle-derived melts field and shows little change in the (Th/Yb) PM ratio (Fig. 14). Suite 1 samples range from ~3.1-5.4 (Nb/Yb) PM values plotting between enriched mantle 1 (EM1) and MORB compositions (Fig. 14). Suite 2 samples plot within or close to the mantle-defined boundary with various plotting with increasing (Th/Yb) PM ratio (Fig. 14). Six samples from Suite 2 plot toward the UCC composition, five being from Death Valley, and one from Garnet Mountains, indicating significant crustal contamination within Suite 2 (Fig.14). Two samples from Suite 2 plot within the Suite 1 ratios (TB040 & TB041) (Fig. 14). The cluster of Suite 2 samples around LCC compositions is an indication to the assimilation of crustal material at lower portions within the SWLLIP.

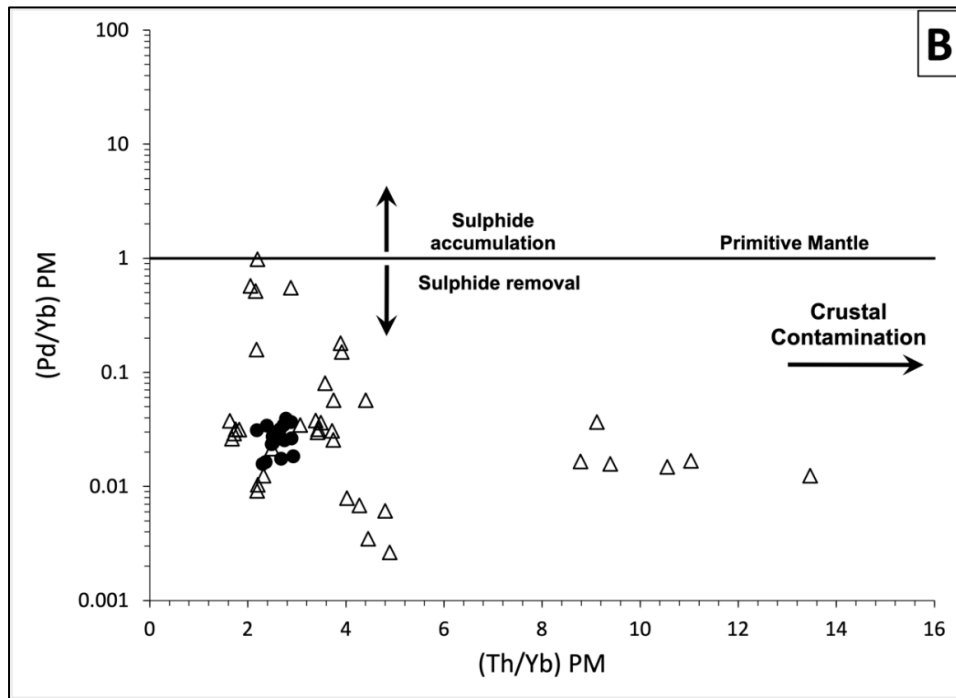
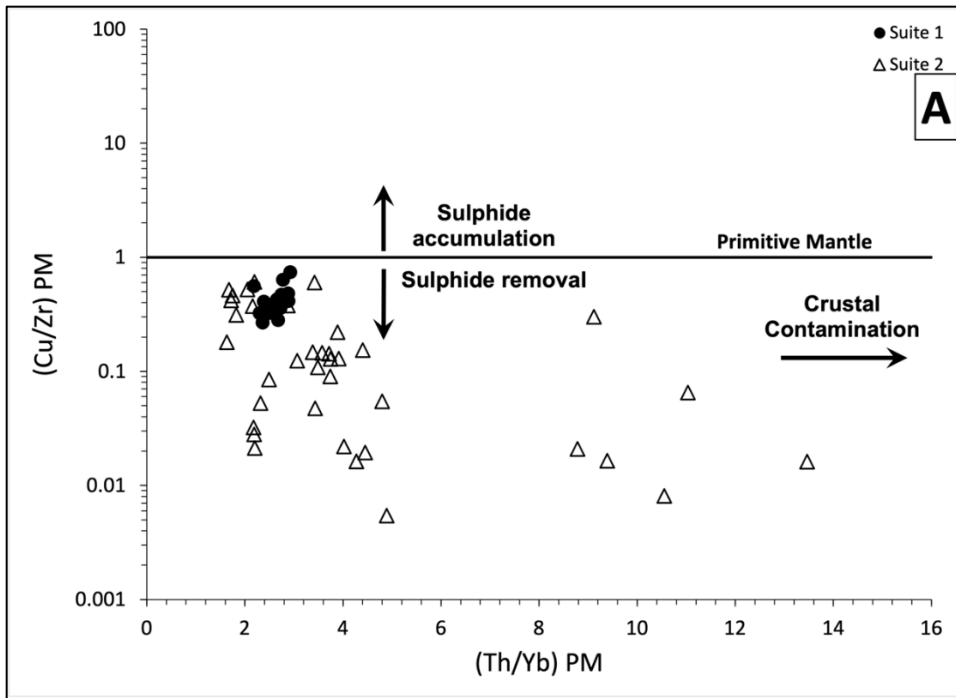


Figure 13. Diagram (Cu/Zr)PM (A) and (Pd/Yb)PM (B). Diagram showing variations in (Cu/Zr)PM (A) and (Pd/Yb)PM (B) ratios with (Cu/Zr)PM ratios within the SWLLIP, indicative of chalcophile element enrichment or depletion, and (Th/Yb)PM ratios indicative of assimilation of crustal material and crustal contamination of the SWLLIP samples; ratios are normalized to primitive mantle values of McDonough and Sun (1995).

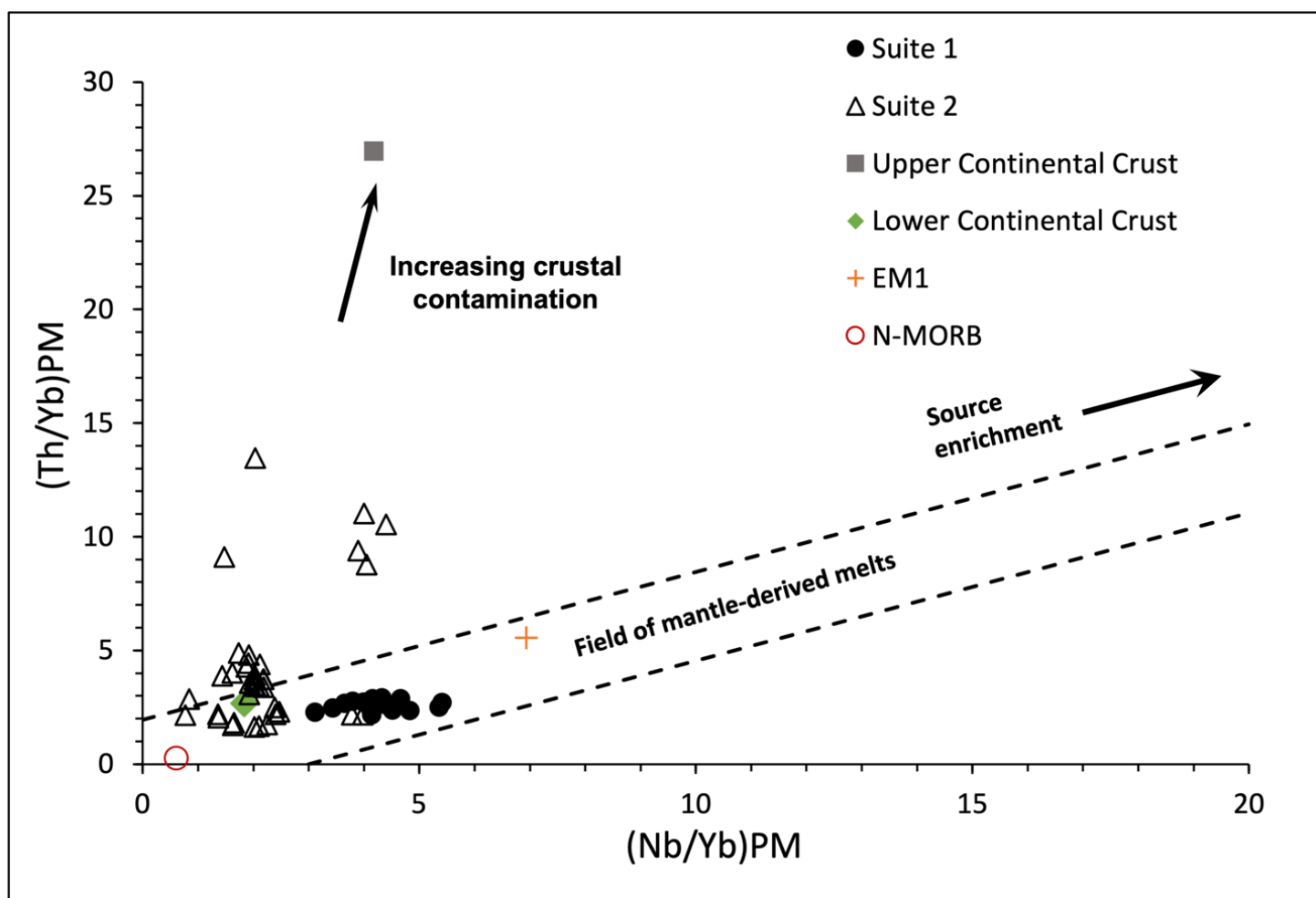


Figure 14. Diagram (Nb/Yb)PM and (Th/Yb)PM. Diagram showing variations in SWLLIP samples Adapted from Pearce, 2008; ratios are normalized to primitive mantle values of McDonough and Sun, 1995, with EMI compositions from Condie, 2001; N-MORB composition is from Hofmann (1988); and average lower continental crust (LCC) and upper continental crust (UCC) composition from (McLennan, 2001) modified from Taylor and McLennan (1985).

The sulfur saturation history considers the initial chalcophile element concentration from the melt generation and the degree of crustal contamination, notably the addition of sulfur, which would cause a sulfur saturation to occur, thus removing the chalcophile elements from the silicate portion of the magmatic system. To scrutinize the sulfide and silicate interaction and the degree at which chalcophile elements were either removed or accumulated from the melt can be assessed on a Cu/Pd vs. Pd diagram (adapted from Barnes and Maier, 1999) (Fig. 15). Suite 1 plots uniformly with Cu/Pd values with one outlier (TB005) with high Cu concentrations (182 ppm) (Fig. 15). When analyzing silica and sulfide melt interaction of Suite 2, it is evident of various degrees of sulfide and silicate interaction. Suite 2 shows significant variation in Cu/Pd ratio and Pd concentrations, with the majority of samples trending toward sulfide removal (Fig. 15). Seven samples, four being the undepleted samples, plot close to primitive mantles values (e.g. chalcophile element undepleted) (Fig. 15). The remaining three samples, in decreasing Cu/Pd values, are from the Hualapai Mountains, Death Valley, and Burro Mountains.

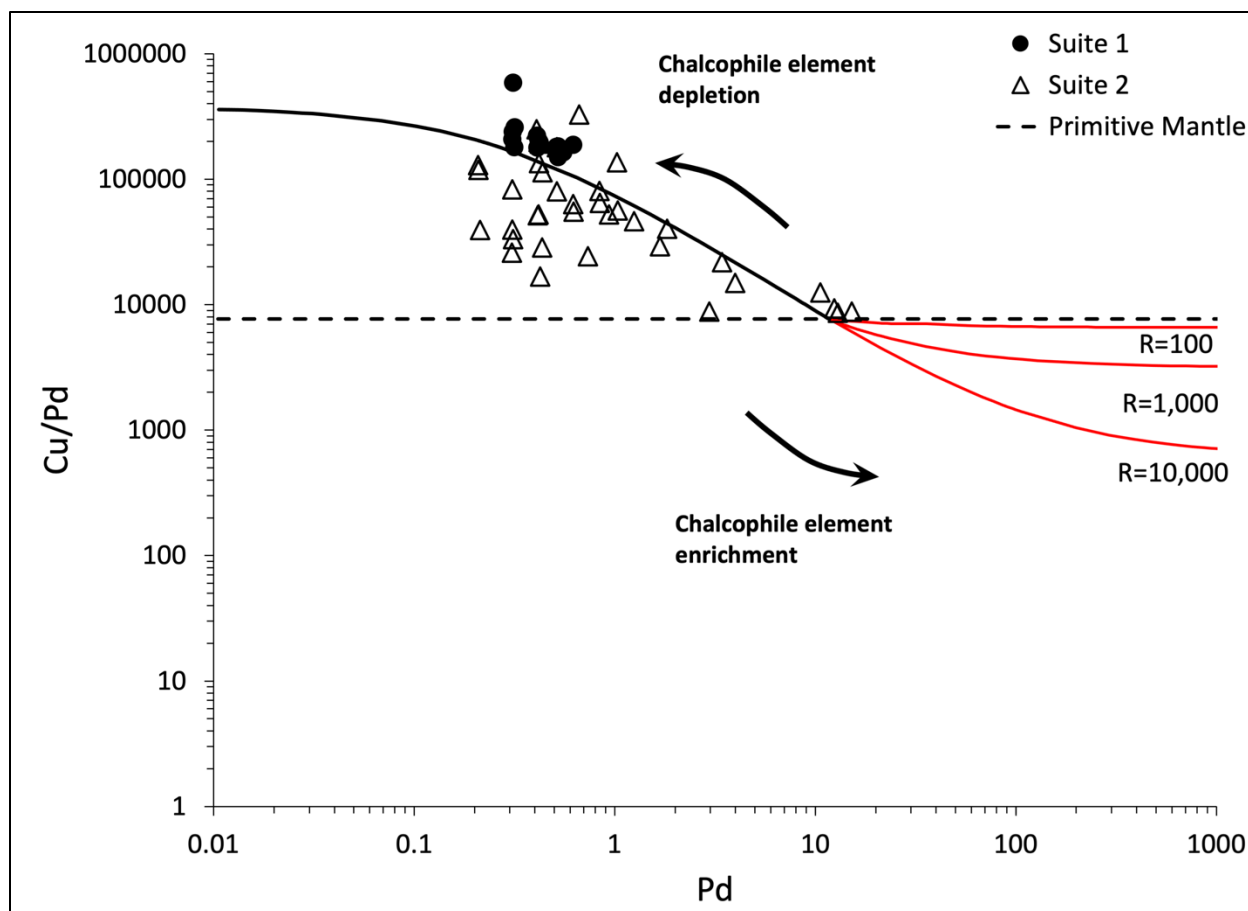


Figure 15. Diagram showing variation in Cu/Pd ratios compared to Pd concentration. The solid line to the left corresponds to a modeled magma undergoing equilibrium fractionation and removal of immiscible sulfides from a primary melt containing ~10 ppb Pd and ~100 ppm Cu (after Barnes et al., 1993). The solid lines to the right of the diagram correspond to R-factors (Campbell and Naldrett, 1979) of 100, 1,000, and 10,000, respectively. Note the chalcophile element depletion trend of Suite 2.

VI. DISCUSSION

Using geochemical proxies established by previous studies of magmatic intrusions allows for assessing the petrogenesis of the SWLLIP, building a deposit model for magmatic sulfide mineralization or lack thereof in this area, and detailing the regional tectonic implications of the emplacement of this LIP. Two suites, a transitional alkali and a tholeiitic suite, are observed in our sample set and correlate to the main magmatic pulses.

Genesis of the SWLLIP magmas

The petrogenesis of the diabase can be assessed using elemental ratio (e.g., (Tb/Yb)_{PM}) comparisons to evaluate potential melt source region characteristics (e.g., source region and source enrichment). Several authors have suggested various models for the petrogenesis of the SWLLIP. Hammond-Gorden et al. (2022) suggest hydrous melting associated with a stagnant slab could have various melts ponding beneath the lithosphere before being emplaced in the upper crust from extensional faulting, though the cause of extension is unclear in this model. Mosher et al. (2008) suggested subduction during the Greenville orogeny allowed for thickening and heating of the lithosphere followed by slab breakoff, allowing for the upwelling of mafic magmatism. Numerous sedimentary basins (e.g., Apache Group) that the diabase intruded were thought to form in an extensional environment since it is ordinary for basaltic rocks to be emplaced during crustal extension (Hammond, 1986; Wrucke, 1993). Bright et al. (2014) suggest all magmatism of the SWLLIP

occurred post-Greenville shortening in the southwestern U.S. and that delamination was possibly caused by right-lateral shearing during oblique convergence, provided the least resistant path for a mantle plume to rise and flatten at the base of the lithosphere. The various petrogenetic models are not mutually exclusive but could provide different contributions to SWLLIP magmatism, but it is undeniable that a mantle plume contributed to the main magmatism associated with the SWLLIP due to the high Pt and Pd concentrations and the rapid emplacement of the initial magmatism (~0.25 m.y.; Mohr et al., 2024). A single mantle plume responsible for the contemporaneous MCR and the SWLLIP magmatism is the simplest model for petrogenesis and aligns with the magmatic pulse timings of Mohr et al. (2024), which could have acceded into the upper crust due to extension caused by oblique-convergence as mentioned by Bright et al. (2014). Geochemical discrimination diagrams using immobile trace elements can help assess the petrogenesis of this magmatic event.

This study identified two different but related suites for the SWLLIP, consistent with previous research (Wrucke, 1989 and Hammond, 1991) that loosely identified mildly alkaline to tholeiitic diabase intrusions within the LIP. The more specific division of these two suites is consistent in several geochemical discrimination diagrams that provide evidence of melt compositions ranging from depleted to undepleted in chalcophile elements and exhibits characteristics of relatively higher amounts of crustal contamination (Suite 2) vs. a depleted, primitive melt (Suite 1).

When looking at the source region on a (Tb/Yb)PM vs. (La/Sm)PM, as well as the source enrichment, both suites overlap with some variation regarding the source melt's depth and composition (Fig. 7). The similarity in the source region suggests a single source for the diabase with various degrees of crustal interaction and differing degrees of melting. Suite 2 has a wide range of (Tb/Yb)PM values that indicate sourcing from both spinel and garnet lherzolite sources, with the latter likely at low degrees of partial melting (Fig 7). The five samples of Suite 2 that plot above (Tb/Yb)PM in the garnet lherzolite field are from Death Valley, CA, and Burro Mountains, NM, and are sourced from opposite ends of the SWLLIP (~800 km)(Fig. 7). Though, during emplacement of the diabase, Death Valley was closer in proximity to New Mexico. These five samples were sourced from a deeper area than the rest of the samples but had values similar to La/Sm as the rest of the SWLLIP samples. The elevated values (Tb/Yb)PM, along with the elevated Ti/V of Suite 2, can imply the melting of an enriched mantle material or a change from continental flood basalt (CFB) to oceanic-island basalt (OIB) (Jowitt et al., 2014). However, the cause for the variation of Ti/V values seen particularly in the OIB field is likely due to crustal assimilation observed in various diagrams (Fig. 6) and thin sections (deuteric reactions).

The elevated La/Sm seen in Fig. 7 is likely due to a higher degree of partial melting and/or heterogeneity of the magma or crustal contamination (La Flèche et al., 1998; Hollings et al., 2010; Wallace et al., 2015). Crustal contamination and deuteric reactions are presumed to cause the elevated La/Sm ratios rather than a

change of mantle source since samples with elevated (La/Sm)PM trend toward UCC composition (e.g., elevated Th; Fig. 13). Sample TB005 from Suite 1 shows primary mineralization replacement (e.g., saussuritization of plagioclase grains) in thin sections, which could contribute to elevated (La/Sm)PM ratios. The remaining Suite 1 sample has similar (La/Sm)PM (Fig. 7) and (Th/Yb)PM (Fig. 12), suggestive of a low degree of melting from a single homogenous source with little change in the depth of mantle melting. Most samples plot within or just outside the mantle-derived field, with Suite 1 plotting towards a slightly depleted region of the mantle (Fig. 14). The variation between the two suites in Fig. 14 suggests the degree of partial melting was the controlling factor due to only a slight change in (Th/Yb)PM ratios that would plot samples more toward EM1 compositions. If the source region were not homogeneous across the melting area, then the degree of (Nb/Yb)PM and the previously mentioned elemental quantities would be affected. Differences seen in the suites could be from the variation in the depth of melting. Alkaline compositions can be produced at depth, while tholeiitic melt typically involves significant melting in the shallower spinel stability field (Hammond, 1990). The timing of emplacement determined by Mohr et al. (2024) also correlates to the type of magmatism with tholeiitic magmatism at 1098 Ma and alkaline at 1083 Ma. The tholeiitic magmatism could represent the plume head, and the alkaline melt could be from the tail of the plume, particularly if the head detached (e.g., Bercovici & Mahoney, 1994). Hammond (1990) also noted that rifting could have allowed multiple mantle sources to rise within the region, thus having unique geochemical signatures

before crustal contamination. The crust's thickness can also correlate to increased La/Sm ratios (e.g., Turner & Langmuir, 2015), which could vary depending on the province (Fig. 1A).

In trace element diagrams, LILE (Cs, Pb, Rb, and Ba) show a wide distribution within Suite 2 (Fig. 9), likely due to heterogeneity in amounts of crustal assimilation within the suite (e.g., Mojave vs. Yavapai province; Fig. 1A). Trace element concentrations in Suite 1 plot similarly except TB012, which has a negative Sr anomaly, which is likely associated with the saussuritization of plagioclase as observed in the thin section (Humphris et al., 1998). The five Suite 2 samples from the Colorado River Area have a similar enrichment of LILE and Nb and Ta trends as Suite 1 but have positive K and Sr anomalies, similar to Suite 2, perhaps suggesting a shared plumbing system with the LIP at certain localities, particularly in the Colorado River region. Suite 2 trace element diagrams demonstrate negative Nb and Ta anomalies common to arc magmatism. Still, the case of the SWLLIP reflects accreted arc terranes that the diabase intruded and assimilated rather than arc magmatism.

Crustal contamination of the SWLLIP magmas

Assessing the crustal contamination of a given intrusion is essential in understanding the magmatic sulfide genesis. Based on the analysis of immobile elements such as HFSE coupled with LREE enrichment, we can infer the effects of crustal contamination, which could affect the distribution of the data points seen in Figure 8. Figure 6 reflects the tectonic setting, but when compared with crustal contamination diagrams (Fig. 11), the wide range of Ti/V ratios of Suite 2 in Figure 6 is thus from the higher degree of crustal rock interaction, which can be affected by the heterogeneity of the host rock types (igneous vs sedimentary) or a change from OIB to CFB magmatism.

The higher degree of crustal contamination seen in Suite 2 is demonstrated by the slightly elevated (La/Sm)PM (Fig. 8). The two highest (La/Sm)PM ratios of Suite 2 samples (Fig. 7 and 8) are some of the most crustal-contaminated samples of the study, further demonstrated by having elevated (Th/Yb)PM values (Fig. 11-13). During continental crust genesis, Th is preferably concentrated in the crust compared to other elements (Marimon et al., 2022). There are additional samples from Suite 2 that plot with elevated (Th/Yb)PM but do not show the elevated (La/Sm) PM ratios (Fig. 8 and 9). This suggests that the few samples with significantly elevated (La/Sm)PM ratios are from a higher degree of crustal contamination within certain portions of the SWLLIP rather than a change in source enrichment.

Using an (Nb/Th)_{PM} and (Th/Yb)_{PM} discrimination plots (Fig. 11), the degree of crustal contamination can be assessed since primitive mantle values have high (Nb/Th)_{PM} and low (Th/Yb)_{PM} relative to the continental crust (Jochum et al., 1989). Elevated (Th/Yb)_{PM} can also be generated from melt interaction with oceanic lithosphere or during subduction from Th being released during melting (Condie and Shearer, 2017). Suite 2 mainly clusters around LCC, which signifies that Suite 2 assimilated more crustal rock signatures than Suite 1 (Fig. 11). Two Suite 2 samples from the Burro Mountains, plot within the Suite 1 field, are the most primitive samples of Suite 2 (Fig. 11). The six Suite 2 samples that have elevated (Th/Yb)_{PM} and plot toward UCC values in Figure 11 likely incorporated country rock right before solidification thus as not to have been assimilated into the melt and possibly form a sulfur saturation based up these samples not being depleted in chalcophile elements. The four undepleted samples of Suite 2 plot among the study's lowest (Nb/Th)_{PM} and (Th/Yb)_{PM}, suggesting minor amounts of crustal contamination, which are confirmed by their undepleted chalcophile element quantities that will be discussed in the following section. Suite 2 samples, falling within the mantle-derived field or just outside clustering around the LCC values further demonstrate the crustal contamination trend with six samples containing elevated (Th/Yb)_{PM} (Fig. 13). Suite 1 shows very little crustal contamination associated with (Th/Yb)_{PM} (Fig. 13). Additional crustal material not only contributes to the magmatic signature but can affect the melt's sulfur saturation, mainly by adding crustal sulfur, which is the primary influence in making an

economical-grade magmatic sulfide deposit (Naldrett, 2010b; Keays and Lightfoot, 2010).

Magmatic sulfur saturation history of SWLLIP magmatism

Considering the magmatic system fertility, or the enrichment or depletion of chalcophile elements in magmatic sulfide systems, is essential for assessing the (Ni, Cu, PGE) mineralization potential and history of a given LIP (Jowitt et al., 2014). If a low degree of partial melting of the mantle occurs, the chalcophile elements will be retained in sulfides within the mantle (Naldrett, 2010a). Assessing the sulfide history alongside the crustal contamination diagrams can help determine which portions of the LIP are barren or enriched in chalcophile elements. Chalcophile-depleted samples, particularly from Suite 2, could indicate a large-scale sulfur saturation event at depth, which may have occurred before the emplacement and removed chalcophile elements from the silica melt and deposited elsewhere within the system. Low chalcophile tenor samples could also indicate low degrees of melt that never became sulfur-saturated, as seen in Suite 1.

Suite 1 samples cluster with similar chalcophile element ratios with no outliers (Fig 12). Suite 1 has low chalcophile tenors, suggesting that mantle sourcing, rather than a sulfur saturation event that occurred after the ascent of the melt, is likely responsible for the low chalcophile tenors. Suite 1's chalcophile quantities suggest a low degree of partial melting (<10%) that did not acquire significant chalcophile elements from the mantle (Pt ~1.11 ppb and Pd ~0.63 ppb) (Naldrett, 2010b). These chalcophile elements were retained in mantle sulfides while the chalcophile-poor sulfur-undersaturated melt was extracted and emplaced

in the upper crust. Suite 1 shows no evidence of an S saturation event with diabase intrusions, which show neither depletion nor enrichment in chalcophile elements.

The existence of two populations within Suite 2, an undepleted and depleted chalcophile element, suggests a sulfur saturation event occurred after a high-degree partial melting of a fertile source. The undepleted chalcophile samples of Suite 2 lack any evidence of crustal contamination and have elevated Pt and Pd contents (~11.14 ppb Pt and ~12.79 ppb Pd) compared to mantle values (modern convecting mantle ~6.2 ppb Pt and ~5.4 ppb Pd; Barnes et al., 2015). The undepleted chalcophile samples plotting above the average mantle values of Pd and Pt suggest an enriched source region with a high degree of melting (~25%, e.g., Keays, 1995), leaving little to no sulfide that could retain the chalcophile elements in the mantle. Platinum and Pd concentrations can reach 18 ppb from partial melting (18%) at 20 kbars (Naldrett, 2010b). The undepleted chalcophile samples suggest a high degree of mantle melting for Suite 2 samples, which is of interest since the majority of Suite 2 samples show a depletion of chalcophile elements suggesting the concentration of high tenor sulfides elsewhere in the LIP plumping system (Fig. 14). The remaining portion of this section will focus on Suite 2 due to Suite 1 showing no chalcophile element depletion (S-saturation) or crustal contamination to indicate any potential magmatic sulfide deposits.

Suite 2 has a weak positive correlation between (Cu/Zr)_{PM} and (Pd/Yb)_{PM} and against MgO (wt.%), implying that the source of the melt was responsible for the initial chalcophile concentration (Fig. 10). Suite 2 samples show a weak inverse

trend in the amount of chalcophile element depletion and crustal contamination demonstrating that the crustal contamination played a role in the removal of the sulfides from within the diabase and thus deeper intrusions of the SWLLIP could host the sulfides (Fig. 12).

The low (Cu/Zr)PM and (Pd/Yb)PM and elevated (Th/Yb)PM values seen in Suite 2 samples are likely sourced from a magma chamber that had experienced a sulfur saturation event from fractional crystallization or crustal assimilation, leaving the chalcophile-depleted diabase with low Cu and Pd values prior to emplacement. Differences in the chalcophile concentrations in contaminated samples may also be indicated by the heterogeneity of the assimilated country rock in terms of sulfur concentration (e.g., igneous vs sedimentary).

The correlation between sulfide removal and crustal contamination is seen throughout the Suite 2 samples (Fig. 12A and B). Five Suite 2 samples from a sheet in Burro Mountains, New Mexico, are depleted in (Pd/Yb)PM and (Cu/Zr)PM but only show slightly above average (Th/Yb)PM, implying limited country rock assimilation (Fig. 12). In thin section, these five samples show country rock fragmentation and brecciation (xenoliths) along with small amounts of sulfide mineralization (e.g., pyrite) seen within the brecciated rock (Fig. 3C). These sulfides likely formed during emplacement and thus did not sequester chalcophile elements from the silica melt.

Six Suite 2 samples have above-average (Th/Yb)PM and are some of the most depleted (Cu/Zr)PM and (Pd/Yb)PM rocks, except TBJA04, alluding to those

intrusions assimilated country rock containing sulfides, which allowed for sulfur saturation to occur, possibly scavenging primary chalcophile elements from the silica portion of the LIP and depositing them elsewhere in the system (Fig. 12A and B). Sample TBJA04 has an undepleted (Cu/Zr)PM compared to (Th/Yb) PM and is the sole sample from the Garnet Mountain location (Fig. 12A). The elevated (Cu/Zr)PM could be attributed to a higher-than-normal Cu content in a heterogeneous country rock that this intrusion assimilated during emplacement, or the country rock did not contain sufficient S-content to allow for sulfur saturation to occur.

The chalcophile undepleted samples of Suite 2 exhibit some of the study's lowest (Th/Yb)PM (Fig. 12), demonstrating they did not acquire continental crust that contained significant sulfur. If they had, there would be an elevated (Th/Yb)PM, but more importantly, the additional sulfide would cause the melt to become S-saturated, removing the chalcophile elements from the system and decreasing the (Cu/Zr)PM and (Pd/Yb)PM (Fig.12). These undepleted samples could represent the initial chalcophile budget of the Suite 2 magmas. It should also be noted that the range of ratios seen in Figure 12 is a component of heterogeneous crustal rocks that SWLLIP intrusions assimilated.

The interaction between the sulfide and silicate melt can be assessed by analyzing Cu/Pd vs Pd (Fig. 14). Most Suite 2 samples can be fitted to a single modeled equilibrium fractionation trend for an immiscible sulfide melt that exsolved from and equilibrated with a single batch of magma represented by the

dashed line in Figure 14 (Jowitt and Ernst, 2013). The deviation of Suite 2 away from the dashed line could be from the varying Cu content of the assimilated country rocks since Cu, Pt, and Pd all show similar patterns (Fig. 9).

The plumbing system within an LIP is vital to controlling sulfur saturation and sulfide distribution within the system (Srivastava et al., 2022). The main intrusive feature seen in the SWLLIP is sheets and sills, with an occasional feeder dike linking the sheets and sills. Sheets and sills in lower portions of the SWLLIP will thus feed higher intrusions of the LIP (Srivastava et al., 2022). If a low magma chamber within Suite 2 had a sulfur saturation event, then all the magma ascending through that chamber will exhibit a chalcophile element depletion. Multiple magma chambers at different intrusive levels along the magma ascent path would distribute various chalcophile element distributions based upon the S-saturation of those chambers.

An early sulfur saturation event at depth during the formation of the SWLLIP would promote sulfide accumulation at depth in the LIP plumbing system and thus feed upper intrusions with chalcophile-depleted melt. The undepleted samples could reflect a magma staging chamber different from the rest of Suite 2 due to their similar geographical locality within the SWLLIP, allowing undepleted samples to be placed before a sulfur saturation occurs. It is unlikely the sulfur saturation occurred during emplacement, which would allow for the scavenging of chalcophile elements from the silicate melt due to slightly elevated Pt and Pd concentrations from various locations. The chalcophile element distribution,

particularly the depleted SWLLIP intrusions, is indicative of sulfide mineralization further back in the magmatic system.

Evidence for the tectonic setting of the SWLLIP

During the Mesoproterozoic, Laurentia had various contemporaneous mafic magmatic events like the SWLLIP and Keweenawan Rift. Various modes of melting were presented in the previous sections, including a mantle plume, rifting, and various delamination models. The mafic magmatism associated with the MCR is thought to have formed in a failed rift setting associated with a mantle plume and the interaction between the plume and the lithosphere (Brzozowski et al., 2023; Cundari et al., 2021; Hollings et al., 2007a; Hart et al., 2007; Hollings et al., 2007b; Richardson, et al., 2007; Srivastava et al., 2022). A flattened plume head could span the distance between the SWLLIP and MCR (Campbell, 2007). Various authors have discussed the coeval relationship of the SWLLIP and the Keweenawan Rift due to similarities in age constraints, geochemical signatures, and paleomagnetic data (Hammond, 1986; Howard, 1991; Harlan, 1993; Wrucke, 1993; Bright et al., 2014; Mohr et al., 2024). Two plumes could have been emplaced simultaneously, causing the SWLLIP and Keweenawan Rift, but a simpler model of a single plume spreading beneath the lithosphere is thus likely due to the timing and proximity of magmatism in both regions (Bright et al., 2014; Mohr et al., 2024). Magmatism associated with a plume arrival is emplaced in a short period (<1 m.y.) and a short volume, which is what we see in both the MCR and SWLLIP.

More precise dating using U-Pb zircon from comagmatic felsic segregations within the mafic portions of the SWLLIP have confined the main pulses of

magmatism to 1098 Ma and 1083 Ma (Mohr et al., 2024). Mohr et al. (2024) demonstrated two main pulses of magmatism, with the earliest at 1098 Ma, which occurred ~2 Ma before the main magmatism of the 1096 ± 0.19 Ma Duluth Complex located within the MCR, which hosts Ni-Cu-PGE magmatic sulfides (Naldrett, 1999; Swanson-Hysell et al., 2020). It is worth noting that Van Schmus et al. (1990) obtained a U-Pb age of 1097.5 ± 3 Ma for baddeleyite from mafic magmatism associated with the MCR. Two varying plume models were presented by Mohr et al. (2024), one from the core-mantle boundary (CMB) and another from the mantle transition zone (MTZ) with plume head diameters of 1000km and 300 km, respectively (Campbell and Griffiths, 1990). Once the plume head begins to flatten at the base of the lithosphere, it can spread to a diameter of ~2000km (Campbell and Griffiths, 1990). Plate motion is thought to be ~30 cm/yr during the emplacement of the SWLLIP and MCR magmatism (Swanson-Hysell et al., 2019), which allows for the CMB plume to be emplaced at SWLLIP and then spread to the MCR zone within the ~2 Ma time frame (Mohr et al., 2024). A smaller plume sourced from the MTZ could not outpace plate motion and spread from the Southwest Laurentia to the MCR zone in the ~2 Ma time frame (Mohr et al., 2024). Van Schmus W.R. (Van Schmus, 1992) stated the magmatism along the southwestern arm of the MCR, which extends into Kansas, was synchronous with the magmatism of the Superior (Duluth Complex). This suggests the emplacement of the SWLLIP and MCR magmatism close in proximity. Mohr et al. (2024) (Fig. 3A

and B) dated Death Valley magmatism at ~1098 Ma but ~400km outside the initial area of 1098 magmatism, which is likely due to later extension.

When a plume rises and interacts with the lithosphere, it forms an intricate and usually enigmatic magmatic plumbing system within the upper crust (see Ernst et al., 2019) that can affect the magmatic sulfide potential of the melt. A common feature seen during plume emplacement is radiating dike swarms, as seen in the Proterozoic Mackenzie dike swarm (Ernst and Baragar, 1992; Ernst et al., 2019). If magmatism from a mantle plume was ejected laterally to a previously thinned portion of the lithosphere caused by extension, this could explain the lack of radiating dike swarms normally related to plume magmatism. As previously mentioned, rather than a radiating dike swarm, most SWLLIP magmatism intrudes as sheets along with normal faults at a northwest trend (Howard, 1991). Large igneous province magmatism can also contribute to the delamination of the lithosphere due to the mantle plume (Sleep, 1997; Camp and Hanan, 2008; He, 2020). The short duration of the magmatic pulse is likely due to the movement of the upper plate migration relative to the mainly stationary mantle plume, as seen within the MCR and SWLLIP (Fairchild et al., 2017). It is worth noting the end of the MCR magmatism at 1083.52 ± 0.23 Ma was associated with felsic magmatism, likely not associated with the SWLLIP magmatism (Fairchild et al., 2017)

The two magma types seen in the same LIP are not unique to the SWLLIP as seen in the Siberian Trap LIP and are explained by having two distinct source regions and plumbing systems, though in the Siberian Trap LIP case, it was

simultaneously sourced from different parts of the mantle (Arndt et al., 1998; Jowitt et al., 2014). This does not seem to be the case for the SWLLIP magmatism due to sample locations within close proximity to one another having emplacement ages differing by 14 Ma, inferring episodic magmatism (Bright et al., 2014; Hammond-Gordon et al., 2022). Geochemical data did not indicate a significant change in source composition but did show variation in depths (Fig.7).

Crustal contamination is the main process for sulfur saturation to occur within the silicate melt, which can acquire chalcophile elements from a fertile silicate melt seen in the MCR. Magmatic sulfide mineralization is located in the basaltic basal units of the Duluth Complex in the MCR (Severson et al., 2002). Suite 1 of the SWLLIP shares geochemical similarities to the dikes of Mt Mollie, Pigeon River, and ENE Sibley of the MCR magmatism, and Suite 2 samples of the SWLLIP share similar elemental ratios as the diabase Nipigon Sills of the Nipigon Embayment associated with MCR magmatism although they are not unique to the SWLLIP and Nipigon Embayment (data from Cundari et al. 2021). Diabase intrusions of the Nipigon Embayment of the MCR were emplaced before the main rifting magmatism of the MCR (Heaman et al., 2007; Hollings et al., 2007a), suggesting that the SWLLIP diabase could represent the early magmatism of failed rifting in the southwest. The Nipigon Embayment diabase exhibits crustal contamination signatures of shallow crust interaction (Brzozowski et al., 2023), similar to those seen in Suite 2 samples from this study. It should be noted that these shared elemental ratios are not unique to these LIPs. This is not indicative of

coeval magmatism, but further geochemical analysis and geophysical investigation between the MCR and SWLLIP could provide better clues to their relationship. Asthenosphere upwelling and thinning of lithosphere could provide a pathway for a mantle plume, particularly a plume at the base of a continental craton that could spread and be responsible for the SWLLIP and MCR magmatism. The magmatism of the SWLLIP does not have a radiant dike swarm present, so it is unlikely a plume head would be located at SWLLIP, further suggesting that the single plume model for MCR and SWLLIP magmatism that could have fed the region and allowed for magmatism to follow the least resistant paths. Bright et al. (2014) noted the shallowing of the lithosphere toward the southwest, as illustrated in Artemieva (2009, Fig. 5A and 12A). This would favor spreading a mantle plume in the southwest direction if the plume was centered towards the middle of the craton (Bright et al., 2014).

Spatial variation within the SWLLIP

The geochemical variation within the diabase shows a spatial variation to their locations, with the exception in the Colorado River area, being that it is the only area sampled from this study to host alkaline and tholeiitic types, suggestive of a shared plumbing system between the two suites. The differing composition between the two suites in the SWLLIP could be from the difference in the timing of magmatism. Suite 1 was confined to the Colorado River Area, associated with a 1083 Ma pulse, while the Suite 2 samples from California and Arizona are confined to areas of the earlier 1098 Ma pulse. The proximity of Death Valley and the Colorado River Area during magmatic emplacement could also explain why both suites were emplaced in the Colorado River area since both areas were closer in proximity before the Tertiary tectonic extension. The presence of both suites in the Colorado River area could also reflect the mantle-plume interaction at the base of the lithosphere (Jowitt et al., 2014). The shared relationship between the suites in the Colorado River area is seen in Figure 4, with all samples plotting within the CFB field regardless of classification. The five Suite 2 samples from the Colorado River area (TB002, TB003b, TB008b, TB010, and TB020) have lower Ti concentrations but similar V concentrations to Suite 1 and a majority of Suite 2 samples (Fig 4). Though the diabase in the Grand Canyon, as well as the Cardenas Basalt, were not analyzed in this study, similar geochemistry and textures are noted with the Salt River diabase (Wrucke, 1993) and the diabase within Apache

Group (Howard, 1991; Timmons et al., 2005). As previously mentioned, Hammond's (1990) analysis of the SWLLIP diabase distinguished two groups whose localities coincide with the eruption dates of Mohr et al. (2024).

Mohr et al. (2024) did not date any samples from New Mexico, but previous dating of felsic rocks associated with SWLLIP magmatism close to mafic samples collected for this study have age determinations of 1077 ± 4 Ma (Amato and Mack, 2012). If a plume head detaches from its conduit tail, it can cause secondary pulses of magmatism within at least 10 Ma from the initial emplacement (Bercovici and Mahoney, 1994). This secondary pulse will likely differ compositionally and reflect a mostly uncontaminated tail geochemical signature, while the plume head will have a contaminated geochemical signature due to the interaction with the lithosphere (Campbell and Griffiths, 1990). Tholeiitic magmas are generally associated with the rifting continental margin, while mildly alkaline magmatism is related to intra-plate rifting (Hammond, 1990). Alkaline basalts are thought to be from deeper, low degrees of partial melting, while tholeiitic basalts are generated from higher degrees of melting at shallower depths (Black et al., 2021).

Suite 2 samples TB002 and TB010 are sampled from the same sill but ~310 m apart. This tholeiitic sill (Suite 2) is located between sills that plot within an alkaline field (Suite 1). All Arizona locations plot within the CFB and trend toward the ARC field, which is likely due to the contamination of the melt from country rock associated with the Yavapai province, an accreted exotic terrain (Strickland et al., 2013). Most of the Death Valley samples plot just within the OIB field with the

exception of the TB021a and TB028, which plot as CFBs, likely due to crustal contamination, as seen with TB021a, which was sampled within close proximity to talc mineralization. Samples from New Mexico plot within the OIB field with three samples plotting with greater than 100 Ti/V ratio likely due to crustal contamination, which is supported by xenoliths in hand sample and thin section (Fig. 3E). The similar geographical location of the suites and the overlapping geochemical data seen in previous diagrams further suggest the shared relationship between the suites.

VII. CONCLUSIONS AND FUTURE WORK

The geochemistry of the diabase samples from the SWLLIP has been evaluated to determine the magmatic sulfide history and its potential to host Ni-Cu-PGE mineralization. Two distinct basaltic suites are found within the SWLLIP: (1) a tholeiitic suite that signifies a high degree of partial melt generated at various depths but with most samples sourced from a shallow source within the mantle, and (2) a mildly alkaline suite derived from a deeper and lower degree of partial melting of the mantle. Suite 1 was likely sourced from a more enriched portion of the mantle than Suite 2. The two suites correspond with two distinct magmatic pulses that Mohr et al. (2024) identified.

The prospectivity of Ni-Cu-PGE sulfide properties within Suite 1 alkaline rocks is prospective due to the initial low Pt and Pd concentrations, indicating a low degree of partial melting that generated chalcophile-depleted mantle-derived magmas that did not sequester significant amounts of chalcophile elements like the PGE from the mantle. In addition, the lack of crustal contamination in Suite 1 demonstrates that sulfur saturation did not occur before emplacement. Further sampling of Suite 1 localities could determine if any samples experienced high degrees of partial melting, causing higher initial PGE concentrations or crustal assimilation, particularly of S-rich sediments.

The geochemical data presents a different story for the tholeiitic Suite 2 samples, specifically due to the presence of undepleted and depleted chalcophile samples. The presence of undepleted samples demonstrates that these magmas

were sourced from a high degree of partial melting that was sulfur-undersaturated and fertile. Moreover, the presence of depleted samples that are crucially contaminated suggests a sulfur saturation event occurring prior to emplacement that depleted the magmas of chalcophile elements and deposited them elsewhere in the mafic portions of the SWLLIP plumbing system. The Suite 2 samples that are only slightly depleted in chalcophile elements and have crustal contamination signatures imply a local crustal contamination event during emplacement that did contain a significant amount of sulfide to obtain a sulfur-saturation event within the system. This study suggests that deeper tholeiitic (Suite 2) intrusions have a greater potential for Ni-Cu-PGE sulfide mineralization than their alkaline counterparts.

A model for magmatic sulfide mineralization within the SWLLIP is demonstrated in Fig. 16. Undepleted chalcophile element melt is emplaced in the upper crust while assimilating country rock. Specific intrusions within the SWLLIP, particularly Suite 2, show various degrees of crustal contamination, with a few samples showing depletion in chalcophile elements. The chalcophile element-depleted intrusions are the exhaust system of the SWLLIP and indicate that sulfide accumulation and deposition occurred further back in the system (Fig. 16)

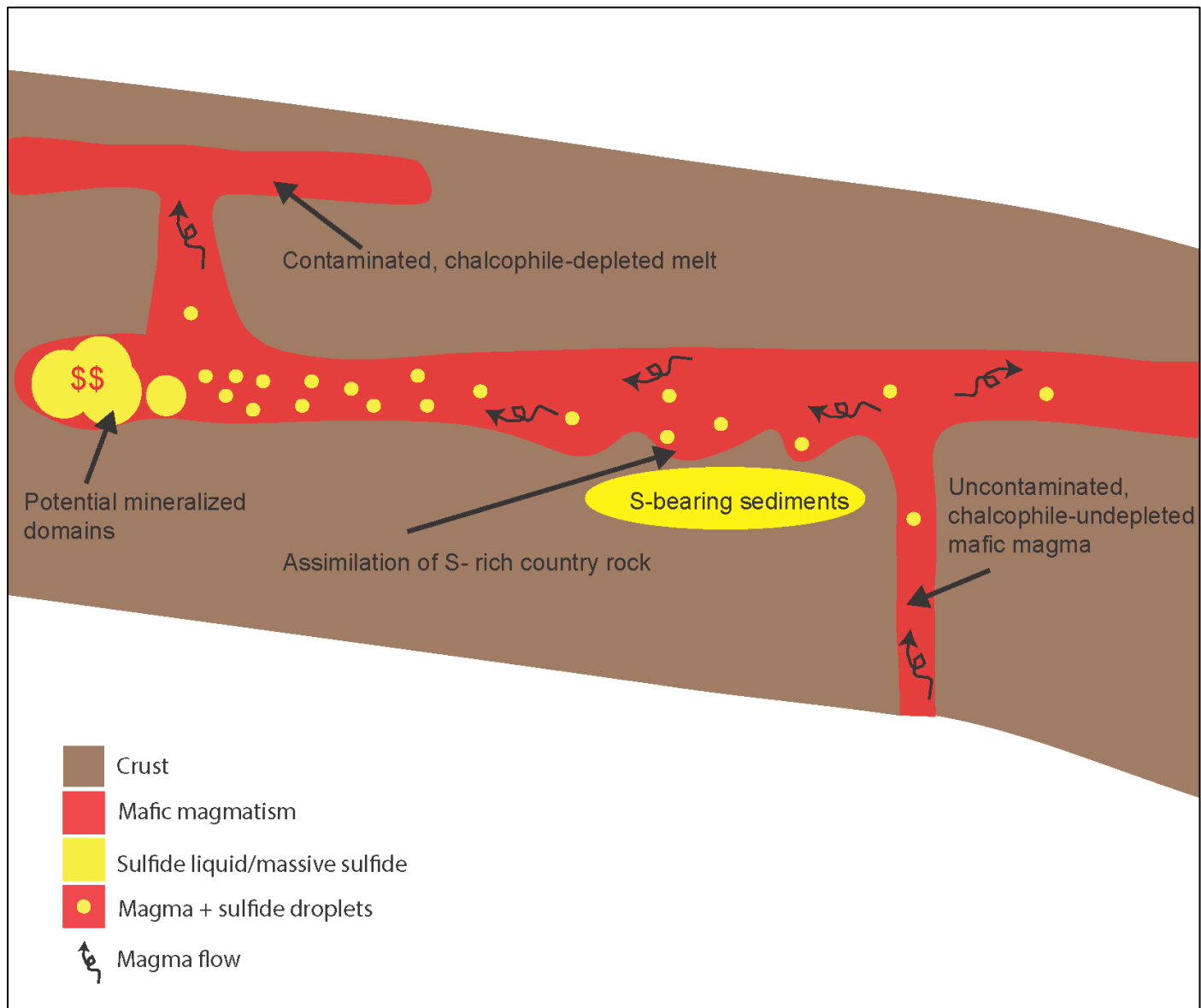


Figure 16. Magmatic sulfide model for SWLLIP

Further work would include detailed LIP seismography to understand the magmatic plumbing system and an additional analysis of tholeiitic localities. This would allow for detailed mapping of the plumbing system and could aid in determining if a single plume was responsible for the SWLLIP and MCR magmatism. Though rare, geochemical analysis of tholeiitic feeder dikes could help understand where magmatic sulfide mineralization occurred and was subsequently deposited in the LIP plumbing system. Though only minor amounts of sulfide minerals were observed in thin sections, analyzing them using a scanning electron microscope (SEM) can determine their composition, which can potentially tell you the source of the sulfides. Examining isotopic signatures would aid in better understanding the source of the SWLLIP plume and the magmatism of the Duluth Complex.

APPENDICES

Appendix A: Figure 3 and others

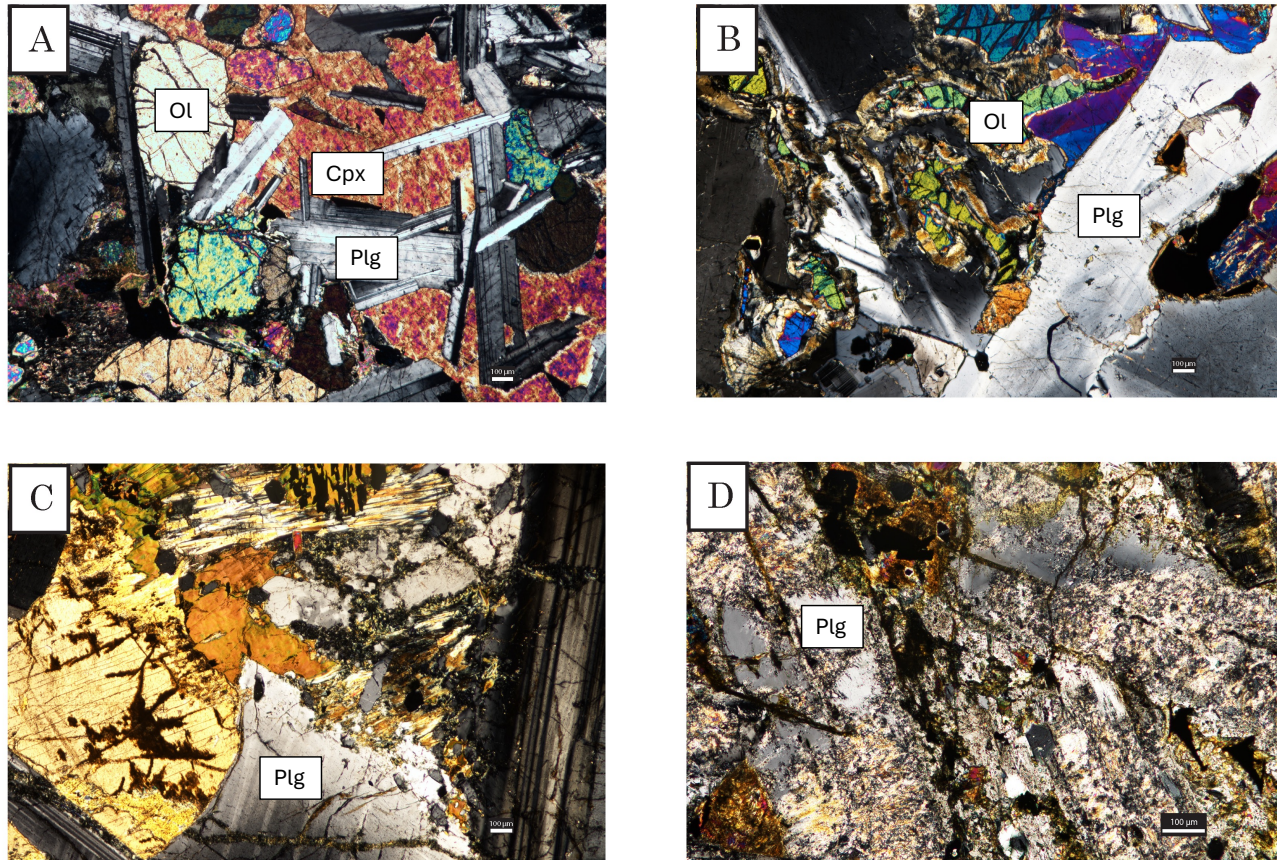


Figure 3. Photomicrographs showing representative examples of SWLLIP units. (A) TBJA05 in PPL showing subophitic texture; (B) TB008a in XPL showing alteration rims on olivine; (C) TB017 in PPL showing partial replacement of primary mineralization; (D) TB012 in PPL showing sericitization of plagioclase.

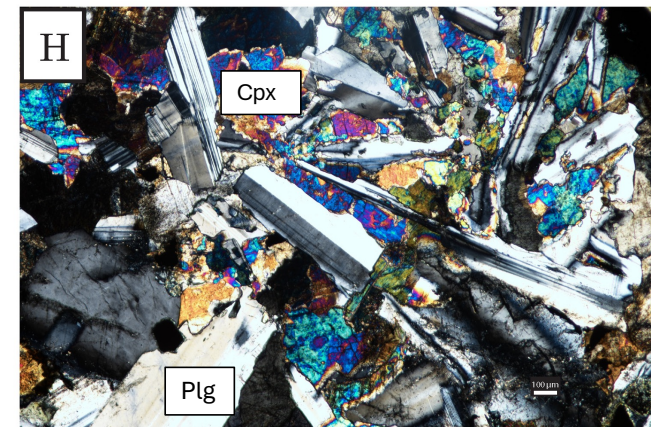
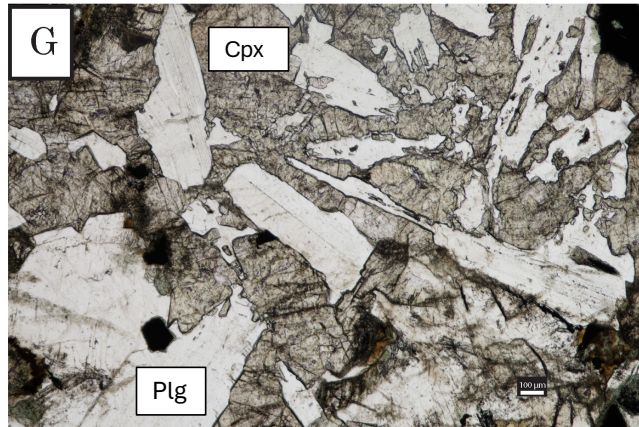
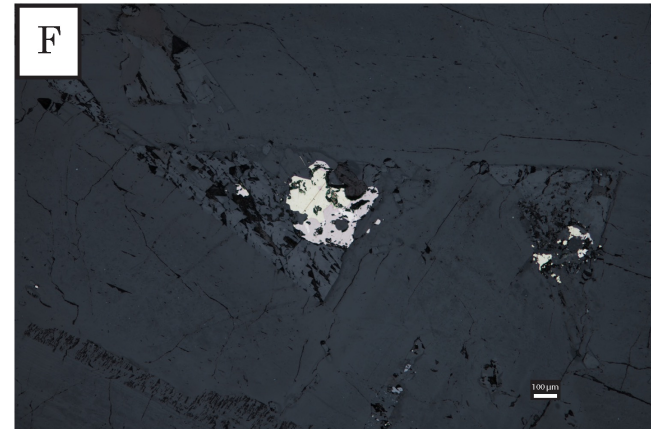
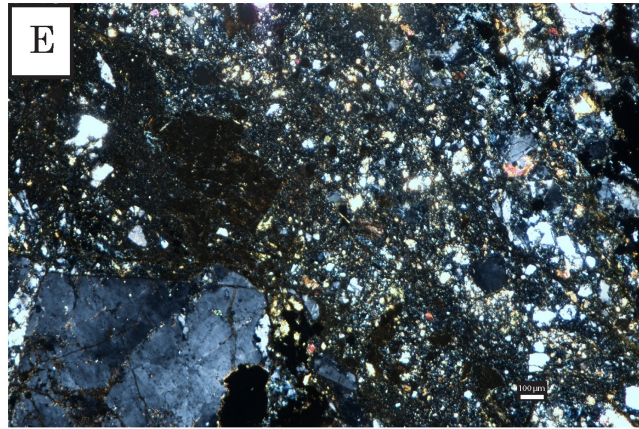


Figure 3 cont. (E) TB038M in PPL with brecciated country rock within the diabase; (F) TB008a in RFL showing multiple phases of sulfides; (G) TBJA05 in PPL showing primary mineralization seen in the undepleted samples; (H) TBJA05 in XPL. Abbreviations: PPL= plain-polarized light, XPL = cross-polarized light, RFL= reflected light, cpx = clinopyroxene, ol = olivine, plg = plagioclase.

Appendix B : Figure 8 and others

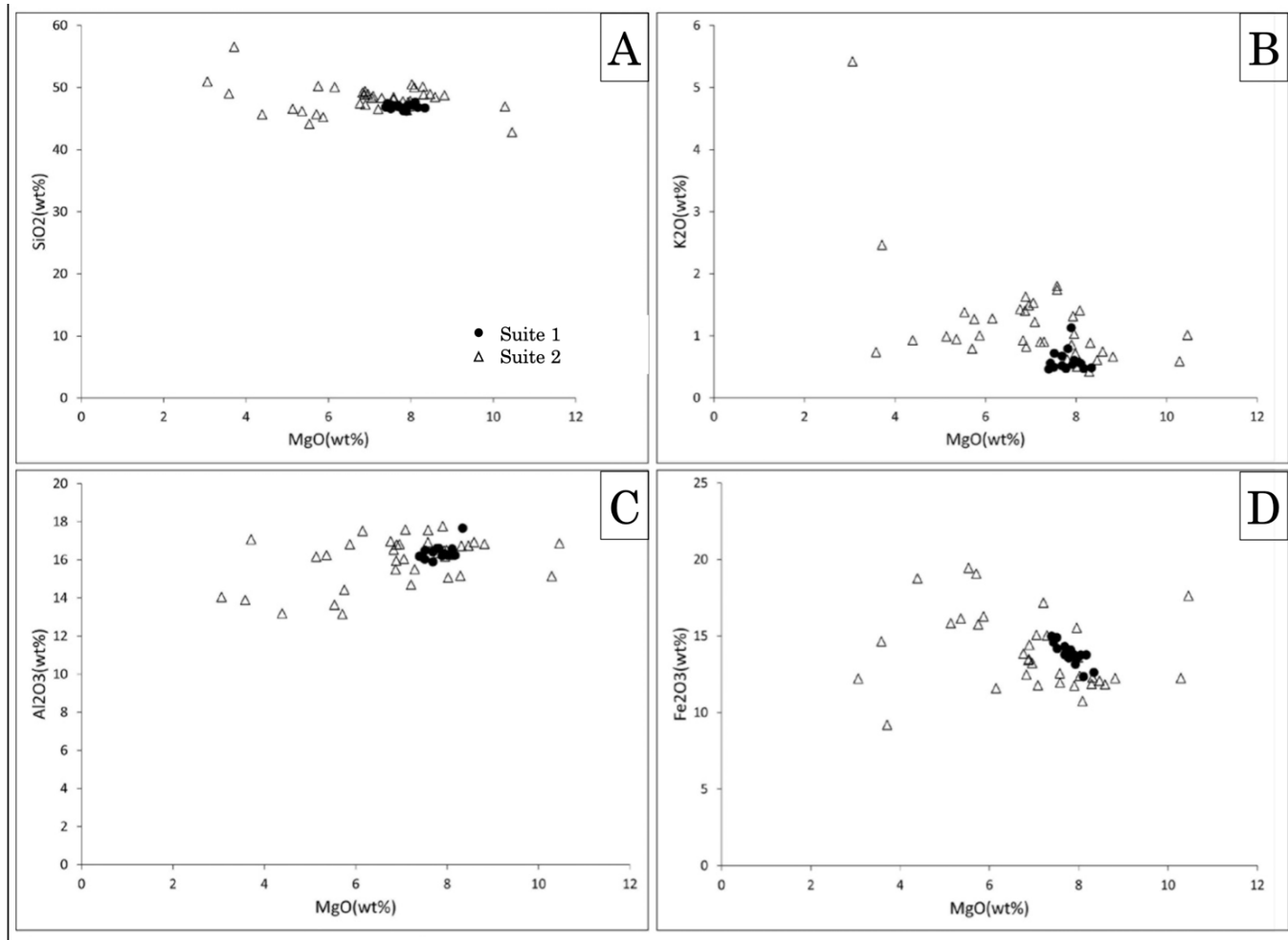


Figure 8. Plots of MgO (wt.%) vs. major element oxides (wt.%) for SWLLIP samples. Where decreasing MgO concentrations record progressive differentiation and fractional crystallization.

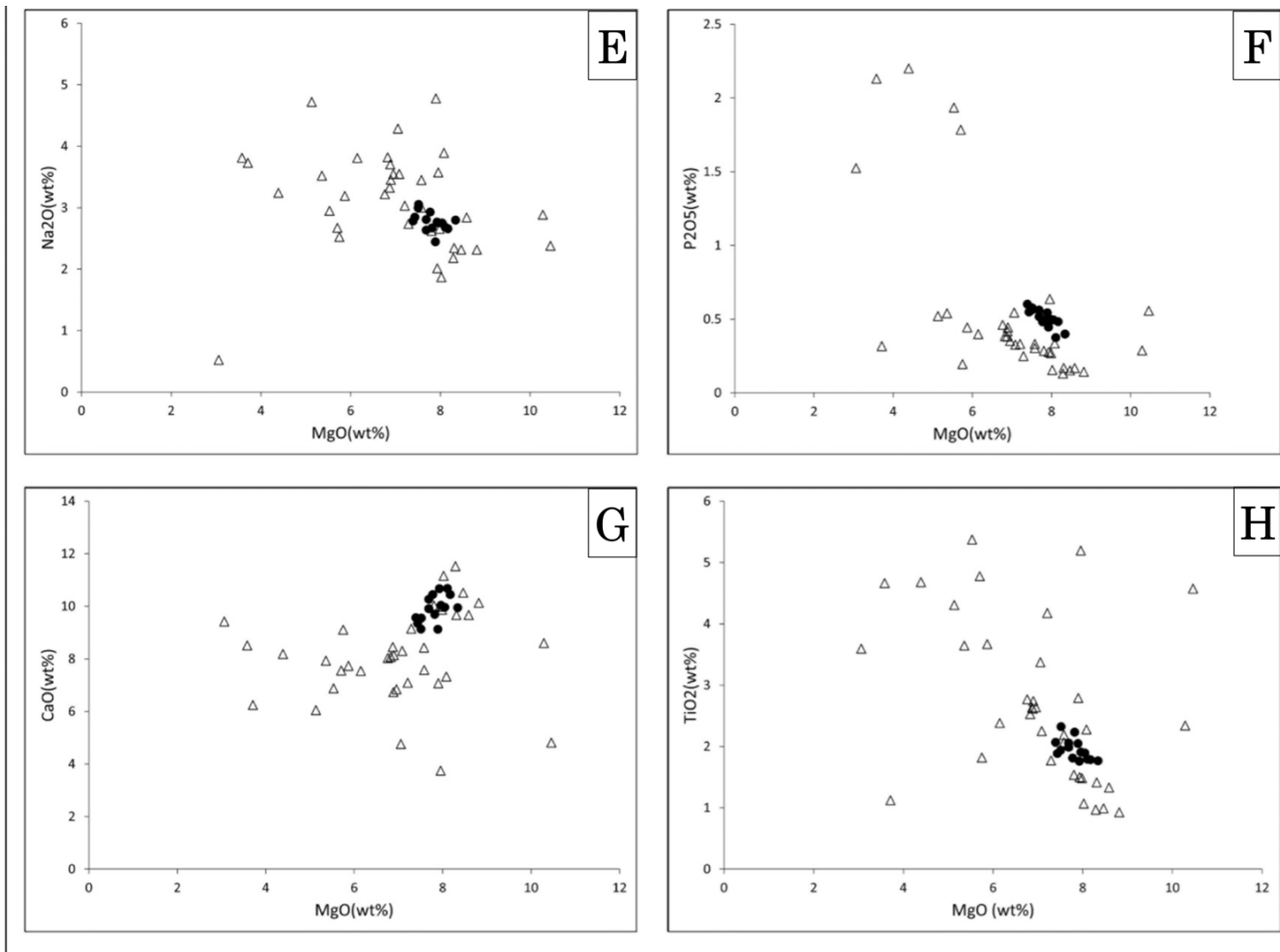


Figure 8 cont.

Appendix C: Sample locations and geochemistry

Sample		TB015	TB009	TB011	TB013	TB004	TB014	TB012	TB017	TB018
Suite		Suite 1	Suite 1	Suite 1	Suite 1	Suite 1	Suite 1	Suite 1	Suite 1	Suite 1
Location	LoD	Colorado River Basin	Colorado River Basin	Colorado River Basin	Colorado River Basin	Colorado River Basin	Colorado River Basin	Colorado River Basin	Colorado River Basin	Colorado River Basin
SiO ₂ (wt %)	0.01	46.78	46.57	47.17	46.24	47.61	46.69	46.15	46.82	47.23
TiO ₂	0.01	1.79	2.32	1.90	2.23	1.79	1.77	2.05	2.07	1.94
Al ₂ O ₃	0.01	16.24	16.50	16.27	16.60	16.57	17.67	16.21	16.19	16.03
FeO	0.01	13.77	14.19	13.75	14.09	12.35	12.62	13.78	14.97	14.90
MgO	0.01	8.17	7.52	8.04	7.82	8.11	8.34	7.89	7.39	7.51
CaO	0.01	10.45	9.55	9.96	9.70	10.68	9.95	9.13	9.56	9.14
Na ₂ O	0.01	2.66	3.05	2.75	2.67	2.69	2.80	2.45	2.78	3.00
K ₂ O	0.01	0.47	0.72	0.58	0.79	0.55	0.48	1.13	0.46	0.49
P ₂ O ₅	0.01	0.48	0.57	0.49	0.49	0.38	0.40	0.54	0.60	0.58
MnO	0.01	0.20	0.19	0.19	0.19	0.16	0.17	0.17	0.21	0.21
Cr ₂ O ₃	0.00	0.02	0.01	0.02	0.01	0.04	0.01	0.02	0.01	0.01
C	0.01	0.17	0.05	0.09	0.29	0.17	0.20	1.73	0.20	0.15
S	0.01	0.02	0.00	0.01	0.04	0.01	0.02	0.00	0.04	0.07
Total		98.96	100.13	100.26	100.31	99.20	99.38	100.50	99.24	101.00
LOI		2.78	1.62	2.02	3.54	2.26	3.36	10.55	3.28	2.83

	LoD	TB015	TB009	TB011	TB013	TB004	TB014	TB012	TB017	TB018
Ag (ppm)	0.01	0.48	0.05	0.02	0.08	0.08	0.05	0.02	0.13	0.08
Ba	0.50	233.36	398.89	205.49	1210.76	238.59	323.90	215.27	616.90	1304.39
Ce	0.10	25.65	30.33	24.72	25.68	18.34	19.56	24.90	31.74	32.58
Cs	0.01	0.13	0.10	0.15	0.21	0.10	0.12	0.29	0.14	0.12
Dy	0.05	4.29	4.59	4.51	3.96	3.30	3.30	4.34	4.59	5.03
Er	0.03	2.25	2.35	2.36	2.19	1.85	1.64	2.34	2.60	2.78
Eu	0.02	1.58	2.04	1.78	1.72	1.44	1.35	1.59	2.11	1.85
Ga	0.10	20.81	23.34	21.73	22.75	20.00	19.77	21.03	22.99	22.68
Gd	0.05	4.28	4.90	4.40	4.77	3.51	3.09	4.62	5.24	4.94
Hf	0.05	1.88	2.22	1.94	1.86	1.58	1.56	2.00	2.37	2.35
Ho	0.01	0.78	0.81	0.79	0.77	0.64	0.63	0.83	0.95	0.87
La	0.10	13.67	12.54	10.92	11.06	7.92	8.20	10.18	13.29	13.82
Lu	0.01	0.29	0.31	0.24	0.26	0.21	0.18	0.25	0.28	0.32
Nb	0.05	11.14	15.32	11.85	13.73	9.31	10.41	12.29	10.52	10.83
Nd	0.10	17.45	19.94	16.48	17.95	13.23	13.25	17.93	20.46	20.83
Pr	0.02	3.36	3.99	3.55	3.57	2.56	2.62	3.26	4.26	4.39
Rb	0.20	10.51	19.64	15.55	34.34	14.59	15.88	32.43	14.97	18.97
Sm	0.03	4.45	5.20	4.77	4.74	3.16	3.21	4.49	5.17	4.71
Sr	0.10	457.26	497.58	374.92	479.08	451.13	457.45	108.13	412.32	436.17
Ta	0.10	0.63	0.93	0.72	0.84	0.52	0.63	0.77	0.53	0.52
Tb	0.01	0.66	0.78	0.71	0.67	0.59	0.44	0.64	0.78	0.75
Th	0.05	0.94	0.90	0.88	0.84	0.59	0.59	0.79	0.94	0.96
Tm	0.01	0.30	0.30	0.30	0.28	0.21	0.22	0.29	0.35	0.33
U	0.05	0.27	0.19	0.21	0.19	0.20	0.16	0.23	0.25	0.28
V	5.00	347.94	315.62	318.27	319.39	287.55	230.30	325.39	314.25	320.68
W	0.50	0.74	0.82	0.62	0.73	1.56	0.63	3.54	0.74	0.52
Y	0.10	22.60	23.54	23.07	21.92	17.19	15.98	22.14	25.10	24.64

	LoD	TB015	TB009	TB011	TB013	TB004	TB014	TB012	TB017	TB018
Yb	0.03	1.80	2.13	1.94	1.70	1.51	1.30	1.83	2.27	1.99
Zr	1.00	70.43	83.27	75.19	76.19	53.14	56.79	77.47	88.58	91.77
As	0.10	2.31	1.54	0.93	4.28	2.40	0.95	1.44	1.37	0.93
Bi	0.01	0.02	0.01	0.02	0.03	0.04	0.02	0.02	0.02	0.02
Hg	0.01	0.06	0.03	0.03	0.11	0.10	0.03	0.04	0.04	0.02
Sb	0.05	0.06	0.05	0.00	0.09	0.08	0.00	0.00	0.05	0.00
Se	0.20	0.21	0.62	0.72	0.00	0.21	0.21	0.33	0.21	0.21
Te	0.01	0.01	0.01	0.01	0.01	0.01	0.00	0.00	0.00	0.00
Cd	0.02	0.13	0.12	0.14	0.10	0.09	0.11	0.23	0.09	0.15
Co	0.10	62.65	56.24	58.30	60.12	56.16	60.78	57.88	61.80	58.16
Cu	0.20	83.36	64.05	73.75	78.39	85.12	57.00	90.53	82.25	73.93
Mo	0.05	0.46	0.51	0.46	0.34	0.36	0.23	0.32	0.43	0.35
Ni	0.20	174.49	103.83	134.42	134.64	126.07	169.31	144.43	133.40	123.22
Pb	0.50	6.83	3.60	4.84	3.44	2.08	1.89	5.53	3.90	4.33
Sc	0.10	29.01	26.63	23.69	26.82	32.92	20.40	26.78	27.73	27.74
Zn	2.00	121.94	108.97	105.06	104.38	92.73	97.80	116.21	122.33	116.52
Au (ppb)	1.00	3.15	1.03	2.06	14.61	6.25	1.05	4.43	1.05	1.03
Pd	0.20	0.42	0.31	0.41	0.52	0.42	0.32	0.55	0.32	0.31
Pt	0.10	0.21	0.21	0.21	0.21	0.21	0.21	0.33	0.21	0.21

Sample Suite		TB007 Suite 1 Colorado River Basin	TB019 Suite 1 Colorado River Basin	TB001 Suite 1 Colorado River Basin	TB008a Suite 1 Colorado River Basin	TB003a Suite 1 Colorado River Basin	TB005 Suite 1 Colorado River Basin	TB020 Suite 2 Colorado River Basin	TB008b Suite 2 Colorado River Basin	TB003b Suite 2 Colorado River Basin
Location	LoD									
SiO ₂ (wt %)	0.01	47.15	47.43	46.91	46.70	47.13	47.13	47.78	47.67	47.86
TiO ₂	0.01	1.91	1.89	2.05	1.81	1.76	1.99	1.54	1.50	1.48
Al ₂ O ₃	0.01	16.27	16.18	15.89	16.59	16.31	16.42	16.35	16.49	16.51
FeO	0.01	13.56	14.60	14.31	13.57	13.15	13.78	13.86	13.67	13.60
MgO	0.01	7.96	7.43	7.68	7.77	7.92	7.69	7.80	7.93	7.98
CaO	0.01	10.03	9.35	10.27	10.45	10.67	9.91	10.03	9.99	9.87
Na ₂ O	0.01	2.75	2.85	2.64	2.93	2.77	2.81	2.62	2.01	2.66
K ₂ O	0.01	0.61	0.56	0.67	0.47	0.54	0.52	0.62	1.32	0.72
P ₂ O ₅	0.01	0.50	0.55	0.56	0.48	0.45	0.52	0.29	0.28	0.27
MnO	0.01	0.19	0.20	0.18	0.18	0.18	0.20	0.18	0.17	0.19
Cr ₂ O ₃	0.00	0.02	0.01	0.03	0.02	0.02	0.02	0.02	0.02	0.02
C	0.01	0.21	0.22	0.07	0.15	0.26	0.23	0.05	0.11	0.06
S	0.01	0.03	0.02	0.01	0.15	0.01	0.01	0.03	0.07	0.01
Total		99.51	99.12	100.86	98.77	100.13	100.32	100.83	100.65	98.99
LOI		2.64	3.17	1.76	0.11	2.65	2.77	1.46	2.23	1.49
Ag (ppm)	0.01	0.09	0.11	0.04	0.03	0.06	0.05	0.16	0.25	0.04
Ba	0.50	430.81	466.96	262.63	223.26	230.97	248.58	1014.79	312.35	222.15
Ce	0.10	23.57	31.41	24.63	23.04	21.44	28.90	18.75	19.93	19.41
Cs	0.01	0.09	0.16	0.44	0.13	0.25	0.25	0.15	0.49	0.11
Dy	0.05	3.89	4.66	4.20	3.91	3.67	4.60	4.14	3.96	3.88

	LoD	TB007	TB019	TB001	TB008a	TB003a	TB005	TB020	TB008b	TB003b
Er	0.03	2.11	2.59	2.19	2.02	1.92	2.63	1.92	2.12	2.40
Eu	0.02	1.40	1.91	1.69	1.52	1.46	1.82	1.59	1.48	1.52
Ga	0.10	20.76	22.87	20.03	20.07	19.47	21.65	22.11	22.91	21.07
Gd	0.05	3.83	4.70	4.72	4.25	3.79	4.45	3.89	4.15	3.76
Hf	0.05	1.77	2.42	2.03	1.68	1.78	2.13	1.92	1.96	1.64
Ho	0.01	0.75	0.91	0.85	0.81	0.76	0.85	0.76	0.78	0.73
La	0.10	10.22	13.07	10.42	9.93	8.91	16.36	7.64	8.32	8.41
Lu	0.01	0.26	0.28	0.30	0.27	0.22	0.26	0.21	0.25	0.28
Nb	0.05	11.16	10.36	11.80	10.86	10.07	12.27	5.49	6.12	5.63
Nd	0.10	15.44	20.55	16.76	15.36	14.91	18.33	13.65	13.36	13.91
Pr	0.02	3.16	4.31	3.47	3.08	3.00	3.95	2.65	2.88	2.68
Rb	0.20	12.10	16.02	17.58	7.78	11.81	11.81	18.34	67.40	15.36
Sm	0.03	3.92	5.23	4.22	4.00	3.76	4.23	3.45	3.52	3.48
Sr	0.10	420.38	408.98	379.13	398.38	402.90	437.09	381.05	401.74	360.22
Ta	0.10	0.52	0.53	0.72	0.61	0.52	0.62	0.31	0.31	0.42
Tb	0.01	0.65	0.76	0.75	0.65	0.61	0.71	0.67	0.63	0.58
Th	0.05	0.83	0.91	0.87	0.90	0.89	1.00	0.53	0.58	0.55
Tm	0.01	0.25	0.34	0.33	0.25	0.23	0.31	0.29	0.31	0.27
U	0.05	0.21	0.26	0.20	0.22	0.20	0.32	0.15	0.16	0.21
V	5.00	287.90	314.12	323.95	280.61	293.11	393.59	305.66	316.46	313.50
W	0.50	0.94	2.85	1.33	0.61	1.14	1.66	0.82	0.72	0.52
Y	0.10	19.82	25.19	21.26	19.46	20.09	23.20	19.46	21.06	19.93
Yb	0.03	1.61	2.02	1.82	1.82	1.78	1.91	1.75	1.83	1.87
Zr	1.00	68.85	88.54	75.62	67.59	64.22	85.97	68.26	69.87	66.44
As	0.10	1.36	0.74	2.45	1.13	2.07	2.07	1.43	5.34	5.19
Bi	0.01	0.03	0.01	0.07	0.01	0.02	0.02	0.03	0.04	0.07
Hg	0.01	0.05	0.02	0.09	0.05	0.02	0.04	0.09	0.09	0.20

	LoD	TB007	TB019	TB001	TB008a	TB003a	TB005	TB020	TB008b	TB003b
Sb	0.05	0.05	0.00	0.13	0.00	0.09	0.07	0.07	0.07	0.15
Se	0.20	0.21	0.21	0.31	0.51	0.00	0.00	0.20	0.51	0.73
Te	0.01	0.01	0.01	0.02	0.01	0.01	0.01	0.01	0.01	0.01
Cd	0.02	0.14	0.15	0.10	0.12	0.15	0.11	0.16	0.08	0.12
Co	0.10	58.83	61.03	57.23	59.91	58.31	62.04	55.63	58.67	60.73
Cu	0.20	94.93	82.01	92.59	91.15	116.52	182.81	101.58	92.27	34.36
Mo	0.05	0.46	0.27	0.55	0.76	0.25	0.36	0.34	0.41	0.52
Ni	0.20	167.42	137.03	125.70	154.64	176.59	152.77	137.04	148.98	148.45
Pb	0.50	4.28	4.11	5.72	1.33	1.45	1.55	3.97	5.24	5.71
Sc	0.10	30.77	28.04	29.23	27.96	31.38	27.55	27.71	28.05	20.76
Zn	2.00	93.88	120.17	100.15	101.39	96.32	103.58	108.00	103.77	104.85
Au (ppb)	1.00	4.17	1.05	6.13	2.05	3.11	2.07	3.06	11.30	10.38
Pd	0.20	0.52	0.42	0.51	0.41	0.62	0.31	0.41	0.51	0.62
Pt	0.10	0.42	0.21	0.31	0.31	0.31	0.21	0.41	0.51	0.42

Sample		TB002	TB010	TBJA05	TBJA06	TBJA02	TBJA03	TB040	TB041	TB027
Suite		Suite 2	Suite 2	Suite 2	Suite 2	Suite 2	Suite 2	Suite 2	Suite 2	Suite 2
Location	LoD	Colorado River Basin	Colorado River Basin	Salt River Canyon	Salt River Canyon	Hualapai Mountain	Hualapai Mountain	Burro Mountains	Burro Mountains	Death Valley
SiO2 (wt %)	0.01	48.44	48.88	48.76	48.95	50.50	50.13	46.21	45.25	48.07
TiO2	0.01	1.33	1.41	0.93	0.99	1.07	0.97	3.64	3.67	2.19
Al2O3	0.01	16.93	16.73	16.83	16.74	15.07	15.16	16.25	16.81	16.92
FeO	0.01	11.85	12.30	12.24	12.09	12.39	11.88	16.15	16.28	12.56
MgO	0.01	8.59	8.31	8.81	8.47	8.02	8.29	5.36	5.87	7.58
CaO	0.01	9.67	9.67	10.13	10.52	11.16	11.52	7.93	7.74	8.43
Na2O	0.01	2.84	2.34	2.32	2.32	1.87	2.18	3.52	3.19	3.00
K2O	0.01	0.74	0.89	0.66	0.61	0.50	0.42	0.94	1.00	1.74
P2O5	0.01	0.17	0.17	0.14	0.15	0.15	0.13	0.54	0.44	0.33
MnO	0.01	0.17	0.17	0.18	0.18	0.19	0.18	0.20	0.20	0.18
Cr2O3	0.00	0.03	0.03	0.02	0.02	0.07	0.05	0.00	0.00	0.02
C	0.01	0.27	0.16	0.04	0.03	0.07	0.09	0.55	0.85	0.04
S	0.01	0.02	0.01	0.03	0.03	0.07	0.08	0.19	0.18	0.01
Total		99.60	98.83	99.76	100.30	100.06	100.40	100.38	100.38	99.35
LOI		3.44	3.18	0.68	0.37	1.82	0.50	3.25	5.25	1.94
Ag (ppm)	0.01	0.03	0.01	0.05	0.04	0.05	0.06	0.03	0.05	0.02
Ba	0.50	222.29	278.72	197.90	179.52	142.95	165.26	194.19	226.27	470.30
Ce	0.10	14.26	15.63	19.18	18.81	19.85	17.18	64.28	53.50	32.50
Cs	0.01	0.09	0.16	1.17	1.38	0.58	1.46	4.82	5.36	1.23
Dy	0.05	3.06	3.71	4.77	4.76	4.12	3.48	7.60	5.31	5.13
	LoD	TB002	TB010	TBJA05	TBJA06	TBJA02	TBJA03	TB040	TB041	TB027

Er	0.03	1.91	2.05	2.90	2.74	2.34	2.02	3.61	2.89	2.74
Eu	0.02	1.01	1.25	1.14	1.02	1.18	0.97	3.06	2.59	1.73
Ga	0.10	20.34	23.33	19.28	19.52	19.44	19.20	27.31	26.43	19.10
Gd	0.05	2.94	3.42	4.38	4.45	3.88	3.53	8.81	7.23	4.71
Hf	0.05	1.70	1.81	2.72	2.87	2.15	2.07	7.92	6.46	3.32
Ho	0.01	0.60	0.69	1.01	0.92	0.82	0.77	1.31	1.06	0.97
La	0.10	5.77	6.44	8.67	8.09	8.64	7.58	24.30	20.41	13.50
Lu	0.01	0.19	0.22	0.37	0.36	0.25	0.25	0.32	0.26	0.42
Nb	0.05	3.69	3.96	3.17	3.24	4.26	3.52	14.38	12.48	7.77
Nd	0.10	9.54	11.40	12.04	13.35	13.16	12.13	42.99	37.22	20.76
Pr	0.02	2.01	2.25	2.72	2.59	2.85	2.29	9.16	7.66	4.36
Rb	0.20	25.58	33.78	17.55	14.77	34.76	10.51	42.26	97.80	51.81
Sm	0.03	2.72	3.08	3.28	3.44	3.30	2.88	9.30	8.19	4.61
Sr	0.10	347.07	385.35	201.98	194.19	263.28	248.64	814.15	784.55	404.90
Ta	0.10	0.21	0.21	0.20	0.20	0.21	0.20	0.93	0.85	0.42
Tb	0.01	0.51	0.54	0.74	0.66	0.66	0.57	1.20	1.06	0.79
Th	0.05	0.49	0.51	1.32	1.10	0.77	0.69	1.01	0.82	1.95
Tm	0.01	0.24	0.25	0.36	0.38	0.31	0.28	0.45	0.34	0.37
U	0.05	0.19	0.15	0.28	0.26	0.24	0.21	0.42	0.30	0.50
V	5.00	258.99	317.78	228.51	250.83	308.53	300.19	303.23	324.60	243.98
W	0.50	0.63	0.74	0.51	0.00	0.00	0.61	0.00	0.00	0.62
Y	0.10	16.78	18.37	25.09	24.17	19.95	16.37	31.47	25.48	27.10
Yb	0.03	1.50	1.64	2.54	2.83	2.09	1.74	2.55	2.10	2.46
Zr	1.00	62.91	67.57	107.11	104.17	88.45	76.82	335.42	283.37	130.81
As	0.10	2.52	2.53	0.61	0.61	2.16	1.62	1.97	1.16	1.35
Bi	0.01	0.04	0.03	0.03	0.03	0.02	0.02	0.03	0.02	0.02
Hg	0.01	0.21	0.07	0.02	0.02	0.04	0.07	0.05	0.06	0.02

	LoD	TB002	TB010	TBJA05	TBJA06	TBJA02	TBJA03	TB040	TB041	TB027
Sb	0.05	0.10	0.08	0.00	0.00	0.00	0.05	0.07	0.00	0.00
Se	0.20	0.21	0.32	0.31	0.30	0.31	0.40	0.00	0.21	0.21
Te	0.01	0.01	0.01	0.01	0.01	0.02	0.02	0.00	0.00	0.01
Cd	0.02	0.10	0.08	0.13	0.10	0.08	0.12	0.15	0.10	0.08
Co	0.10	55.78	58.07	61.21	55.63	53.17	52.56	54.83	58.68	51.39
Cu	0.20	56.20	81.19	115.78	111.25	132.67	133.92	27.00	26.12	57.62
Mo	0.05	0.33	0.21	0.41	0.46	0.50	0.46	1.74	1.46	0.46
Ni	0.20	189.79	175.78	241.77	216.44	169.18	172.84	39.67	54.66	145.87
Pb	0.50	3.77	6.55	4.08	2.33	2.78	2.12	5.71	9.73	5.71
Sc	0.10	27.37	28.19	22.44	32.57	37.23	37.09	23.78	21.25	21.91
Zn	2.00	93.32	95.02	94.87	86.98	88.45	84.90	124.61	132.17	120.43
Au (ppb)	1.00	15.73	3.17	4.08	5.06	7.20	5.05	3.12	2.11	12.46
Pd	0.20	0.42	0.42	12.45	12.95	10.59	15.16	0.21	2.96	1.25
Pt	0.10	0.21	0.21	9.69	9.41	11.11	14.35	0.21	0.85	0.62

Sample		TB037	TB033	TB034	TBJA01	TBJA08	TB025	TB023	TB036	TB024
Suite		Suite 2	Suite 2	Suite 2	Suite 2	Suite 2	Suite 2	Suite 2	Suite 2	Suite 2
Location	LoD	Death Valley	Death Valley	Death Valley	Hualapai Mountain	Salt River Canyon	Death Valley	Death Valley	Death Valley	Death Valley
SiO2 (wt%)	0.01	48.95	48.43	50.06	48.33	47.40	48.63	48.87	49.38	49.21
TiO2	0.01	2.64	2.07	2.28	1.77	2.77	2.25	2.63	2.62	2.53
Al2O3	0.01	16.82	17.56	16.27	15.50	16.98	17.58	15.50	15.96	16.54
FeO	0.01	13.25	11.95	10.76	15.04	13.85	11.79	13.43	13.50	12.49
MgO	0.01	6.95	7.58	8.08	7.29	6.76	7.08	6.87	6.88	6.83
CaO	0.01	6.84	7.58	7.33	9.15	8.03	8.31	8.45	6.74	8.07
Na2O	0.01	3.55	3.45	3.89	2.74	3.22	3.55	3.33	3.70	3.82
K2O	0.01	1.49	1.80	1.41	0.90	1.43	1.22	1.41	1.63	0.93
P2O5	0.01	0.35	0.30	0.34	0.25	0.46	0.33	0.38	0.42	0.38
MnO	0.01	0.21	0.20	0.17	0.22	0.17	0.18	0.20	0.24	0.21
Cr2O3	0.00	0.02	0.03	0.03	0.01	0.01	0.02	0.02	0.02	0.02
C	0.01	0.08	0.05	0.30	0.10	0.04	0.06	0.06	0.06	0.05
S	0.01	0.00	0.02	0.02	0.07	0.12	0.01	0.01	0.01	0.01
Total		99.93	98.76	99.57	100.11	100.74	98.73	100.21	98.89	99.74
LOI		2.18	2.36	3.63	2.47	2.10	2.76	2.28	2.18	2.56
Ag (ppm)	0.01	0.18	0.12	0.10	0.04	0.06	0.06	0.06	0.18	0.04
Ba	0.50	443.93	421.44	351.57	232.30	397.07	303.17	375.08	419.56	246.58
Ce	0.10	30.84	28.52	28.34	25.41	37.04	32.00	37.20	37.35	33.92
Cs	0.01	1.18	1.51	1.06	1.21	1.04	0.91	1.29	1.89	0.82
Dy	0.05	6.12	4.61	5.03	4.76	6.25	5.33	6.13	6.57	5.88
	LoD	TB037	TB033	TB034	TBJA01	TBJA08	TB025	TB023	TB036	TB024

Er	0.03	3.40	2.52	3.03	2.88	3.55	3.14	3.45	4.11	3.34
Eu	0.02	1.72	1.55	1.37	1.48	1.97	1.73	1.96	2.12	1.83
Ga	0.10	20.18	19.92	16.79	24.68	21.55	21.37	21.18	21.66	21.02
Gd	0.05	5.93	4.41	5.63	4.96	6.88	5.12	6.08	6.60	5.34
Hf	0.05	3.59	3.04	3.52	3.23	4.28	3.07	4.07	4.30	3.95
Ho	0.01	1.15	0.93	0.97	0.91	1.20	1.06	1.19	1.34	1.17
La	0.10	12.94	11.64	12.17	10.89	18.88	12.84	14.36	16.22	13.53
Lu	0.01	0.34	0.36	0.34	0.27	0.35	0.39	0.43	0.45	0.44
Nb	0.05	8.89	6.80	8.18	4.59	10.31	8.16	9.67	9.26	8.73
Nd	0.10	21.63	18.66	18.89	17.53	25.55	20.42	24.08	24.48	21.95
Pr	0.02	4.70	3.66	3.87	3.63	5.22	4.26	5.08	5.40	4.53
Rb	0.20	45.64	63.11	45.76	49.05	36.01	34.53	35.44	51.06	21.54
Sm	0.03	4.87	4.64	4.59	5.13	6.52	4.72	6.23	5.72	5.43
Sr	0.10	413.92	477.00	369.41	366.08	614.59	473.70	443.27	415.37	446.34
Ta	0.10	0.52	0.42	0.52	0.31	0.62	0.53	0.62	0.63	0.52
Tb	0.01	0.94	0.74	0.79	0.78	1.03	0.82	0.94	1.01	0.92
Th	0.05	1.84	1.52	1.62	1.50	1.17	1.53	1.86	2.06	1.83
Tm	0.01	0.47	0.36	0.38	0.35	0.48	0.39	0.45	0.50	0.48
U	0.05	0.57	0.39	0.38	0.38	0.37	0.45	0.50	0.60	0.55
V	5.00	283.54	227.49	239.28	351.56	286.26	255.80	289.32	312.84	263.23
W	0.50	0.00	1.05	0.63	0.73	1.33	0.95	0.72	1.15	0.62
Y	0.10	28.77	24.01	25.50	23.44	30.06	28.63	33.17	32.85	30.28
Yb	0.03	2.73	2.36	2.61	2.15	2.80	2.51	3.37	3.08	2.91
Zr	1.00	152.12	117.42	131.18	118.22	169.29	129.48	163.26	165.31	158.15
As	0.10	2.69	3.15	1.15	1.56	0.92	1.58	6.41	2.41	5.10
Bi	0.01	0.09	0.08	0.05	0.04	0.03	0.02	0.02	0.13	0.02
Hg	0.01	0.08	0.05	0.03	0.14	0.04	0.04	0.11	0.01	0.07
	LoD	TB037	TB033	TB034	TBJA01	TBJA08	TB025	TB023	TB036	TB024

Sb	0.05	0.08	0.08	0.05	0.05	0.00	0.00	0.07	0.10	0.05
Se	0.20	0.00	0.21	0.00	0.00	0.00	0.21	0.21	0.00	0.00
Te	0.01	0.00	0.01	0.00	0.01	0.00	0.00	0.01	0.00	0.00
Cd	0.02	0.08	0.10	0.07	0.16	0.13	0.11	0.09	0.09	0.09
Co	0.10	47.70	47.70	36.00	59.32	50.17	50.11	48.87	46.35	46.61
Cu	0.20	39.22	48.96	17.84	74.67	25.55	54.42	58.07	67.69	49.21
Mo	0.05	0.26	0.28	0.26	0.35	0.58	0.36	0.35	0.39	0.40
Ni	0.20	68.81	107.98	117.02	142.07	73.05	116.85	98.06	71.36	104.56
Pb	0.50	7.35	12.37	20.15	3.63	5.64	8.42	4.34	9.73	6.97
Sc	0.10	38.49	25.47	32.32	29.45	22.88	25.90	30.27	32.64	27.16
Zn	2.00	121.07	128.95	150.07	119.26	86.19	114.74	108.49	124.51	113.41
Au (ppb)	1.00	2.07	1.05	1.05	2.07	1.03	2.11	4.13	2.09	2.08
Pd	0.20	0.62	1.68	0.73	3.42	0.31	0.84	1.03	0.84	0.94
Pt	0.10	0.93	1.68	0.63	1.14	0.21	0.63	0.83	1.15	0.73

Sample	TB026	TBJA07	TB031	TB032	TB029	TB030	TB035	TB021a	TB028
Suite	Suite 2	Suite 2	Suite 2	Suite 2	Suite 2	Suite 2	Suite 2	Suite 2	Suite 2

Location	LoD	Death Valley	Salt River Canyon	Death Valley	Death Valley	Death Valley	Death Valley	Death Valley	Death Valley	Death Valley
SiO ₂ (wt%)	0.01	50.05	47.21	46.94	46.37	46.98	46.54	42.79	56.53	46.52
TiO ₂	0.01	2.38	2.74	2.34	2.79	5.20	4.31	4.57	1.12	4.17
Al ₂ O ₃	0.01	17.52	16.80	15.15	17.76	16.17	16.17	16.87	17.07	14.69
FeO	0.01	11.60	14.43	12.26	11.75	15.54	15.84	17.63	9.20	17.19
MgO	0.01	6.15	6.90	10.29	7.90	7.95	5.13	10.46	3.71	7.21
CaO	0.01	7.54	8.14	8.60	7.07	3.74	6.05	4.81	6.25	7.09
Na ₂ O	0.01	3.81	3.45	2.88	4.78	3.57	4.72	2.38	3.73	3.03
K ₂ O	0.01	1.28	0.82	0.59	0.86	1.03	0.99	1.02	2.46	0.90
P ₂ O ₅	0.01	0.40	0.44	0.29	0.50	0.64	0.52	0.56	0.32	0.33
MnO	0.01	0.18	0.21	0.17	0.17	0.10	0.14	0.15	0.09	0.21
Cr ₂ O ₃	0.00	0.02	0.01	0.02	0.02	0.00	0.00	0.00	0.00	0.01
C	0.01	0.04	0.04	1.58	1.01	0.45	0.98	0.33	0.24	0.13
S	0.01	0.00	0.12	0.01	0.01	0.02	0.01	0.01	0.00	0.02
Total		98.80	99.71	99.81	100.69	100.41	98.69	99.09	101.30	100.07
LOI		2.51	1.47	10.10	7.47	5.21	6.09	6.30	2.87	2.38
Ag (ppm)	0.01	0.07	0.03	0.12	0.04	0.04	0.11	0.05	0.13	0.05
Ba	0.50	455.41	321.59	110.85	406.80	267.25	341.76	407.16	742.08	383.19
Ce	0.10	35.26	37.21	31.18	50.13	66.92	67.81	62.22	56.53	45.69
Cs	0.01	0.84	1.56	0.48	0.96	1.67	0.52	0.90	1.18	2.42
Dy	0.05	5.57	6.11	5.41	7.74	7.98	7.11	8.85	4.78	5.58
	LoD	TB026	TBJA07	TB031	TB032	TB029	TB030	TB035	TB021a	TB028

Er	0.03	2.99	3.28	2.67	4.40	4.17	3.66	4.16	3.11	2.63
Eu	0.02	1.76	2.21	1.64	2.62	2.50	2.45	3.20	1.50	2.58
Ga	0.10	21.09	20.82	18.64	22.11	34.68	33.20	32.42	22.08	26.27
Gd	0.05	5.88	6.41	5.14	8.36	8.96	8.44	9.43	5.12	6.06
Hf	0.05	3.88	4.30	3.23	4.97	7.50	6.79	7.56	4.42	4.47
Ho	0.01	1.12	1.20	1.00	1.51	1.51	1.35	1.57	1.02	1.03
La	0.10	14.27	18.86	12.43	20.61	28.85	29.29	22.81	26.58	19.94
Lu	0.01	0.37	0.34	0.33	0.47	0.54	0.42	0.39	0.36	0.33
Nb	0.05	9.02	9.65	7.67	11.70	21.21	18.01	17.57	8.43	12.77
Nd	0.10	22.77	25.05	19.75	32.52	38.60	39.38	42.57	27.70	26.69
Pr	0.02	4.85	5.29	4.13	6.63	8.62	8.59	9.27	6.47	5.71
Rb	0.20	34.31	14.84	15.76	25.55	24.07	23.87	20.52	53.05	30.43
Sm	0.03	5.49	6.45	5.25	7.72	9.39	9.48	9.82	5.21	6.88
Sr	0.10	512.08	592.67	150.35	337.04	138.93	222.41	110.25	494.72	369.69
Ta	0.10	0.63	0.62	0.44	0.75	1.38	1.08	1.20	0.61	0.83
Tb	0.01	0.90	0.99	0.95	1.27	1.40	1.19	1.48	0.81	0.93
Th	0.05	2.11	1.22	1.55	2.44	6.15	5.25	5.86	6.75	3.35
Tm	0.01	0.41	0.44	0.34	0.57	0.53	0.43	0.52	0.42	0.33
U	0.05	0.50	0.36	8.43	0.77	1.96	0.84	3.58	1.63	0.62
V	5.00	218.26	273.14	248.55	258.68	449.66	447.00	447.55	243.27	587.76
W	0.50	0.52	2.27	0.67	0.54	0.85	0.87	4.58	0.92	0.52
Y	0.10	30.43	31.13	28.41	41.97	41.04	36.89	37.99	28.62	27.93
Yb	0.03	2.99	2.71	2.52	3.61	3.23	3.10	2.95	2.78	2.12
Zr	1.00	160.55	170.07	126.49	198.57	306.49	262.56	265.26	172.74	173.42
As	0.10	1.68	1.03	0.55	5.15	1.48	1.74	1.53	4.40	1.35
Bi	0.01	0.02	0.04	0.03	0.06	0.01	0.01	0.07	0.04	0.02
Hg	0.01	0.05	0.02	0.01	0.15	0.04	0.02	0.04	0.41	0.06
	LoD	TB026	TBJA07	TB031	TB032	TB029	TB030	TB035	TB021a	TB028

Sb	0.05	0.00	0.09	0.00	0.40	0.00	0.07	0.00	0.12	0.06
Se	0.20	0.00	0.21	0.33	0.21	0.21	0.00	0.22	0.00	0.00
Te	0.01	0.01	0.00	0.00	0.02	0.00	0.00	0.00	0.00	0.00
Cd	0.02	0.06	0.21	0.09	0.05	0.02	0.05	0.03	0.06	0.08
Co	0.10	48.79	53.80	46.27	45.40	72.75	60.54	55.45	17.79	73.11
Cu	0.20	59.50	41.23	217.48	73.20	7.11	12.37	49.45	7.97	10.38
Mo	0.05	0.35	0.94	0.39	0.42	0.64	0.67	0.44	0.13	1.20
Ni	0.20	98.64	78.64	63.25	58.93	55.47	82.13	74.01	7.97	173.42
Pb	0.50	10.18	8.66	3.77	12.77	7.00	7.38	3.71	12.47	7.27
Sc	0.10	18.05	24.84	28.63	27.26	30.01	28.10	28.16	22.28	23.05
Zn	2.00	100.74	141.21	126.49	132.02	148.47	134.53	216.14	90.97	144.34
Au (ppb)	1.00	1.05	1.03	2.22	4.29	2.12	1.08	3.27	5.11	2.08
Pd	0.20	3.99	0.52	0.67	1.82	0.42	0.43	0.44	0.31	0.31
Pt	0.10	1.36	0.31	0.78	1.18	0.21	0.11	0.22	0.82	0.21

Sample		TBJA04	TB038T	TB038M	TB038B	TB039M	TB039B	TB021b
Suite		Suite 2	Suite 2	Suite 2	Suite 2	Suite 2	Suite 2	Suite 2
Location	LoD	Garnet Mountain	Burro Mountains	Burro Mountains	Burro Mountains	Burro Mountains	Burro Mountains	Death Valley
SiO2 (wt %)	0.01	50.23	49.00	44.13	45.67	45.69	50.96	48.34
TiO2	0.01	1.82	4.67	5.37	4.68	4.78	3.59	3.37
Al2O3	0.01	14.42	13.90	13.65	13.19	13.15	14.05	16.04
FeO	0.01	15.75	14.65	19.45	18.77	19.08	12.22	15.07
MgO	0.01	5.75	3.58	5.53	4.39	5.70	3.06	7.06
CaO	0.01	9.11	8.51	6.88	8.19	7.56	9.42	4.76
Na2O	0.01	2.53	3.81	2.95	3.24	2.67	0.52	4.29
K2O	0.01	1.27	0.73	1.38	0.93	0.79	5.42	1.53
P2O5	0.01	0.19	2.13	1.93	2.20	1.78	1.52	0.55
MnO	0.01	0.21	0.13	0.27	0.25	0.30	0.13	0.24
Cr2O3	0.00	0.01	0.00	0.00	0.00	0.00	0.00	0.01
C	0.01	0.05	0.05	0.07	0.08	0.06	0.03	0.05
S	0.01	0.08	0.13	0.17	0.08	0.19	0.03	0.01
Total		100.08	99.76	100.21	99.99	101.43	100.16	101.52
LOI		1.00	4.76	3.01	2.57	2.93	3.41	2.97
Ag (ppm)	0.01	0.04	0.06	0.05	0.05	0.02	0.04	0.14
Ba	0.50	292.59	596.49	527.01	516.13	476.53	965.98	426.81
Ce	0.10	43.58	122.49	112.93	134.51	112.94	102.45	44.64
Cs	0.01	7.84	0.98	1.93	1.90	1.43	1.27	4.51
Dy	0.05	6.64	17.58	15.48	18.09	15.63	12.84	6.84
	LoD	TBJA04	TB038T	TB038M	TB038B	TB039M	TB039B	TB021b

Er	0.03	4.02	11.02	8.58	10.19	8.70	6.91	3.67
Eu	0.02	1.74	4.60	4.41	4.89	4.19	4.28	2.36
Ga	0.10	24.14	25.99	23.11	25.44	24.65	23.39	21.49
Gd	0.05	6.71	19.55	17.72	21.17	17.59	14.62	7.32
Hf	0.05	4.30	12.25	10.56	12.41	10.68	7.74	4.96
Ho	0.01	1.35	3.72	2.96	3.69	2.99	2.56	1.37
La	0.10	20.15	57.09	51.13	57.45	48.68	43.65	17.28
Lu	0.01	0.47	1.30	0.89	1.09	0.94	0.80	0.39
Nb	0.05	6.91	23.43	19.24	22.00	19.03	14.41	12.08
Nd	0.10	25.27	81.59	75.18	87.69	76.33	65.79	30.03
Pr	0.02	5.43	17.63	15.84	18.25	15.88	14.36	6.18
Rb	0.20	74.27	42.82	128.61	72.05	75.61	288.23	38.88
Sm	0.03	5.69	19.55	16.73	19.08	17.74	15.40	7.22
Sr	0.10	244.51	189.60	243.64	206.97	220.73	386.39	432.98
Ta	0.10	0.41	1.49	1.25	1.36	1.13	0.94	0.82
Tb	0.01	0.99	2.94	2.68	3.13	2.65	2.19	1.09
Th	0.05	5.18	8.01	5.43	6.66	5.25	4.33	1.34
Tm	0.01	0.49	1.41	1.02	1.29	1.10	0.91	0.49
U	0.05	0.86	3.59	1.05	1.48	1.09	1.79	0.45
V	5.00	369.32	268.42	308.47	273.18	328.00	230.79	290.03
W	0.50	0.51	1.81	1.05	3.55	0.83	1.46	0.62
Y	0.10	33.25	101.51	79.78	93.42	78.70	64.96	36.72
Yb	0.03	3.15	9.09	6.77	7.71	6.82	5.98	3.37
Zr	1.00	161.64	538.97	447.54	528.64	455.90	349.84	200.55
As	0.10	0.61	0.96	0.52	0.94	0.72	3.45	5.86
Bi	0.01	0.03	0.87	0.06	0.11	0.04	0.37	0.02
Hg	0.01	0.01	0.05	0.01	0.08	0.04	0.02	0.29
	LoD	TBJA04	TB038T	TB038M	TB038B	TB039M	TB039B	TB021b

Sb	0.05	0.05	0.10	0.05	0.08	0.00	0.06	0.17
Se	0.20	0.20	0.32	0.00	0.21	0.21	0.31	0.21
Te	0.01	0.00	0.01	0.00	0.00	0.00	0.02	0.00
Cd	0.02	0.11	0.10	0.29	0.13	0.06	0.00	0.09
Co	0.10	55.35	57.84	61.38	22.42	53.53	90.85	48.03
Cu	0.20	139.65	8.41	24.89	82.79	21.25	21.93	12.24
Mo	0.05	0.70	1.76	1.34	1.78	1.20	0.86	0.48
Ni	0.20	77.04	15.55	30.43	13.87	59.10	25.27	46.07
Pb	0.50	6.85	6.28	16.21	12.72	5.05	4.07	12.03
Sc	0.10	37.55	35.15	31.68	35.45	26.82	28.09	25.40
Zn	2.00	130.95	146.99	191.35	173.09	188.76	66.84	298.25
Au (ppb)	1.00	1.02	1.07	1.05	2.09	1.03	1.04	5.14
Pd	0.20	1.02	0.21	0.21	0.42	0.41	0.42	0.31
Pt	0.10	0.92	0.21	0.10	0.21	0.21	0.21	0.21

Abbreviations: - = not detected or value given, LoD = lower limit of detection, ppm = parts per million, ppb = parts per billion, SD = standard deviation

Appendix D: Standard geochemistry and certificate values.

SAMPLE	TB006	TB042	Certificate			TB022	TB043	Certificate	
			LoD	OREAS 684	SD			OREAS 24d	SD
SiO2	46.90	47.20	0.01	47.96	0.81	45.60	46.90	47.07	-
Al2O3	11.15	11.25	0.01	11.37	0.12	15.35	15.10	15.22	0.21
Fe2O3	11.15	11.35	0.01	11.44	0.26	11.95	11.85	11.69	0.38
CaO	6.17	6.32	0.01	6.38	0.20	8.29	8.24	8.30	0.25
MgO	17.85	17.80	0.01	17.99	0.35	8.05	7.91	7.79	0.16
Na2O	0.88	0.90	0.01	0.91	0.03	3.33	3.16	3.14	0.11
K2O	0.17	0.18	0.01	0.23	0.02	2.06	2.03	2.05	0.06
Cr2O3	1.91	2.00	0.00	1.99	0.05	0.03	0.03	0.03	-
TiO2	0.23	0.24	0.01	0.24	0.01	2.13	2.06	2.11	0.05
MnO	0.16	0.17	0.01	0.17	0.00	0.16	0.16	0.16	0.01
P2O5	0.03	0.04	0.01	0.03	0.00	0.61	0.58	0.59	0.02
C	0.13	0.13	0.01	-	-	0.03	0.04	-	-
S	0.42	0.45	0.01	-	-	0.04	0.05	-	-
Total	98.15	99.02		-	-	100.34	100.75	-	-
LOI	1.52	1.54		-	-	2.63	2.58	1.55	-
Ba (ppm)	74.00	74.40	0.50	70.62	3.65	560.00	562.00	536.16	16.00
Ce	6.90	7.20	0.10	6.62	0.28	61.40	60.40	59.40	1.47
Cr	>10000	>10000	5.00	13600.00	520.00	231.00	203.00	147.09	21.07
Cs	0.25	0.25	0.01	0.26	0.02	1.20	1.18	1.18	0.07
Dy	0.83	0.85	0.05	0.78	0.05	4.24	4.39	-	-
Er	0.58	0.57	0.03	0.55	0.03	1.98	2.18	-	-
Eu	0.27	0.23	0.02	0.24	0.04	1.88	1.91	-	-
Ga	12.50	12.30	0.10	11.39	0.37	25.00	23.10	22.06	0.84
Gd	0.74	0.78	0.05	0.70	0.09	5.23	5.95	-	-
Ge	1.40	1.40	0.50	-	-	1.60	1.40	-	-
Hf	0.51	0.57	0.05	0.37	0.04	4.81	4.92	4.70	0.33
Ho	0.15	0.19	0.01	0.18	0.01	0.80	0.75	-	-
La	3.40	3.70	0.10	3.33	0.17	29.10	30.50	29.12	2.01
Lu	0.07	0.09	0.01	0.09	0.01	0.27	0.18	0.23	0.03

	TB006	TB042	LoD OREAS 684	SD	TB022	TB043	OREAS 24d	SD	
Nb	1.30	1.36	0.05	1.19	0.17	45.80	46.10	44.57	4.14
Nd	3.70	3.40	0.10	3.14	0.13	29.90	29.30	-	-
Pr	0.70	0.86	0.02	0.81	0.04	7.37	7.12	-	-
Rb	5.30	4.80	0.20	5.67	0.31	38.10	37.60	37.23	4.23
Sm	0.73	0.73	0.03	0.69	0.03	6.88	6.61	-	-
Sn	0.60	0.50	0.50	0.66	0.12	2.00	2.30	1.89	0.09
Sr	168.00	157.00	0.10	160.53	8.12	806.00	766.00	748.42	37.23
Ta	0.10	0.10	0.10	-	-	3.10	3.10	3.01	0.24
Tb	0.13	0.12	0.01	0.12	0.01	0.79	0.83	0.79	0.04
Th	0.73	0.85	0.05	0.77	0.07	3.67	4.03	3.78	0.33
Tm	0.08	0.08	0.01	0.08	0.01	0.25	0.26	-	-
U	0.24	0.22	0.05	0.22	0.03	1.45	1.63	1.40	0.09
V	185.00	186.00	5.00	174.06	9.78	232.00	228.00	201.37	6.70
W	1.10	1.00	0.50	0.56	0.06	0.60	<0.5	-	-
Y	4.80	4.50	0.10	4.39	0.28	21.80	20.10	20.43	0.90
Yb	0.61	0.62	0.03	0.56	0.04	1.64	1.55	-	-
Zr	20.00	20.00	1.00	12.41	1.37	216.00	220.00	204.92	5.69
As	0.70	0.70	0.10	-	-	1.20	1.20	-	-
Bi	0.31	0.34	0.01	0.36	0.02	0.02	0.02	0.03	0.01
Hg	0.01	0.01	0.01	-	-	<0.005	<0.005	-	-
In	0.01	0.01	0.01	0.03	0.01	0.02	0.02	0.07	0.01
Re	0.00	0.00	0.00	-	-	0.00	<0.001	-	-
Sb	0.06	0.08	0.05	-	-	0.06	0.06	-	-
Se	1.60	2.00	0.20	-	-	0.30	<0.2	-	-
Te	0.62	0.65	0.01	0.69	0.11	<0.01	<0.01	-	-
Tl	0.05	0.05	0.02	0.06	0.01	0.09	0.09	0.12	0.02
Ag	0.36	0.38	0.01	-	-	0.04	0.06	-	-
Cd	0.13	0.13	0.02	0.12	0.01	0.12	0.12	0.12	0.02
Co	118.50	112.50	0.10	111.57	5.78	45.70	42.60	44.21	2.42
Cu	1050.00	1020.00	0.20	978.07	25.63	42.70	41.60	43.19	2.29
Li	4.40	4.20	0.20	3.95	0.30	11.40	11.00	10.76	0.65

	TB006	TB042	LoD	OREAS 684	SD	TB022	TB043	OREAS 24d	SD
Mo	1.22	1.27	0.05	1.19	0.15	4.27	4.27	4.46	0.35
Ni	2380.00	2310.00	0.20	2168.34	124.49	148.00	141.00	136.55	6.90
Pb	10.40	9.70	0.50	11.12	0.86	3.30	3.20	3.56	0.44
Sc	19.50	20.30	0.10	19.09	1.35	18.10	21.60	19.96	1.11
Zn	109.00	105.00	2.00	98.59	8.66	113.00	109.00	103.64	6.74
Au (ppb)	151.00	255.00	1.00	-	-	1.00	1.00	-	-
Pt (ppb)	>1000	>1000	0.10	-	-	0.70	0.60	-	-
Pd (ppb)	>1000	>1000	0.20	-	-	1.20	1.20	-	-
Au (ppm)	0.26	0.26	0.01	0.24	0.01	-	-	-	-
Pt (ppm)	3.87	4.03	0.01	3.80	0.19	-	-	-	-
Pd (ppm)	1.76	1.75	0.01	1.74	0.05	-	-	-	-

SAMPLE	LoD	Certificate				Certificate			
		TB044	TB045	OREAS 682	SD	TB046	GSP-2	SD	
SiO2	0.01	50.20	50.60	51.26	0.52	67.60	66.60	0.80	
Al2O3	0.01	16.70	16.75	16.76	0.17	15.00	14.90	0.20	
Fe2O3	0.01	9.87	9.88	9.92	0.22	4.90	4.90	0.16	
CaO	0.01	9.14	9.20	9.26	0.17	2.11	2.10	0.06	
MgO	0.01	8.20	8.27	8.21	0.16	0.97	0.96	0.03	
Na2O	0.01	2.13	2.14	2.16	0.04	2.82	2.78	0.09	
K2O	0.01	1.38	1.40	1.42	0.05	5.39	5.38	0.14	
Cr2O3	0.00	0.53	0.54	0.54	0.02	0.00	-	-	
TiO2	0.01	0.85	0.85	0.85	0.01	0.67	0.66	0.02	
MnO	0.01	0.15	0.15	0.15	0.00	0.04	-	-	
P2O5	0.01	0.29	0.28	0.28	0.01	0.29	0.29	0.02	
C	0.01	0.07	0.07	-	-	0.08	-	-	
S	0.01	0.11	0.12	-	-	0.05	-	-	
Total		99.94	100.65	-	-	100.91	-	-	
LOI		0.40	0.50	-	-	0.94	-	-	
Ba (ppm)	0.50	382.00	407.00	376.00	22.00	1385.00	1340.00	44.00	
Ce	0.10	36.10	36.60	35.87	1.59	467.00	410.00	30.00	
Cr	5.00	3720.00	3860.00	3701.00	157.00	23.00	20.00	6.00	
Cs	0.01	3.50	3.50	3.57	0.22	1.19	1.20	0.10	
Dy	0.05	3.00	3.12	2.92	0.22	6.57	6.10	-	
Er	0.03	2.04	1.78	1.62	0.15	2.65	2.20	-	
Eu	0.02	1.26	1.28	1.25	0.10	2.51	2.30	0.10	
Ga	0.10	19.30	19.30	18.30	1.04	24.40	22.00	2.00	
Gd	0.05	3.73	3.83	3.66	0.41	13.10	12.00	2.00	
Ge	0.50	1.50	1.60	-	-	1.80	-	-	
Hf	0.05	2.24	2.10	1.55	0.19	16.25	14.00	1.00	
Ho	0.01	0.65	0.61	0.55	0.06	1.10	1.00	0.10	
La	0.10	18.10	17.90	17.30	1.09	193.50	180.00	12.00	
Lu	0.01	0.21	0.20	0.22	0.03	0.20	0.23	0.03	

	LoD	TB044	TB045	OREAS 682	SD	TB046	GSP-2	SD
Nb	0.05	5.51	5.30	5.16	0.97	25.80	27.00	2.00
Nd	0.10	19.20	19.40	19.40	0.76	217.00	200.00	12.00
Pr	0.02	4.37	4.61	4.66	0.14	56.50	51.00	5.00
Rb	0.20	70.80	71.70	72.00	2.30	257.00	245.00	7.00
Sm	0.03	4.06	4.41	4.03	0.14	27.40	27.00	1.00
Sn	0.50	1.90	1.80	1.63	0.12	8.00	-	-
Sr	0.10	465.00	476.00	455.00	19.93	249.00	240.00	10.00
Ta	0.10	0.40	0.40	0.38	0.03	0.90	-	-
Tb	0.01	0.53	0.52	0.50	0.06	1.43	-	-
Th	0.05	6.44	5.69	5.52	0.32	117.50	105.00	8.00
Tm	0.01	0.24	0.20	0.23	0.02	0.30	0.29	0.02
U	0.05	1.26	1.24	1.36	0.15	2.59	2.40	0.19
V	5.00	251.00	239.00	231.00	10.00	62.00	52.00	4.00
W	0.50	1.20	1.20	1.08	0.10	0.80	-	-
Y	0.10	16.10	15.60	15.40	0.44	26.10	28.00	2.00
Yb	0.03	1.64	1.66	1.51	0.07	1.89	1.60	0.20
Zr	1.00	75.00	82.00	51.54	4.15	631.00	550.00	30.00
As	0.10	0.60	0.80	-	-	0.60	-	-
Bi	0.01	0.08	0.09	0.10	0.01	0.03	-	-
Hg	0.01	0.01	<0.005	-	-	0.02	-	-
In	0.01	0.01	0.01	0.04	0.01	0.03	-	-
Re	0.00	0.00	0.00	-	-	0.00	-	-
Sb	0.05	0.10	0.10	0.20	0.05	0.30	-	-
Se	0.20	0.50	0.50	-	-	<0.2	-	-
Te	0.01	0.15	0.15	-	-	0.03	-	-
Tl	0.02	0.06	0.06	0.15	0.01	0.59	-	-
Ag	0.01	0.12	0.12	-	-	0.10	-	-
Cd	0.02	0.05	0.06	-	-	0.08	-	-
Co	0.10	47.90	50.10	52.00	3.80	7.10	7.30	0.80
Cu	0.20	256.00	260.00	261.00	15.00	44.00	43.00	4.00
Li	0.20	11.30	12.10	12.80	1.18	37.80	36.00	1.00

	LoD	TB044	TB045	OREAS 682	SD	TB046	GSP-2	SD
Mo	0.05	1.42	1.46	1.45	0.19	2.62	2.10	0.60
Ni	0.20	571.00	584.00	572.00	30.15	18.20	17.00	2.00
Pb	0.50	7.80	8.20	30.00	0.95	40.60	42.00	3.00
Sc	0.10	23.80	25.80	21.40	2.30	6.20	6.30	0.70
Zn	2.00	83.00	85.00	90.00	21.00	122.00	120.00	10.00
Au (ppb)	1.00	72.00	76.00	71.60	3.30	19.00	-	-
Pt (ppb)	0.10	819.00	838.00	820.00	52.00	2.10	-	-
Pd (ppb)	0.20	421.00	436.00	440.00	26.47	4.10	-	-
Au (ppm)	0.01	-	-	-	-	-	-	-
Pt (ppm)	0.01	-	-	-	-	-	-	-
Pd (ppm)	0.01	-	-	-	-	-	-	-

Abbreviations: - = not detected or value given, LoD = lower limit of detection, ppm = parts per million, ppb = parts per billion, SD = standard deviation

REFERENCES

- Adams, D.C., Ouimette, M.A., and Moreno, F., 2022, Middle-late Proterozoic extension in the Carlsbad region of southeastern New Mexico and west Texas, *in* New Mexico Geological Society, p. 137–144, doi:10.56577/ffc-44.137.
- Amato, J.M., Boullion, A.O., Serna, A.M., Sanders, A.E., Farmer, G.L., Gehrels, G.E., and Wooden, J.L., 2008, Evolution of the Mazatzal province and the timing of the Mazatzal orogeny: Insights from U-Pb geochronology and geochemistry of igneous and metasedimentary rocks in southern New Mexico: *Bulletin of the Geological Society of America*, v. 120, p. 328–346, doi:10.1130/B26200.1.
- Amato, J.M., Heizler, M.T., Boullion, A.O., Sanders, A.E., Toro, J., McLemore, V.T., and Andronicos, C.L., 2011, Syntectonic 1.46 Ga magmatism and rapid cooling of a gneiss dome in the southern Mazatzal province: Burro Mountains, New Mexico: *Bulletin of the Geological Society of America*, v. 123, p. 1720–1744, doi:10.1130/B30337.1.
- Amato, J.M., and Mack, G.H., 2012, Detrital zircon geochronology from the Cambrian-Ordovician Bliss Sandstone, New Mexico: Evidence for contrasting Grenville-age and Cambrian sources on opposite sides of the Transcontinental Arch: *Bulletin of the Geological Society of America*, v. 124, p. 1826–1840, doi:10.1130/B30657.1.
- Arndt, N., Chauvel, C., Czamanske, G., and Fedorenko, V., 1998, Two mantle sources, two plumbing systems: tholeiitic and alkaline magmatism of the Maymecha River basin, Siberian flood volcanic province: *Contrib Mineral Petrol*, p. 297–313.
- Ball, P.W., White, N.J., Maclennan, J., and Stephenson, S.N., 2021, Global influence of mantle temperature and plate thickness on intraplate volcanism: *Nature Communications*, v. 12, doi:10.1038/s41467-021-22323-9.
- Barnes, S.J., 2023, Lithogeochemistry in exploration for intrusion-hosted magmatic Ni-Cu-Co deposits: *Geochemistry: Exploration, Environment, Analysis*, v. 23, doi:10.6084/m9.figshare.c.6267664.
- Barnes, S.-J., Couttn, J.-F., Sawyer, E.W., and Bouchaib, C., 1993, Nickel-Copper Occurrences in the Belleterre-Angliers Belt of the Pontiac Subprovince and the Use of Cu-Pd Ratios in Interpreting Platinum-Group Element Distributions: <http://pubs.geoscienceworld.org/segweb/economicgeology/article-pdf/88/6/1402/3491365/1402.pdf>.
- Barnes, S.J., Holwell, D.A., and Le Vaillant, M., 2017, Magmatic sulfide ore deposits: *Elements*, v. 13, p. 89–95, doi:10.2113/gselements.13.2.89.
- Barnes, S.-J., and Lightfoot, P.C., 2005, Formation of Magmatic Nickel Sulfide Deposits and Processes Affecting Their Copper and Platinum Group Element Contents: *Economic Geology*, v. 100, p. 179–213.

- Barnes, S.-J., and Maier, W.D., 1999, The fractionation of Ni, Cu and the noble metals in silicate and sulphide liquids, <https://api.semanticscholar.org/CorpusID:85509253>.
- Barnes, S.J., Mungall, J.E., and Maier, W.D., 2015, Platinum group elements in mantle melts and mantle samples: *Lithos*, v. 232, p. 395–417, doi:10.1016/j.lithos.2015.07.007.
- Bercovici, D., and Mahoney, J., 1994, Double Flood Basalts and Plume Head Separation at the 660-Kilometer Discontinuity: *Science*, v. 266, p. 1367–1369.
- Blacet, P.M., 1975, Preliminary geologic map of the Garnet Mountain Quadrangle, Mohave County, Arizona: doi:10.3133/ofr7593.
- Black, B.A., Karlstrom, L., and Mather, T.A., 2021, The life cycle of large igneous provinces: *Nature Reviews Earth and Environment*, v. 2, p. 840–857, doi:10.1038/s43017-021-00221-4.
- Bright, R.M., 2012, High-precision geochronology and geochemical analysis of ~1.1 Ga diabase intrusions in the southwestern United States: New Mexico State University.
- Bright, R.M., Amato, J.M., Denyszyn, S.W., and Ernst, R.E., 2014, U-Pb geochronology of 1.1 Ga diabase in the southwestern United States: Testing models for the origin of a post-Grenville large igneous province: *Lithosphere*, v. 6, p. 135–156, doi:10.1130/L335.1.
- Bryan, S.E., and Ernst, R.E., 2008, Revised definition of Large Igneous Provinces (LIPs): *Earth-Science Reviews*, v. 86, p. 175–202, doi:10.1016/j.earscirev.2007.08.008.
- Brzozowski, M.J., Hollings, P., Zhu, J.J., and Creaser, R.A., 2023, Osmium isotopes record a complex magmatic history during the early stages of formation of the North American Midcontinent Rift — Implications for rift initiation: *Lithos*, v. 436–437, doi:10.1016/j.lithos.2022.106966.
- Camp, V.E., and Hanan, B.B., 2008, A plume-triggered delamination origin for the Columbia River Basalt Group: *Geosphere*, v. 4, p. 480–495, doi:10.1130/GES00175.1.
- Campbell, I.H., 2007, Testing the plume theory: *Chemical Geology*, v. 241, p. 153–176, doi:10.1016/j.chemgeo.2007.01.024.
- Campbell, I.H., and Griffiths, R.W., 1990, Implications of mantle plume structure for the evolution of flood basalts: *Earth and Planetary Science Letters*, v. 99, p. 79–93.
- Campbell, I.H., and Naldrett, A.J., 1979, The influence of silicate: sulfide ratios on the geochemistry of magmatic sulfides: *Economic Geology*, v. 74, p. 1503–1505.
- Coffin, M.F., and Eldholm, O., 1994, Large igneous provinces: Crustal structure, dimensions, and external consequences: *Reviews of Geophysics*, v. 32, p. 1–36, doi:10.1029/93RG02508.

- Condie, K.C., 1982, Plate-tectonics model for Proterozoic continental accretion in the southwestern United States: <http://pubs.geoscienceworld.org/gsa/geology/article-pdf/10/1/37/3505731/i0091-7613-10-1-37.pdf>.
- Condie, K.C., and Shearer, C.K., 2019, Significance of high field strength and rare earth element distributions in deciphering the evolution of the inner solar system: *Geochimica et Cosmochimica Acta*, v. 266, p. 633–651, doi:10.1016/j.gca.2019.05.027.
- Condie, K.C., and Shearer, C.K., 2017, Tracking the evolution of mantle sources with incompatible element ratios in stagnant-lid and plate-tectonic planets: *Geochimica et Cosmochimica Acta*, v. 213, p. 47–62, doi:<https://doi.org/10.1016/j.gca.2017.06.034>.
- Cundari, R., Hollings, P., Smyk, M., and Carl, C., 2021, The geochemical evolution of the Logan Igneous Suite, Ontario, Canada: new insights from the Logan Basin and implications for the genesis of the Mesoproterozoic Midcontinent Rift System: Geological Society, London, Special Publications, doi:10.6084/m9.gshare.c.5490935.
- Duebendorfer, E.M., Chamberlain, K.R., and Jones, C.S., 2001, Paleoproterozoic tectonic history of the Cerbat Mountains northwestern Arizona: Implications for crustal assembly in the southwestern United States: *Bulletin of the Geological Society of America*, v. 113, p. 575–590, doi:10.1130/0016-7606(2001)113<0575:PTHOTC>2.0.CO;2.
- Ernst, R.E., 2021, Large Igneous Provinces, *in* Alderton, D. and Elias, S.A. eds., *Encyclopedia of Geology (Second Edition)*, Oxford, Academic Press, p. 60–68, doi:<https://doi.org/10.1016/B978-0-12-409548-9.12528-X>.
- Ernst, R.E., and Baragar, W.R.A., 1992, Evidence from magnetic fabric for the flow pattern of magma in the Mackenzie giant radiating dyke swarm: *Nature*, v. 356, p. 511–513, doi:10.1038/356511a0.
- Ernst, R.E., and Jowitt, S.M., 2013, Chapter 2 Large Igneous Provinces (LIPs) and Metallogeny: *Society of Economic Geologists*, v. 17, p. 17–51.
- Ernst, R.E., Liikane, D.A., Jowitt, S.M., Buchan, K.L., and Blanchard, J.A., 2019, A new plumbing system framework for mantle plume-related continental Large Igneous Provinces and their mafic-ultramafic intrusions: *Journal of Volcanology and Geothermal Research*, v. 384, p. 75–84, doi:10.1016/j.jvolgeores.2019.07.007.
- Ernst, R.E., and Youbi, N., 2017, How Large Igneous Provinces affect global climate, sometimes cause mass extinctions, and represent natural markers in the geological record: *Palaeogeography, Palaeoclimatology, Palaeoecology*, v. 478, p. 30–52, doi:<https://doi.org/10.1016/j.palaeo.2017.03.014>.
- Fairchild, L.M., Swanson-Hysell, N.L., Ramezani, J., Sprain, C.J., and Bowring, S.A., 2017, The end of Midcontinent Rift magmatism and the paleogeography of Laurentia: *Lithosphere*, v. 9, p. 117–133, doi:10.1130/L580.1.
- Ferguson, C.B., Duebendorfer, E.M., and Chamberlain, K.R., 2004, Synkinematic intrusion of the 1.4-Ga Boria Canyon Pluton, northwestern Arizona: Implications for Ca. 1.4-

- Ga regional strain in the Western United States: *Journal of Geology*, v. 112, p. 165–183, doi:10.1086/381656.
- La Flèche, M.R., Camiré, G., and Jenner, G.A., 1998, Geochemistry of post-Acadian, Carboniferous continental intraplate basalts from the Maritimes Basin, Magdalen Islands, Québec, Canada: *Chemical Geology*, v. 148, p. 115–136, doi:[https://doi.org/10.1016/S0009-2541\(98\)00002-3](https://doi.org/10.1016/S0009-2541(98)00002-3).
- Floyd, P.A., and Winchester, J.A., 1975, Magma type and tectonic setting discrimination using immobile elements: *Earth and Planetary Science Letters*, v. 27, p. 211–218.
- Ganino, C., and Arndt, N.T., 2009, Climate changes caused by degassing of sediments during the emplacement of large igneous provinces: *Geology*, v. 37, p. 323–326, doi:10.1130/G25325A.1.
- Grambling, T.A., Holland, M., Karlstrom, K.E., Gehrels, G.E., and Pecha, M., 2022, Revised location for the Yavapai-Mazatzal crustal province boundary in New Mexico: Hf isotopic data from Proterozoic rocks of the Nacimiento Mountains, *in* *New Mexico Geological Society*, p. 175–184, doi:10.56577/ffc-66.175.
- Hammond, J.G., 1986, Geochemistry and petrogenesis of Proterozoic diabase in the southern Death Valley region of California: *Contributions to Mineralogy and Petrology*, v. 93, p. 312–321.
- Hammond, J.G., 1990, Middle Proterozoic diabase intrusions in the southwestern U.S.A. as indicators of limited extensional tectonism: Mid-Proterozoic Laurentia-Baltica: Geological Association of Canada, Dept. of Earth Sciences, p. 517–531.
- Hammond-Gordon, J., Calzia, J., and Tapani Ramo, O., 2022, A new look at the diabase of the Southwest Laurentia Large Igneous Province (SWLLIP): Speeding Laurentia and stagnant slabs: Joint 118 Annual Cordilleran/ 72nd Annual Rocky Mountain Section Meeting, <https://gsa.confex.com/gsa/2022CD/webprogram/Paper373610.html>.
- Hansen, V.L., 2007, LIPs on Venus: *Chemical Geology*, v. 241, p. 354–374, doi:10.1016/j.chemgeo.2007.01.020.
- Harlan, S.S., 1993, Paleomagnetism of Middle Proterozoic diabase sheets from central Arizona: *Canadian Journal of Earth Sciences*, v. 30, p. 1415–1426, doi:10.1139/e93-122.
- He, C., 2020, Upwelling mantle plume and lithospheric delamination beneath the North China Craton: *Physics of the Earth and Planetary Interiors*, v. 306, doi:10.1016/j.pepi.2020.106548.
- Heaman, L.M., Easton, R.M., Hart, T.R., Hollings, P., MacDonald, C.A., and Smyk, M.C., 2007, Further refinement to the timing of Mesoproterozoic magmatism, Lake Nipigon region, Ontario: *Canadian Journal of Earth Sciences*, v. 44, p. 1055–1086, doi:10.1139/E06-117.
- Holland, M.E., Grambling, T.A., Karlstrom, K.E., Jones, J. V., Nagotko, K.N., and Daniel, C.G., 2020, Geochronologic and Hf-isotope framework of Proterozoic rocks from central

- New Mexico, USA: Formation of the Mazatzal crustal province in an extended continental margin arc: *Precambrian Research*, v. 347, doi:10.1016/j.precamres.2020.105820.
- Hollings, P., Hart, T.R., Richardson, A., and MacDonald, C.A., 2007a, Geochemistry of the Mesoproterozoic intrusive rocks of the Nipigon Embayment, northwestern Ontario: Evaluating the earliest phases of rift development: *Canadian Journal of Earth Sciences*, v. 44, p. 1087–1110, doi:10.1139/E06-127.
- Hollings, P., Richardson, A., Creaser, R.A., and Franklin, J.M., 2007b, Radiogenic isotope characteristics of the Mesoproterozoic intrusive rocks of the Nipigon Embayment, northwestern Ontario: *Canadian Journal of Earth Sciences*, v. 44, p. 1111–1129, doi:10.1139/E06-128.
- Hollings, P., Smyk, M., Heaman, L.M., and Halls, H., 2010, The geochemistry, geochronology and paleomagnetism of dikes and sills associated with the Mesoproterozoic Midcontinent Rift near Thunder Bay, Ontario, Canada: *Precambrian Research*, v. 183, p. 553–571, doi:10.1016/j.precamres.2010.01.012.
- Holwell, D.A., and McDonald, I., 2010, A review of the behaviour of platinum group elements within natural magmatic sulfide ore systems: *Platinum Metals Review*, v. 54, p. 26–36, doi:10.1595/147106709X480913.
- Howard, K.A., 1991, Intrusion of horizontal dikes: tectonic significance of Middle Proterozoic diabase sheets widespread in the upper crust of the southwestern United States: *Journal of Geophysical Research*, v. 96, p. 12461–12478, doi:10.1029/91jb00112.
- Howard, K.A., Nielson, I.E., Wilshire, H.G., Nakata, J.K., Goodge, J.W., Reneau, S.L., John, B.E., and Hansen, V.L., 1990, Preliminary geologic map of the Mohave Mountains area Mohave County, Western Arizona: doi:https://doi.org/10.3133/ofr90684.
- Hughes, A.E., Haque, N., Northey, S.A., and Giddey, S., 2021, Platinum group metals: A review of resources, production and usage with a focus on catalysts: *Resources*, v. 10, doi:10.3390/resources10090093.
- Humphris, S.E., Alt, J.C., Teagle, D.A., and Honnorez, J.J., 1998, Geochemical changes during hydrothermal alteration of basement in the stockwork beneath the active tag hydrothermal mound: *Proceedings of the Ocean Drilling Program, Scientific Results*, v. 158.
- Ivanov, A. V, He, H., Yan, L., Ryabov, V. V, Shevko, A.Y., Palesskii, S. V, and Nikolaeva, I. V, 2013, Siberian Traps large igneous province: Evidence for two flood basalt pulses around the Permo-Triassic boundary and in the Middle Triassic, and contemporaneous granitic magmatism: *Earth-Science Reviews*, v. 122, p. 58–76, doi:https://doi.org/10.1016/j.earscirev.2013.04.001.
- Jiang, S.Y., Wang, R.C., Xu, X.S., and Zhao, K.D., 2005, Mobility of high field strength elements (HFSE) in magmatic-, metamorphic-, and submarine-hydrothermal systems:

- Physics and Chemistry of the Earth, Parts A/B/C, v. 30, p. 1020–1029, doi:<https://doi.org/10.1016/j.pce.2004.11.004>.
- Jicha, B.R., Hart, G.L., Johnson, C.M., Hildreth, W., Beard, B.L., Shirey, S.B., and Valley, J.W., 2009, Isotopic and trace element constraints on the petrogenesis of lavas from the Mount Adams volcanic field, Washington: Contributions to Mineralogy and Petrology, v. 157, p. 189–207, doi:[10.1007/s00410-008-0329-6](https://doi.org/10.1007/s00410-008-0329-6).
- Jochum, K.P., McDonough, W.F., Palme, H., and Spettel, B., 1989, Compositional constraints on the continental lithospheric mantle from trace elements in spinel peridotite xenoliths: Nature, v. 340, p. 548–550, doi:[10.1038/340548a0](https://doi.org/10.1038/340548a0).
- John, B.E., 1982, Geologic Map of the Chemehuevi Mountains area, San Bernardino County, California and Mohave County, Arizona.:
- Jowitt, S.M., and Ernst, R.E., 2013, Geochemical assessment of the metallogenic potential of Proterozoic LIPs of Canada: Lithos, v. 174, p. 291–307, doi:[10.1016/j.lithos.2012.03.026](https://doi.org/10.1016/j.lithos.2012.03.026).
- Jowitt, S.M., Williamson, M.-C., and Ernst, R.E., 2014, Geochemistry of the 130 to 80 Ma Canadian High Arctic Large Igneous Province (HALIP) Event and Implications for Ni-Cu-PGE Prospectivity: Economic Geology, v. 109, p. 281–307, doi:[10.2113/econgeo.109.2.281](https://doi.org/10.2113/econgeo.109.2.281).
- Keays, R. ~R., 1995, The role of komatiitic and picritic magmatism and S-saturation in the formation of ore deposits: Lithos, v. 34, p. 1–18, doi:[10.1016/0024-4937\(95\)90003-9](https://doi.org/10.1016/0024-4937(95)90003-9).
- Keays, R.R., and Lightfoot, P.C., 2010, Crustal sulfur is required to form magmatic Ni-Cu sulfide deposits: Evidence from chalcophile element signatures of Siberian and Deccan Trap basalts: Mineralium Deposita, v. 45, p. 241–257, doi:[10.1007/s00126-009-0271-1](https://doi.org/10.1007/s00126-009-0271-1).
- Keays, R.R., and Lightfoot, P.C., 2007, Siderophile and chalcophile metal variations in Tertiary picrites and basalts from West Greenland with implications for the sulphide saturation history of continental flood basalt magmas: Mineralium Deposita, v. 42, p. 319–336, doi:[10.1007/s00126-006-0112-4](https://doi.org/10.1007/s00126-006-0112-4).
- Klausen, M.B., 2022, Highly magmatic break-up LIP centres: revisiting the East Greenland volcanic rifted margin, *in* Geological Society Special Publication, Geological Society of London, v. 518, p. 17–42, doi:[10.1144/SP518-2021-22](https://doi.org/10.1144/SP518-2021-22).
- Li, C., Arndt, N.T., Tang, Q., and Ripley, E.M., 2015, Trace element indiscrimination diagrams: Lithos, v. 232, p. 76–83, doi:[10.1016/j.lithos.2015.06.022](https://doi.org/10.1016/j.lithos.2015.06.022).
- Lightfoot, P.C., Hawkesworth, C.J., Hergt, J., Naldrett, A.J., Gorbachev, N.S., Fedorenko, V.A., and Doherty, W., 1993, Remobilisation of the major-, trace-element, and from picritic and tholeiitic Siberian Trap, Russia continental lithosphere by a mantle plume: Sr-, Nd-, and Pb-isotope evidence lavas of the Noril'sk District: Contributions to Mineralogy and Petrology, v. 114, p. 171–88.

- Linnen, R.L., and Keppler, H., 1997, Columbite solubility in granitic melts: consequences for the enrichment and fractionation of Nb and Ta in the Earth's crust: *Contributions to Mineralogy and Petrology*, v. 128, p. 213–227, doi:10.1007/s004100050304.
- Linnen, R.L., and Keppler, H., 2002, Melt composition control of Zr/Hf fractionation in magmatic processes: *Geochimica et Cosmochimica Acta*, v. 66, p. 3293–3301.
- Maier, W.D., Howard, H.M., Smithies, R.H., Yang, S.H., Barnes, S.-J., O'Brien, H., Huhma, H., and Gardoll, S., 2015, Magmatic ore deposits in mafic-ultramafic intrusions of the Giles Event, Western Australia: *Ore Geology Reviews*, v. 71, p. 405–436, doi:https://doi.org/10.1016/j.oregeorev.2015.06.010.
- Maier, W.D., Li, C., and De Waal, S.A., 2001, Why are there no major Ni–Cu sulfide deposits in large layered mafic-ultramafic intrusions? *The Canadian Mineralogist*, v. 39, p. 547–556, doi:10.2113/gscanmin.39.2.547.
- Marimon, R.S. et al., 2022, The generation and evolution of the Archean continental crust: The granitoid story in southeastern Brazil: *Geoscience Frontiers*, v. 13, p. 101402, doi:https://doi.org/10.1016/j.gsf.2022.101402.
- McDonough, W.F., and Sun, S.S., 1995, The composition of the Earth: *Chemical Geology*, v. 120, p. 223–253.
- McLennan, S.M., 2001, Relationships between the trace element composition of sedimentary rocks and upper continental crust: *Geochemistry, Geophysics, Geosystems*, v. 2, doi:https://doi.org/10.1029/2000GC000109.
- Mohr, M.T., Schmitz, M.D., Swanson-Hysell, N.L., Karlstrom, K.E., Macdonald, F.A., Holland, M.E., Zhang, Y., and Anderson, N.S., 2024, High-precision U–Pb geochronology links magmatism in the Southwestern Laurentia large igneous province and Midcontinent Rift: *Geology*, doi:10.1130/G51786.1.
- Mosher, S., 1998, Tectonic evolution of the southern Laurentian Grenville orogenic belt: *Bulletin of the Geological Society of America*, v. 110, p. 1357–1375, doi:10.1130/0016-7606(1998)110<1357:TEOTSL>2.3.CO;2.
- Mudd, G.M., Jowitt, S.M., and Werner, T.T., 2018, Global platinum group element resources, reserves and mining – A critical assessment: *Science of the Total Environment*, v. 622–623, p. 614–625, doi:10.1016/j.scitotenv.2017.11.350.
- Mungall, J.E., Hanley, J.J., Arndt, N.T., and Debecdelievre, A., 2006, Evidence from meimechites and other low-degree mantle melts for redox controls on mantle-crust fractionation of platinum-group elements: *www.pnas.org/cgi/doi/10.1073/pnas.0600878103*.
- Munteanu, M., Wilson, A.H., Yao, Y., Jiang, S.-Y., Chunnett, G., Luo, Y., Mafurutu, L., and Phadagi, R., 2010, A conduit-related genesis of the Lengshuiqing intrusive assemblage (Sichuan, SW China): *Journal of Volcanology and Geothermal Research*, v. 189, p. 118–130, doi:https://doi.org/10.1016/j.jvolgeores.2009.10.016.

- Naldrett, A.J., 2010a, From the mantle to the bank: The life of a Ni-Cu-(PGE) sulfide deposit: *South African Journal of Geology*, v. 113, p. 1–32, doi:10.2113/gssajg.113.1-1.
- Naldrett, A.J., 2004, *Magmatic Sulfide Deposits*: Springer Berlin Heidelberg, doi:10.1007/978-3-662-08444-1.
- Naldrett, A.J., 2010b, Secular Variation of Magmatic Sulfide Deposits and Their Source Magmas: *Economic Geology*, v. 105, p. 669–688, doi:https://doi.org/10.2113/gsecongeo.105.3.669.
- Naldrett, A.J., 1999, World-class Ni-Cu-PGE deposits: key factors in their genesis: *Mineralium Deposita*, v. 34, p. 227–240, doi:https://doi.org/10.1007/s001260050200.
- Northey, S., Mohr, S., Mudd, G.M., Weng, Z., and Giurco, D., 2014, Modelling future copper ore grade decline based on a detailed assessment of copper resources and mining: *Resources, Conservation and Recycling*, v. 83, p. 190–201, doi:10.1016/j.resconrec.2013.10.005.
- Nyman, M.W., and Karlstrom, K.E., 1997, Pluton emplacement processes and tectonic setting of the 1.42 Ga Signal batholith, SW USA: important role of crustal anisotropy during regional shortening: *Precambrian Research*, v. 82, p. 237–263.
- Peach, C.L., Mathez, E.A., and Keays, R.R., 1990, Sulfide melt-silicate melt distribution coefficients for noble metals and other chalcophile elements as deduced from MORB: Implications for partial melting: *Geochimica et Cosmochimica Acta*, v. 54, p. 3379–3389, doi:https://doi.org/10.1016/0016-7037(90)90292-S.
- Pearce, J.A., 1996, A user's guide to basalt discrimination diagrams: *Geological Association of Canada Short Courses*, v. 12, p. 79–113.
- Pearce, J.J., Harris, N.B.W., and Tindle, A.G., 1984, Trace Element Discrimination Diagrams for the Tectonic Interpretation of Granitic Rocks: *Journal of Petrology*, v. 25, p. 956–983, doi:10.1093/petrology/25.4.956.
- Pinti, D.L., 2011, Rare Earth Elements, in Gargaud, M., Amils, R., Quintanilla, J.C., Cleaves, H.J. (Jim), Irvine, W.M., Pinti, D.L., and Viso, M. eds., *Encyclopedia of Astrobiology*, Berlin, Heidelberg, Springer Berlin Heidelberg, p. 1432–1436, doi:10.1007/978-3-642-11274-4_1348.
- Ripley, E.M., and Li, C., 2003, Sulfur isotope exchange and metal enrichment in the formation of magmatic Cu-Ni-(PGE) deposits: *Economic Geology*, v. 98, p. 635–641, doi:10.2113/gsecongeo.98.3.635.
- Roberts, M.T., 1976, California Division of Mines and Geology Special Report 106 *Geologic Features-Death Valley, California Stratigraphy and Depositional Environments of the Crystal Spring Formation, Southern Death Valley Region, California.*
- Robertson, J.C., Barnes, S.J., and Le Vaillant, M., 2015, Dynamics of magmatic sulphide droplets during transport in silicate melts and implications for magmatic sulphide ore formation: *Journal of Petrology*, v. 56, p. 2445–2472, doi:10.1093/petrology/egv078.

- Rollinson, H.R., 1993, *Using Geochemical Data*: Routledge, 384 p., doi:10.4324/9781315845548.
- Rollinson, H., and Pease, V., 2021, *Using Geochemical Data to Identify Tectonic Environments*, in *Using Geochemical Data*, Cambridge University Press, p. 157–177, doi:10.1017/9781108777834.008.
- Rudnick, R.L., and Gao, S., 2013, *Composition of the Continental Crust*, in *Treatise on Geochemistry: Second Edition*, Elsevier Inc., v. 4, p. 1–51, doi:10.1016/B978-0-08-095975-7.00301-6.
- Salters, V.J.M., 2011, *Elements: High field strength*: White, W (eds) *Encyclopedia of Geochemistry*. *Encyclopedia of Earth Sciences Series*, v. 25, p. 956–983.
- Van Schmus, W.R., 1992, *Tectonic setting of the Midcontinent Rift system: Tectonophysics*, v. 213, p. 1–15, doi:https://doi.org/10.1016/0040-1951(92)90247-4.
- Van Schmus, W.R., Martin, M.W., Sprowl, D.R., Geissman, J., and Berendsen, P., 1990, *Age, Nd, and Pb isotopic composition, and magnetic polarity for subsurface samples of the 1100 Ma Midcontinent rift: Geological Society of America Abstracts with Programs*, v. 22, p. A174.
- Severson, M., Miller, J., Peterson, D., Green, J., and Hauck, S., 2002, *Mineral potential of the Duluth Complex and related intrusions: Minnesota Geological Survey Report of Investigations*, v. 58.
- Shervais, J.W., 1982, *Ti-V plots and the petrogenesis of modern and ophiolitic lavas: Earth and Planetary Science Letters*, v. 59, p. 101–118.
- Shervais, J.W., and Vetter, S.K., 2009, *High-K alkali basalts of the Western Snake River Plain (Idaho): Abrupt transition from tholeiitic to mildly alkaline plume-derived basalts: Journal of Volcanology and Geothermal Research*, v. 188, p. 141–152, doi:https://doi.org/10.1016/j.jvolgeores.2009.01.023.
- Sheth, H.C., 2007, *‘Large Igneous Provinces (LIPs)’: Definition, recommended terminology, and a hierarchical classification: Earth-Science Reviews*, v. 85, p. 117–124, doi:https://doi.org/10.1016/j.earscirev.2007.07.005.
- Sleep, N.H., 1997, *Lateral flow and ponding of starting plume material: Journal of Geophysical Research: Solid Earth*, v. 102, p. 10001–10012, doi:10.1029/97jb00551.
- Smythe, D.J., Fonseca, R.O.C., and Kiseeva, E.S., 2017, *Chalcophile elements and sulfides in the upper mantle: Elements*, v. 13, p. 111–116, doi:10.2113/gselements.13.2.111.
- Srivastava, R.K., Ernst, R.E., Buchan, K.L., and de Kock, M., 2022, *An overview of the plumbing systems of large igneous provinces and their significance: Geological Society, London, Special Publications*, v. 518, p. 1–16, doi:10.1144/SP518-2021-167.

- Stensrud, H.L., and More, S., 1980, Precambrian Geology and Massive Sulfide Environments of the West-Central Hualapai Mountains, Mohave County, Arizona-A Preliminary Report.:
- Strickland, B.A., Wooden, J.L., Mattinson, C.G., Ushikubo, T., Miller, D.M., and Valley, J.W., 2013, Proterozoic evolution of the Mojave crustal province as preserved in the Ivanpah Mountains, southeastern California: *Precambrian Research*, v. 224, p. 222–241, doi:10.1016/j.precamres.2012.09.006.
- Sun, S.S., and McDonough, W.F., 1989, Chemical and isotopic systematics of oceanic basalts: Implications for mantle composition and processes: *Geological Society Special Publication*, v. 42, p. 313–345, doi:10.1144/GSL.SP.1989.042.01.19.
- Swanson-Hysell, N.L., Hoaglund, S.A., Crowley, J.L., Schmitz, M.D., Zhang, Y., and Miller Jr., J.D., 2020, Rapid emplacement of massive Duluth Complex intrusions within the North American Midcontinent Rift: *Geology*, v. 49, p. 185–189, doi:10.1130/G47873.1.
- Swanson-Hysell, N.L., Ramezani, J., Fairchild, L.M., and Rose, I.R., 2019, Failed rifting and fast drifting: Midcontinent Rift development, Laurentia's rapid motion and the driver of Grenvillian orogenesis: *Bulletin of the Geological Society of America*, v. 131, p. 913–940, doi:10.1130/B31944.1.
- Taylor, S.R., and McLennan, S.M., 1985, *The continental crust: Its composition and evolution: United States*, Blackwell Scientific Pub., Palo Alto, CA, <https://www.osti.gov/biblio/6582885>.
- Theodore, T.G., Blair, W.N., and Nash, J.T., 1987, Geology and gold mineralization of the Gold Basin-Lost Basin mining districts, Mohave County, Arizona: Department of the Interior, US Geological Survey, p. 9–13.
- Timmons, J.M., Karlstrom, K.E., Heizler, M.T., Bowring, S.A., Gehrels, G.E., and Crossey, L.J., 2005, Tectonic inferences from the ca. 1255-1100 Ma Unkar Group and Nankoweap Formation, Grand Canyon: Intracratonic deformation and basin formation during protracted Grenville orogenesis: *Bulletin of the Geological Society of America*, v. 117, p. 1573–1595, doi:10.1130/B25538.1.
- Turner, S.J., and Langmuir, C.H., 2015, What processes control the chemical compositions of arc front stratovolcanoes? *Geochemistry, Geophysics, Geosystems*, v. 16, p. 1865–1893, doi:<https://doi.org/10.1002/2014GC005633>.
- Wallace, M.L., Jowitt, S.M., and Saleem, A., 2015, Geochemistry and petrogenesis of mafic-ultramafic suites of the Irindina Province, Northern Territory, Australia: Implications for the Neoproterozoic to Devonian evolution of central Australia: *Lithos*, v. 234–235, p. 61–78, doi:10.1016/j.lithos.2015.07.009.
- Wang, K., Plank, T., Walker, J.D., and Smith, E.I., 2002, A mantle melting profile across the Basin and Range, SW USA: *Journal of Geophysical Research: Solid Earth*, v. 107, p. 51–521, doi:10.1029/2001JB000209.

- Wang, C.Y., Zhou, M.F., and Keays, R.R., 2006, Geochemical constraints on the origin of the Permian Baimazhai mafic-ultramafic intrusion, SW China: *Contributions to Mineralogy and Petrology*, v. 152, p. 309–321, doi:10.1007/s00410-006-0103-6.
- Whitmeyer, S.J., and Karlstrom, K.E., 2007, Tectonic model for the Proterozoic growth of North America: *Geosphere*, v. 3, p. 220–259, doi:10.1130/GES00055.1.
- Winchester, J.A., and Floyd, P.A., 1977, Geochemical discrimination of different magma series and their differentiation products using immobile elements: *Chemical Geology*, v. 20, p. 325–343.
- Wright, L.A., Troxel, B.W., Williams, E.G., Roberts, M.T., and Diehl, P.E., 1976, *Precambrian Sedimentary Environments of the Death Valley Region, Eastern California*: California Division of Mines and Geology, Special Report 106, p.7-15.:
- Wrucke, C.T., 1967, *Precambrian and Permian rocks in the vicinity of Warm Spring Canyon, Panamint Range, California*: Stanford University, 1–211 p.
- Wrucke, C.T., 1993, *The Apache Group, Troy Quartzite, and Diabase: Middle Proterozoic rocks of Central and Southern Arizona: Precambrian: conterminous*, v. C–2, p. 517–521.
- Wrucke, C.T., 1989, *The middle Proterozoic Apache Group, Troy Quartzite, and associated diabase of Arizona*: Arizona Geological Society, v. 17, p. 239–258.
- Wrucke, C.T., Stone, P., and Stevens, C.H., 2007, *Geologic map of the Warm Spring Canyon Area, Death Valley National Park, Inyo County, California with a discussion of the regional significance of the stratigraphy and structure*: USGS, v. 1.1.
- Yakubchuk, A., and Nikishin, A., 2004, Noril'sk-Talnakh Cu-Ni-PGE deposits: a revised tectonic model: *Mineralium Deposita*, v. 39, p. 125–142, doi:10.1007/s0012600303730.
- Yao, Z., and Mungall, J.E., 2021, Linking the Siberian Flood Basalts and Giant Ni-Cu-PGE Sulfide Deposits at Norilsk: *Journal of Geophysical Research: Solid Earth*, v. 126, p. e2020JB020823, doi:https://doi.org/10.1029/2020JB020823.
- Yao, Z., and Mungall, J.E., 2022, Transport and deposition of immiscible sulfide liquid during lateral magma flow: *Earth-Science Reviews*, v. 227, p. 1–23, doi:10.1016/j.earscirev.2022.103964.
- Yao, Z., Qin, K., and Mungall, J.E., 2018, Tectonic controls on Ni and Cu contents of primary mantle-derived magmas for the formation of magmatic sulfide deposits: *American Mineralogist*, v. 103, p. 1545–1567, doi:10.2138/am-2018-6392.
- Yuan, F., Zhou, T., Zhang, D., Jowitt, S.M., Keays, R.R., Liu, S., and Fan, Y., 2012, Siderophile and chalcophile metal variations in basalts: Implications for the sulfide saturation history and Ni–Cu–PGE mineralization potential of the Tarim continental flood basalt province, Xinjiang Province, China: *Ore Geology Reviews*, v. 45, p. 5–15, doi:https://doi.org/10.1016/j.oregeorev.2011.04.003.

Zhong, F.J., Wang, L., Wang, K.X., Liu, J.G., Zhang, Y., Li, H., Yang, S., Chen, Y.P., Xia, F., and Pan, J.Y., 2023, Mineralogy and geochemistry of hydrothermal alteration of the Mianhuakeng uranium deposit in South China: Implications for mineralization and exploration: *Ore Geology Reviews*, v. 160, doi:10.1016/j.oregeorev.2023.105606.

CURRICULUM VITAE

Thomas J. Boes

Email: thomasboes86@gmail.com

EDUCATION

Master of Science, Economic Geology August 2021 – May 2024

University of Nevada, Las Vegas, NV | GPA: 3.64

Thesis: Assessing the potential for magmatic sulfides within Southwestern
Laurentia large igneous province

- **Relevant Coursework:** Research Methods, Instrumental Techniques, Geographic Information Systems (GIS): Theory and Applications, Geology of Metallic Ore Deposits, Poster Presentation and Time Management, Advanced Geochronology and Thermochronology, Seminar in Economic Geology, Geology of the Evolution of West North America, Geochronology
- **Grants & Awards:** Scholarship Recipient of Rocky Mountain Federation of Mineralogical Societies (\$4,000), UNLV Travel Grant (\$900), Society of Economic Geologist Student Grant (\$5,000).
- **Talks and Poster Presentations:** AGU Fall 2022 (poster), UNLV Geosymposium 2022 & 2023 (poster and talk, respectively), SEG 2023 London Conference (Poster), CREG Reno, NV 2024 (talk), LIP Industry Consortium Workshop 2024 (Virtual talk).

Bachelor of Arts, Geology

August 2018 – May 2021

University of Nevada, Las Vegas, NV

Geology Major | GPA: 3.62

- **Honors:** Deans Honor List (4x)
- **Additional studies:** Mentee with UNLV RAMP program 2020-2021

EXPERIENCE

Graduate Teaching Assistant, University of Nevada, Las Vegas, NV August 2021 – May 2024

- Instructed lab portions of GEOL 101L, GEOL102L, GEOL 333L, and GEOL 372
- Assisted professors in teaching Las Vegas geology to CCSD science teachers to implement in their geology lessons through RAMP.

Research Assistant, University of Nevada, Las Vegas, NV August 2020 – May 2021

- Field assistant that collected rock samples and entered data from zircon separation to constrain pegmatite emplacement.
- Method Used: Badger, Disk-mill, Wilfley Table, Methylene Iodide separation, Frantz magnetic separation, and hand-picking.
- Compiled trace element data for zircons using GeoChemical Toolkit (GCDkit).

Shipping and Receiving Auditor, Hilton, La Jolla, CA September 2016 – December 2017

- Meticulous shipping clerk that processes all outgoing and incoming shipments from all delivery services.
- Created and managed control logs for the tracking and placement of freight.
- Input bank statements and Expedia reservations and assisted the hotel in any required area.
- Expanded responsibility through accounting and P&L management, improving hotel record-keeping and operational budget-keeping practices.

Interior Communication Electrician, United States Navy San Diego, CA

September 2012 – September 2016

- Work Center Supervisor responsible for three technicians and all internal communication on board USS Dewey during our 9 ½ month deployment and within homeport.
- Responsible for over 100 jack-boxes, 200 phones, 300 1mc speakers, SGSI, WSN-8, 1,000 smoke alarms, 100 flooding alarms, parasense, VCHT alarms, and SITE TV.
- Maintained and scheduled over 5,000 maintenance checks a quarter.

ORGANIZATIONS & LEADERSHIP

Society of Economic Geology (SEG) UNLV Student Chapter

- Vice President Spring 2022- Fall 2022
- Member 2018 - Present

American Association of Petroleum Geology (AAPG) UNLV Student Chapter

- Vice President Fall 2020 – Fall 2021
- Member Fall 2018- Present

Geopath

- Volunteer Summer 2023- Present

SKILLS

Software: Proficient with ArcGIS, Google Earth Pro, Adobe Illustrator, Adobe Photoshop, Microsoft Office (Word, Excel, PowerPoint), Windows OS, and Mac OS.

• **Field/Lab:** Experience using microscopes (reflected and transmitted light), diamond saws, Badger, Disk-mill, Wilfley Table, Methylene Iodide separation, Frantz magnetic separation, and hand-picking interpreting topographic maps.